ABSTRACT

Title of dissertation: NUCLEAR MODIFICATION FACTOR
OF HIGH MOMENTUM JETS
IN $\sqrt{s_{_{NN}}} = 2.76$ TeV
PbPb COLLISIONS

Ying Lu,
Doctor of Philosophy, 2013

Dissertation directed by: Professor Alice C. Mignerey
Department of Chemistry and Biochemistry

According to quantum chromodynamics (QCD), the release of quarks and gluons creates a new form of matter, the quark gluon plasma (QGP), expected to occur in relativistic heavy-ion collisions at high energies. The structure and dynamics of the QGP can be studied using partonic interactions at large momentum transfers. This was studied at the Relativistic Heavy Ion Collider starting in 2002 utilizing AuAu collisions at 200 GeV center-of-mass. In this analysis, fully reconstructed jets in pp and PbPb collisions at 2.76 TeV center-of-mass energy are analyzed with the CMS detector at the Large Hadron Collider (LHC) in CERN. The ratio of inclusive reconstructed jet transverse momenta spectra of PbPb collisions to that of proton+proton (pp) collisions is defined as the jet nuclear modification factor (R_{AA}) and is studied to quantify the medium modification within transverse momenta above 100 GeV/c. Jet R_{AA} results are compared for three different unfolding methods: Bayesian Unfolding, Bin-By-Bin Unfolding and Generalized Singular Value

Decomposition (GSVD) Unfolding, as well as corrections performed with pp data smearing. A jet R_{AA} of approximately 0.5 is observed in the most central collisions and close to unity in the most peripheral collisions without a strong indication of any transverse momenta (p_T) dependence. A suppression of high p_T jets is observed in central PbPb collisions in comparison to peripheral collisions. This is consistent with the observation of jet quenching.

NUCLEAR MODIFICATION FACTOR OF HIGH TRANSVERSE MOMENTUM JETS IN $\sqrt{s_{_{NN}}} = 2.76$ TeV PbPb COLLISIONS

by

Ying Lu

Dissertation submitted to the Faculty of the Graduate School of the
University of Maryland, College Park in partial fulfillment
of the requirements for the degree of
Doctor of Philosophy
2013

Advisory Committee:
Professor Alice C. Mignerey, Chair/Advisor
Professor Nicholas J. Hadley
Professor Christopher Jarzynski
Professor Garegin Papoian
Professor John Ondov

Acknowledgments

This dissertation is a conclusion of my wonderful journey towards the Ph.D. It is with the deepest gratitude that I acknowledge the persistent support and guidance of my advisor, Professor Alice Mignerey. Her enthusiasm in research and patience in teaching touched my soul and encouraged me to march forward all these past years.

I would like to express appreciation towards my committee members, Professor Nicholas J. Hadley, Professor Christopher Jarzynski, Professor Garegin Papoian and Professor John Ondov, for the kind help they provided me.

Also, I am indebted to Dr. Marguerite Tonjes, who works as a research faculty in University of Maryland, Dr. David Mason, who works as a research faculty in Fermi National Laboratory, and Dr Yen-Jie Lee, who works as a postdoctoral fellow in CERN and soon will start his new career in the U.S. These three physicists were great mentors during the years of my Ph.D research. I have been working with Dr. Marguerite Tonjes since the beginning of my graduate studies. She is a mentor in research, a co-worker in analysis, and a friend in life. Her extraordinary patience, problem-solving and multi-task ability have set an outstanding example. Her involvement as a contact in our analysis group has also granted me the advantange to discuss with her various issues related to my research. The guidance she provided me with in programming techniques, software utilization and documentation editing will benefit me for a life time. Dr. David Mason is my sponsor for the University Research Association Fellowship. I cannot express my gratitude enough to him thinking about the hours and hours he spent with me on coding. His devotion truly inspired me. Dr. Yen-Jie Lee, who has been the most outstanding researcher I have seen in my age, provided me with so much concrete advice in the analysis conducted in this thesis. His deep enthusiasm, sharp perspectives and logical reasoning in physics made our analysis possible.

In particular, I would like to share my credits with my analysis collaborators: Dr. Pawan Kumar Netrakanti (Bhabha Atomic Research Center), Dr. Yue Shi Lai (Massachusetts Institute of Technology), Dr. Sevil Salur (Rutgers University) and Dr. Jorge Robles (Rutgers University). Each of them has devoted a great amount of their time and expertise in the analysis. After countless hours of video-conferences and meeting, with the difficulty of the time difference, we finally made it and have our result publicized.

I have made two trips to CERN and obtained an aweful lot of help from Frank Ma, Yongsun Kim and Yetkin Yilmaz, who are graduate students in Massachusetts Institute of Technology working in the same sub-group of the Heavy Ion community as me. They are all graduating now and I wish them the best luck in the future.

In addition, I would like to thank Yu Zheng, a graduate student of Purdue University working in Fermi National Laboratory, and Fan Yang, a postdoctoral researcher in Fermi National Laboratory. Both of them shared a myriad of their hands-on experience with me on coding.

I wish to thank my husband Charles Robey, who has been my best friend in the past three years and gave me the best Christmas gift last year, the birth of our beautiful daughter, Annabel Robey. Indeed, I am very grateful to my mother, Weihong Ran and my father, Dongfeng Lu who have gave me so much encouragement

through these years and helped me overcome the toughest time of my life. Finally, I would love to acknowledge my father-in-law, Frank Robey, who is a chemist himself and has given me practical advice on improving my written techniques.

Table of Contents

Acknowledgements ii

List of Tables vii

List of Figures viii

Glossary of Terms xii

Overview xiv

1 Introduction 1
  1.1 The Standard Model 1
    1.1.1 Fundamental Particles 1
    1.1.2 Quantum Chromodynamics 5
  1.2 Quark Gluon Plasma 9
  1.3 Heavy-ion Collisions 15
    1.3.1 Event Characterization 15
    1.3.2 Jets 17
  1.4 Nuclear Modification Factor R_{AA} 20

2 Experimental Overview 22
  2.1 Large Hadron Collider 22
  2.2 Compact Muon Solenoid Detector 23

3 Event Selection 29
  3.1 Online Selection 29
    3.1.1 Types of Collisions and Available L1 Triggers 30
    3.1.2 Selecting Minimum Bias Collisions 32
    3.1.3 Collisions With High Energy Jets 32
  3.2 Offline Event Selection 35
    3.2.1 Removal of HCAL Anaomalous Signals 36
    3.2.2 Leading Track Jet Quality Identification 36
    3.2.3 Luminosity and Dataset 37
    3.2.4 Centrality Determination 38

4 Jet Reconstruction 44
  4.1 Monte Carlo (MC) Simulation 44
  4.2 Jet Reconstruction Algorithms 46
  4.3 Underlying Event Subtraction 48
  4.4 Jet Finding Efficiency 50
  4.5 Jet Resolution and Response 54

5 Analysis 57
5.1 Measured Jet Spectra and Measured Jet R_{AA} 57
5.2 Unfolding the Jet Spectra 63
5.2.1 Bayesian Method and Bin-by-Bin Method 67
5.2.2 GSVD Method 68
5.3 Smearing Method 73

6 Systematic Errors 88
6.1 Jet Resolution Systematics 88
6.2 Background Fluctuation 90
6.3 Hadronic Calorimeter Noise 90
6.4 Jet Finding Efficiency Uncertainty 95
6.5 Jet Trigger Efficiency Uncertainty 95
6.6 Luminosity and Event Selection Uncertainty 95
6.7 Jet Energy Scale Uncertainty 96
6.8 Uncertainty in T_{AA} 97
6.9 Total Systematics 97

7 Results 99
7.1 Jet R_{AA} vs. p_T Result 99
7.2 Jet R_{AA} vs. N_{part} Result 109

8 Conclusion 111

A Lorentz Contraction 114

B Rapidity and Pseudorapidity 116

C Luminosity 120

D Unfolding Techniques 123

E Jet Quality Check 128

Bibliography 136

List of Tables

1.1 Quarks 2
1.2 Leptons 3
1.3 Gauge Bosons 4
1.4 Baryons and Mesons 5

2.1 Beam Parameters of Lead-lead Collisions. 23

3.1 Selection Impact on PbPb Sample. 39
3.2 Selection Impact on pp Sample. 39

4.1 PYTHIA Events Simulated and Embedded in HYDJET Samples 45
4.2 σ Values from Gaussian Fits to Random Cone Distributions of the Min-bias PbPb data. 53
4.3 σ Values from Gaussian Fits to Random Cone Distributions of MC Simulation. 53

5.1 Parameters of the Functional Form for the Jet Energy Resolution for pp and PbPb Centralities. 79
5.2 Smearing Factors (in GeV/c) for pp in Different PbPb Centralities with Bin-by-Bin and Fit-based Methods. 83

6.1 Jet Selection Efficiency from MC Studies. 93
6.2 Glauber Model Parameters(N_{coll}, N_{part}, T_{AA}) 97
6.3 Summary of the Systematic Uncertainties. 98

List of Figures

1 Charge hadron R_{AA} at STAR Collaboration. xv
2 JetR_{AA} as a function of p_T in Bayesian unfolding method. xvii

1.1 Particle classification hierarchy. 5
1.2 Feynman Diagram of quark color exchange via a gluon. 6
1.3 Illustration of quark confinement. 8
1.4 Quark confinement via the inelastic reaction $\mathrm{e}^{-} + \mathrm{p} \rightarrow \mathrm{e}^{-} + \mathrm{p}$. 9
1.5 Atomic and nuclear phase diagrams. 10
1.6 Hadronic and QGP phases of nuclear matter. 11
1.7 Heavy-ion collision evolution. 15
1.8 The relationship of η-θ. 17
1.9 Di-jet event in a heavy-ion collision. 18

2.1 LHC physical layout. 24
2.2 LHC injection system layout. 25
2.3 CMS detector and sub-detectors 26
2.4 CMS Acceptance 27
2.5 The transverse view of CMS detector 28
2.6 First heavy-ion event in LHC. 28

3.1 Trigger efficiency 34
3.2 Recorded integrated luminosity for the heavy-ion runs. 38
3.3 Heavy-ion collision geometry 41
3.4 Centrality determination for min-bias and HLT-triggered samples. . . 42

4.1 Underlying event background in PbPb collisions. 50
4.2 Underlying event background in PbPb collisions within $100 < p_T(\,\mathrm{GeV}/c) <$ 110. 51
4.3 Jet reconstruction efficiency 52
4.4 Random cone background study 54
4.5 Jet p_T response and p_T resolution for anti-k_{T} jet algorithm with various resolution parameters. 56
4.6 Jet p_T response and p_T resolution for anti-k_{T} jet algorithm with R=0.3. 56

5.1 Measured jet spectra of pp and PbPb samples with R = 0.2. 58
5.2 Measured jet spectra of pp and PbPb samples with R = 0.3. 59
5.3 Measured jet spectra of pp and PbPb samples with R = 0.4. 59
5.4 Measured R_{AA} constructed with anti-k_{T} particle flow jets in cone size 0.2. 60
5.5 Measured R_{AA} constructed with anti-k_{T} particle flow jets in cone size 0.3. 61
5.6 Measured R_{AA} constructed with anti-k_{T} particle flow jets in cone size 0.4. 62
5.7 Response matrix for PbPb from Bayesian unfolding method(a). . . . 65

5.8 Response matrix for PbPb from Bayesian unfolding method(b). . . . 66
5.9 Response matrix constructed for pp from Bayesian unfolding method. 67
5.10 PbPb MC closure test for Bayesian method. 69
5.11 pp MC closure test for Bayesian method. 69
5.12 PbPb MC closure test for GSVD $R = 0.2$. 70
5.13 PbPb MC closure test for GSVD $R = 0.3$. 71
5.14 PbPb MC closure test for GSVD $R = 0.4$. 71
5.15 Proton-proton MC closure test for GSVD $R = 0.3$. 72
5.16 Jet p_T spectra for pp collisions with and without smearing factors (bin-by-bin). 73
5.17 Jet p_T spectra for pp collisions with and without smearing factors (fit). 74
5.18 The ratio of reconstructed jet and generated jet p_T for PbPb and smeared pp. 75
5.19 The ratio of reconstructed jet and generated jet p_T for PbPb and smeared pp. 76
5.20 σ of the RecoJet p_T over GenJet p_T as a function of centrality for various p_T bins for the anti-k_{T} jet algorithm with R=0.3 76
5.21 Mean of the RecoJet p_T over GenJet p_T as a function of centrality for various p_T bins for the anti-k_{T} jet algorithm with R=0.3. 77
5.22 Ratio of PbPb jet spectra to bin-by-bin smeared pp jet spectra as a function of reconstructed jet p_T. 77
5.23 Jet energy resolution as function of generated jet p_T for pp and PbPb(parametrization). 79
5.24 Jet energy scale as function of generated jet p_T in PbPb(third-order polynomial). 80
5.25 Jet energy resolution as function of generated jet p_T for smeared pp reco jet p_T. 80
5.26 Jet energy scale as function of generated jet p_T for smeared pp reco jet p_T. 81
5.27 Comparison of the ratio of reconstructed jet p_T and the generated jet p_T distributions for pp, smeared pp and 0–5% PbPb collisions. . . . 84
5.28 Comparison of the ratio of reconstructed jet p_T and the generated jet p_T distributions for pp, smeared pp and 5–10% PbPb collisions. . . . 84
5.29 Comparison of the ratio of reconstructed jet p_T and the generated jet p_T distributions for pp, smeared pp and 10–30% PbPb collisions. . . 85
5.30 Comparison of the ratio of reconstructed jet p_T and the generated jet p_T distributions for pp, smeared pp and 30–50% PbPb collisions. . . 85
5.31 Comparison of the ratio of reconstructed jet p_T and the generated jet p_T distributions for pp, smeared pp and 50–70% PbPb collisions. . . 86
5.32 Comparison of the ratio of reconstructed jet p_T and the generated jet p_T distributions for pp, smeared pp and 70–90% PbPb collisions. . . 86
5.33 MC closure test with pp smearing method. 87

6.1 Bayesian unfolding method in various iterations. 89
6.2 HCAL noise study in PbPb collisions 91

6.3 HCAL noise study in pp collisions 92
6.4 HCAL noise study in PbPb collisions with leading track identification. 92
6.5 HCAL noise study in pp collisions with leading track identification. . 93
6.6 HCAL noise selection efficiency. 94
6.7 Ratio between unfolded jet p_T spectra varied by the 2% jet p_T scale and the unvaried jet p_T spectra. 96
6.8 Total Systematic Uncertainties. 98

7.1 Bayesian unfolded jet R_{AA} for anti-k_{T} jets of R=0.3. 100
7.2 Jet R_{AA} constructed for R=0.3 jets using various correcting methods. 101
7.3 Jet R_{AA} in various resolution parameters for anti-k_{T} jets using Bayesian unfolding method for the given centrality bins. 102
7.4 Jet R_{AA} constructed by anti-k_{T} particle flow jets in cone size 0.3 using GSVD unfolding. 103
7.5 R_{AA} in different cone sizes for anti-k_{T} particle flow jets in cone size 0.3 with GSVD unfolding method. 104
7.6 R_{AA} in different cone sizes for anti-k_{T} particle flow jets and anti-k_{T} calorimeter jets with Bayesian method. 105
7.7 R_{AA} in different cone sizes for akPuPF jets and akPuCalo jets with Bin-by-Bin unfolding method. 106
7.8 R_{AA} for calorimeter and particle flow jets in anti-k_{T} algorithm with Bayesian method in jet cone size 0.3. 107
7.9 R_{AA} for akPu3Calo jets in comparison of Bayesian and smearing method. 108
7.10 Ratio of R_{AA} Smearing and Bayesian methods in different centrality bins. 108
7.11 R_{AA} vs N_{part}. 109
7.12 R_{AA} vs N_{part} for various techniques. 110

8.1 R_{AA} “zoo”. 113

A.1 $\gamma(\beta)$. 115

B.1 Rapidity(v/c). 117
B.2 Rapidity and pseudorapidity as a function of θ. 119

E.1 Jet η distribution comparison of data and MC sample. 129
E.2 Jet ϕ distribution comparison of data and MC sample. 129
E.3 Jet p_T distribution comparison of data and MC sample. 130
E.4 Jet η-ϕ distribution of data sample. 130
E.5 Jet η-ϕ distribution of MC sample. 131
E.6 Jet η-p_T distribution of data sample. 131
E.7 Jet η-p_T distribution of MC sample. 132
E.8 Jet η-p_T distribution of MC sample. 132
E.9 JetID neutralMax with ak3PuPF jets. 133
E.10 JetID neutralMax data / MC ratio with ak3PuPF jets. 133

E.11 JetID photonMax ak3PuPF 134
E.12 JetID photonMax data / MC ratio with ak3PuPF jets. 134
E.13 JetID trackMax data / MC ratio with ak3PuPF jets. 135
E.14 JetID trackMax data / MC ratio with ak3PuPF jets. 135

Glossary of Terms

ALICE	A Large Ion Collider Experiment
ATLAS	A Toroidal LHC Apparatus
γ	(1) photon, (2) Lorentz factor
Δz	distance traveled
θ	polar angle with respect to beam axis
μ	muon
π	pion
ρ	nucleon density
σ_{NN}	inelastic nucleon-nucleon cross section
ϕ	azimuthal angle about the beam axis
χ^2	variable in a "goodness-of-fit" test quantifying how well an observed distribution fits a hypothesized or theoretical distribution
$\sqrt{s_{NN}}$	center-of-mass collision energy per nucleon pair
2D	two-dimensional
b	barn, unit of cross section ($10^{-24} cm^2$)
b	impact parameter
BSC	beam scintillation counter
BPTX	beam pick-up timing experiment devices, a trigger system in CMS
c	speed of light
centrality	% of collisions having more geometric overlap than current collision
CERN	European organization for nuclear physics
CMS	Compact Muon Solenoid
CPU	central processing unit
DAQ	data acquisition system
DQM	data quality monitoring
η	(1) pseudorapidity, (2) viscosity (rarely)
ECAL	electronic calorimeter
e	electron or positron depending on charge
E	energy
eV	electron volt
Gen	generated simulation data
HCAL	hadronic calorimeter
HLT	high-level trigger
HF	hadronic forward calorimeter
L	(1) integrated depth of absorber material, (2) nuclei's measured length in laboratory's reference frame
L_0	nuclei's length when at rest
$\mathscr{L}$	instantaneous luminosity
$\mathscr{L}_i$	integrated or delivered luminosity
$\mathscr{L}_r$	recorded or collected luminosity

Glossary of Terms (continued)

LHC	Large Hadron Collider
LHCb	Large Hadron Collider beauty
L1	level-1 hardware-based trigger
MC	Monte Carlo simulation
Min-Bias	minimum bias
N	north
N	number of particles
N_{evts}	number of events
N_{MB}	number of min-bias events
N_{part}	number of nucleons interacting in collision
ndf	number of degrees of freedom
p	proton
p	total momentum
p_T	transverse momentum
p_z	longitudinal momentum
Pb	lead
$PbWO_4$	lead tungstate
PMT	photomultiplier tube
q	quark
$\overline{q}$	antiquark
QCD	Quantum Chromo Dynamics
QED	Quantum Electro Dynamics
QGP	quark gluon plasma
r	distance from center of nucleus
R	nuclear radius
Reco	reconstructed simulation data
RHIC	Relativistic Heavy Ion Collider
ROOT	object oriented C++ library developed for particle physics analyses
SL4	Scientific Linux 4
SL5	Scientific Linux 5
SM	Standard Model
T	Tesla
w	weighting value
W	tungsten
y	rapidity
z	collision position along z-axis, *i.e.* z-vertex
ZDC	zero degree calorimeter

Overview

A new type of matter, the Quark Gluon Plasma (QGP, Sec. 1.2), is prostulated to have been created a few millionths of a second after the big bang. With the technology of particle accelerators, research at accelerator facilities like the Relativistic Heavy Ion Collider (RHIC) at Brookhaven National Laboratory and Large Hadron Collider (LHC) (Chap. 2) at CERN unveil the mysteries and beauty of this novel matter. These particle accelerators collide heavy ions like gold, copper, uranium and lead at close to the speed of light, creating the high energy and density environment similar to that after the big bang. The detectors placed on these accelerators record the collision events with sophisticated selection criteria (Chap. 3). The Compact Muon Solenoid (CMS) is one of these detectors at the LHC that has a mature calorimeter system measuring the energy of particles emitted from the collision point. The particles are grouped together into cones with different resolution parameters and these particle cones are referred to as “jets” (Sec. 1.3.2). They are considered as “hard probes” (high transverse momentum particles) for the QGP and they travel very fast while propagating through this hot QGP medium. Energy is dissipated as these “hard” particles transform into “soft particles”(low transverse momentum particles). As a result, the jet on one side of the back-to-back jet pair (see Fig. 1.9) which pushes through QGP farther will “lose” more energy than the jet on the other side. This is known as “jet quenching” and the quenching effects can characterize the behavior like viscosity of the QGP. It can be studied via various methods with different kinds of physical objects: heavy-particle suppression, di-hadron correlation, nuclear modification factor etc. This analysis focuses on the nuclear modification factor of jets (jet R_{AA}), which compares the jet yields in heavy-ion collisions to those in pp collisions where no quenching effects are found. It is defined as the ratio of the inclusive jet yields of PbPb to those of pp collisions with appropriate scaling due to the fact that not all the particles participate in the collisions depending on their collision geometry. Figure 1 is the nuclear modification factor result for charge hadron particle in STAR Experiment at RHIC. The central AuAu collisions give R_{AA} of less than 1, indicating the jet quenching, compared to that of deuteron+Au collisions above 1 with no indication of jet quenching [1]. This study at RHIC inspired the research in this thesis.

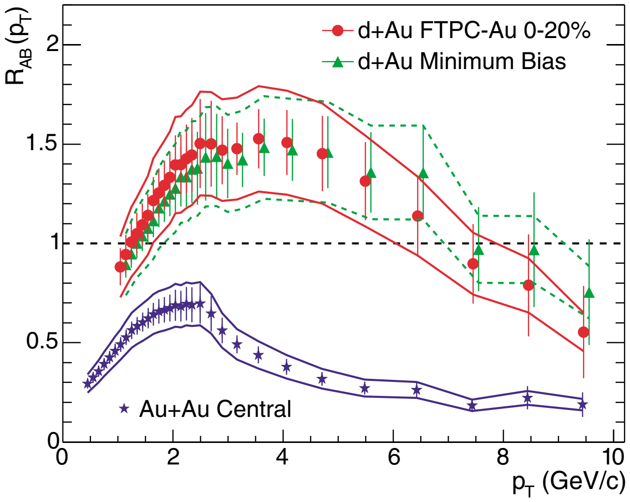

Figure 1: Charge hadron R_{AA} as a function of p_T at STAR Collaboration (RHIC). Adapted from [1]

However, the analysis in this thesis is a step forward from the results obtained from RHIC. It not only studies this type of quenching effects at a new statistical level but also provides a direct insight into the QGP with jets containing various particles, in comparison with the charged hadron particle nuclear modification factor studied at the RHIC. With a well-established reconstruction algorithm for jets (Chap. 4), the measured inclusive jets spectra (Sec. 5.1) can be produced for both pp and PbPb data samples within the event selection (Chap. 3). Monte Carlo simulated events (Sec. 4.1) are generated to construct resolution matrices that account for various jet resolution effects and to study systematic uncertainties (Chap. 6). The true jet spectra can be obtained through the correction for the measured jet spectra with the resolution matrix (Chap. 5).

The results are shown for anti-k_{T} particle flow jets with a resolution parameter of 0.3 using Bayesian unfolding correcting method (the main correcting method) in Fig. 2. For the most peripheral PbPb collisions, the jet R_{AA} is near unity, demonstrating the no-jet-quenching nature in the low particle multiplicity environment. The jet R_{AA} lowers with decreasing collision centrality in the range of jet p_T studied, indicating the jet energy suppression and creation of the QGP.

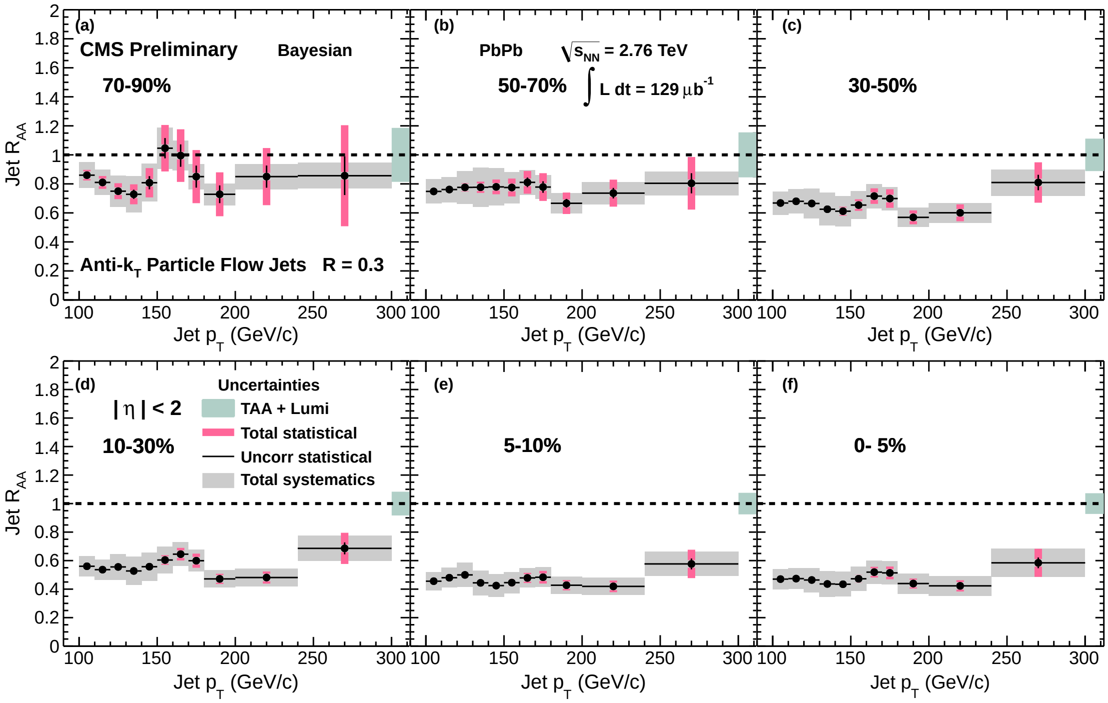

Figure 2: Bayesian unfolded jet R_{AA} for anti-k_{T} jets of R=0.3. Bars represent the uncorrelated statistical uncertainty, thin magenta vertical bands the total statistical uncertainty, and the wide grey band represents the systematic uncertainty. The overall combined uncertainty from T_{AA} and luminosity is represented as a green box above 300 GeV/c.

Chapter 1

Introduction

In this chapter, all the particles and their intrinsic properties within the standard model framkwork will be introduced in Sec. 1.1. The new type of matter, the Quark Gluon Plasma (QGP) created after the Big Bang, is the motivation for the research in this thesis and will be discussed in Sec. 1.2 followed by the introduction on jets in heavy-ion collisions in Sec. 1.3, which serves as a probe for this type of matter. This thesis explores the novel method to study the jet quenching effects with the nuclear modification factor, the definition of which is given in Sec. 1.4.

1.1 The Standard Model

The standard model (SM) emerged in the past century through the endeavor of many theoretical and experimental physicists leading to the discoveries of a variety of fundamental particles. The SM predicts that the universe is found to be composed of twelve blocks of fundamental particles categorized into quarks and leptons that are bound together by four fundamental forces carried by the gauge bosons [2].

1.1.1 Fundamental Particles

One category of fundamental particles is quarks, listed in Table 1.1. There are six different types or flavors of quarks (q) along with their antiquarks ($\overline{q}$). All

Table 1.1: Quarks [2, 3]

Quark	Symbol	Charge	Antiparticle	Anticharge	Mass (MeV/c^2)	Generation
up	u	+2/3	$\overline{\mathrm{u}}$	–2/3	1.7–3.3	1
down	d	–1/3	$\overline{\mathrm{d}}$	+1/3	4.1–5.8	1
strange	s	–1/3	$\overline{\mathrm{s}}$	+1/3	101	2
charm	c	+2/3	$\overline{\mathrm{c}}$	–2/3	1270	2
bottom	b	–1/3	$\overline{\mathrm{b}}$	+1/3	4190	3
top	t	+2/3	$\overline{\mathrm{t}}$	–2/3	172000	3

quarks (including quarks and antiquarks) can undergo a weak interaction and are divided into three generations based on mass and stability. In addition, since all quarks carry a charge, they can also all undergo an electromagnetic interaction with other charged particles, including fellow quarks and charged leptons, which will be discussed next. Interestingly, quarks carry an additional property called *color*, allowing them to interact via the strong force.

The main difference between a charged particle and its corresponding antiparticle is their opposite charge, with all other properties being identical. This results in a special relationship between them because, to obey conservation laws such as charge or momentum, a particle cannot be created from the vacuum (empty space) without its antiparticle. Particle-antiparticle pairs can also undergo a unique reaction called an *annihilation*, where the two particles annihilate each other with the release of energy, such as in

$$\mathrm{e}^- + \mathrm{e}^+ \rightarrow 2\gamma. \tag{1.1}$$

This annihilation is enabled by the energy released in the form of mass, as represented in Einstein's famous equation $E = mc^2$, where E represents energy, m mass, and c the speed of light. Neutral particles, like the photon and Z^0, are their own

Table 1.2: Leptons [2–4]

Lepton	Antiparticle	Charge	Mass (MeV)	Half-life (s)	Generation
e^-	e^+	± 1	0.511	∞	1
ν_L	$\overline{\nu}_L$	—	$(0 - 0.13) \times 10^{-6}$	∞	1
μ^-	μ^+	± 1	105.7	2.2×10^{-6}	2
ν_M	$\overline{\nu}_M$	—	$(0.009 - 0.13) \times 10^{-6}$	∞	2
τ^-	τ^+	± 1	1777	291×10^{-15}	3
ν_H	$\overline{\nu}_H$	—	$(0.04 - 0.14) \times 10^{-6}$	∞	3

antiparticles and consequently given the name *Majorana* particles.

The other category of fundamental particles is leptons and their antiparticles, listed in Table 1.2 . The electron (e) is the most commonly known lepton, also the lightest among six of them, which orbits the nucleus of atoms. The ν_L (Lightest), ν_M (Middle), ν_H (Heaviest), and their antiparticles are categorized as (anti)neutrinos and can each be *flavored* as an e, μ, or τ (anti)neutrino. For example an electron flavored neutrino would be ν_e. Leptons are divided into three generations, where, for the non-neutrino leptons, the lower the generation number, the smaller the mass and the more stable the particle. This is evident by reviewing their half-lives. This generation mass trend is generally observed for the neutrinos, but the current uncertainty in their mass determination causes their ranges to overlap. Additionally, all leptons are able to undergo weak interactions. However, only those that carry a charge are able to interact through the electromagnetic force via the photon. Regardless of the mediating force, all reactions involving leptons must conserve charge, lepton generation, and total lepton number, where leptons and their antiparticles have a lepton number of +1 and -1, respectively.

Gauge bosons are the force bearing particles that carry the *strong*, *weak* and

Table 1.3: Gauge Bosons [2, 3]

Gauge Boson	Interaction	Mass (GeV)	Strength	Range	Acts on
gluon	strong	0	1	10^{-15} m	hadrons
γ	electromagnetic	0	10^{-2}	$1/r^2$	electric charges
$W^{\pm}$, Z^0	weak	80.4, 91.2	10^{-5}	10^{-18} m	hadrons/leptons
graviton	gravity	0	10^{-39}	$1/r^2$	masses

electromagnetic forces. The gauge bosons for these forces are the *gluon*, $W^{\pm}$ and Z^0, and photon, respectively. Natures fourth known fundamental force, *gravity*, which is not incorporated into the SM and not yet experimentally confirmed, is theorized to be mediated by the *graviton*. Table 1.3 gives the gauge bosons with their physical properties.

Particles, including non-fundamental particles, can be classified into other groups as well. For example, (anti)quarks only coalesce into groups of three (qqq, $\overline{qqq}$) to produce (anti)*baryons* and a quark-antiquark pair ($q\overline{q}$), which is called a *meson*. The most commonly known baryons are the proton (p), composed of the *uud* quarks, and the neutron (n), composed of the *udd* quarks. Baryons and mesons are categorized into what are called *hadrons*, which are simply particles made of quarks that therefore interact via the strong interaction. Table 1.4 lists some well-known hadrons. Note in the table that despite being composed of fractionally charged quarks, all hadrons have an integer charge.

One other method of categorizing particles is to distinguish particles based on their spin (*fermions* and *bosons*). Fermions have 1/2 integral spin and bosons have integral spin. Since quarks have a spin of 1/2, baryons (qqq, $\overline{qqq}$) are fermions, while mesons ($q\overline{q}$) are bosons. Leptons have spin of 1/2 and are therefore fermions, while

Table 1.4: Baryons and Mesons [3]

Particle	Quarks	Charge	Spin	Mass (MeV)	Half-life (s)
p	uud	+1	1/2	938	$> 6.6 \times 10^{36}$
n	udd	0	1/2	940	885.7
π^+	$u\bar{d}$	+1	0	140	2.60×10^{-8}
π^-	$\bar{u}d$	–1	0	140	2.60×10^{-8}
K^+	$u\bar{s}$	+1	0	494	1.24×10^{-8}
K^-	$\bar{u}s$	–1	0	494	1.24×10^{-8}

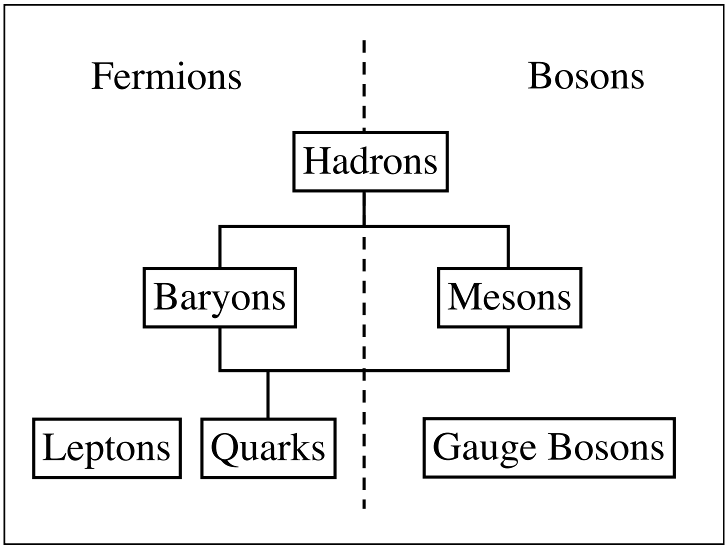

Figure 1.1: Particle classification hierarchy. Adapted from [2].

gauge bosons have integral spin and are bosons. Figure 1.1 shows a summary of the particle classification hierarchy.

1.1.2 Quantum Chromodynamics

The well-known theory of *Quantum Chromodynamics* (QCD) is weaved into the SM. It is the theory of the strong force, or “color force” as it is sometimes referred to, and describes the interactions of quarks and gluons. QCD describes the

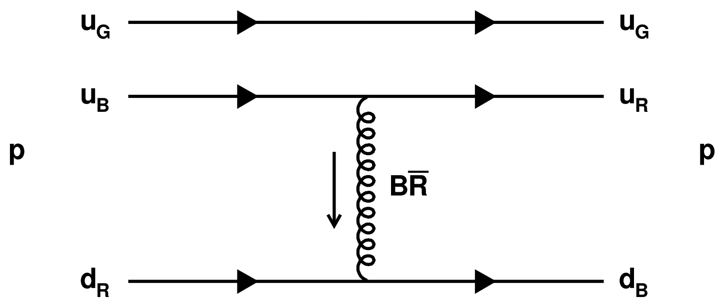

Figure 1.2: Feynman Diagram of a gluon interaction changing the color of two quarks in a proton. Here a blue-antired gluon is transferred from a u_B quark to a d_R quark, effectively swapping their color charge. Adapted from [2].

color charge inherent in both quarks and gluons, which manifests itself as the strong force. Quarks can have any one of three colors (*red*, *blue*, *green*), while antiquarks can have any one of three *anti*colors (*anti*red, *anti*blue, *anti*green). This is simply the name given to the property rather than the actual color. All hadrons are *colorless* or *color neutral*, meaning that (anti)baryons contain one quark of each (anti)color and mesons contain one quark of color and one antiquark with the corresponding anticolor, for instance red and antired. On the other hand, gluons simultaneously possess color and anticolor and their exchange can change the color of quarks, as shown in Fig. 1.2.

Via the mediation of the gluons, quarks are grouped together into hadrons such as the proton and neutron, which are the two *nucleons* that make up the atomic nucleus, with the exception of hydrogen and its proton only nucleus. As seen in Table 1.3, the strong force is significantly stronger than the other fundamental forces with the comparison of their relative strength. As matter of fact, it is so strong that its residual force is what binds nucleons together in the nucleus. However, its short range, also listed in the table, indicates that its influence is not sensible outside the nucleus.

This leads to one of QCD's most distinctive properties *asymptotic freedom*, which states that the strong force actually decreases in strength the shorter the distance between quarks, and grows in strength the larger the distance. This behavior is difficult to grasp, but one can relate it to stretching a spring. This makes another terminology definition necessary, *confinement*, meaning that quarks are confined to hadrons and cannot freely escape.

As illustrated in Fig. 1.3, if energy is added to a $q\overline{q}$ pair, the distance between the quarks will grow and the gluons holding them together will begin to "stretch", increasing the potential energy of the bond. If this process continues, eventually the potential energy between the $q\overline{q}$ pair will grow so great that the gluons will essentially "snap" with the simultaneous creation of a new $q\overline{q}$ pair in-between the original pair. The original quarks then form new quark pairs from the newly produced quarks; thus, relieving the system's stress by releasing energy. Hence, nature favors the creation of a new $q\overline{q}$ pair more than separating the original $q\overline{q}$ pair any further. This also explains why no individual quark has ever been experimentally observed. As stated before, this creation of new particles from the vacuum is possible due to Einstein's equation $E = mc^2$ and is the main driving force of particle production in particle accelerator collisions.

Though asymptotic freedom and confinement seem abstract, there is a significant amount of experimental evidence in the past few decades providing sufficient support to QCD and its fundamental physical properties.

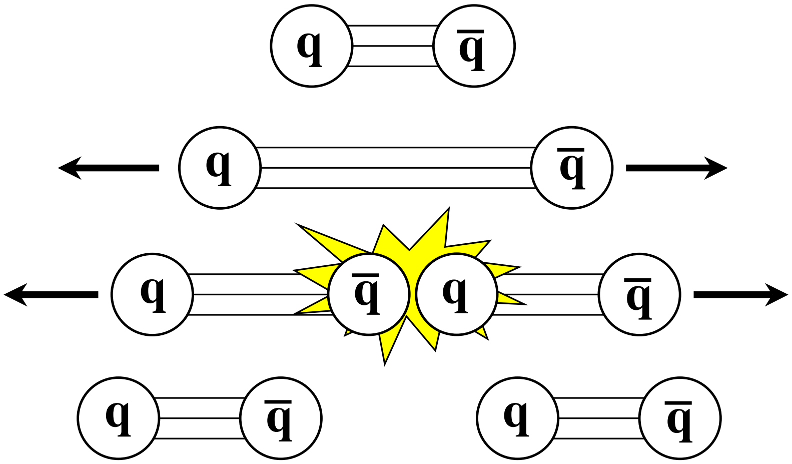

Figure 1.3: Illustration of quark confinement that leads to quarks being confined to hadrons, in this case mesons. See text for details. Adapted from [4].

One of the strongest pieces of evidence for quarks originates from deep inelastic scattering experiments [5–7], where inelastic indicates kinetic energy being lost or transferred between the reaction participants. In these experiments a high energy electron with a wavelength much shorter than the radius of a proton is collided with a proton in order to probe its internal structure. What these scattering experiments have shown is that the proton contains three point like particles, *i.e.* quarks, just as the SM predicted there would be.

Along with supporting the quark theory, reactions such as [8]

$$\mathrm{e}^- + \mathrm{p} \rightarrow \mathrm{e}^- + \mathrm{p} + \pi^0, \tag{1.2}$$

where a neutral meson is produced while the collision reactants are preserved, also supports the theory of QCD. The reaction does not make sense if protons are fundamental particles. Resorting to the QCD theory, however, solves the puzzle, as is illustrated in the Fig. 1.4 example. In (*a*) the incident electron inelastically scat-

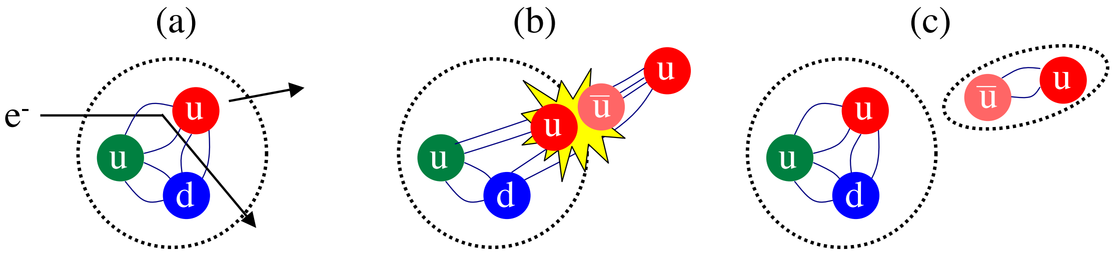

Figure 1.4: Illustration of confinement through the experimentally measured inelastic reaction $\mathrm{e}^- + \mathrm{p} \to \mathrm{e}^- + \mathrm{p} + \pi^0$. See text for a step-by-step explanation. Adapted from [9].

ters off one of the proton's u quarks, transferring some of its kinetic energy and "knocking" the u quark out of the proton. In (b), because of quark confinement, the ejected quark cannot freely escape the proton. Instead, the gluons in the proton stretch from the newly added energy until they escape from the confinement, triggering the production of a $u\overline{u}$ pair from the vacuum. In (c), the newly created $\overline{u}$ forms a π^0 with the ejected u and the newly created u replaces the ejected u in order to re-form the proton. This is a simple example illustrating confinement.

1.2 Quark Gluon Plasma

Nuclear matter exists in various physical phases, analogous to atomic matter. For atomic matter, these phases are often represented in a phase diagram with the variables of pressure and temperature. For nuclear matter, the variables are often temperature / energy and baryon density, which is simply the density of baryonic matter, *e.g.* protons and neutrons. Examples of these phase diagrams are shown in Fig. 1.5. At a low temperature, quarks and gluons are confined to hadrons, as illustrated in Fig 1.6(a). With increasing temperature, a phase change occurs

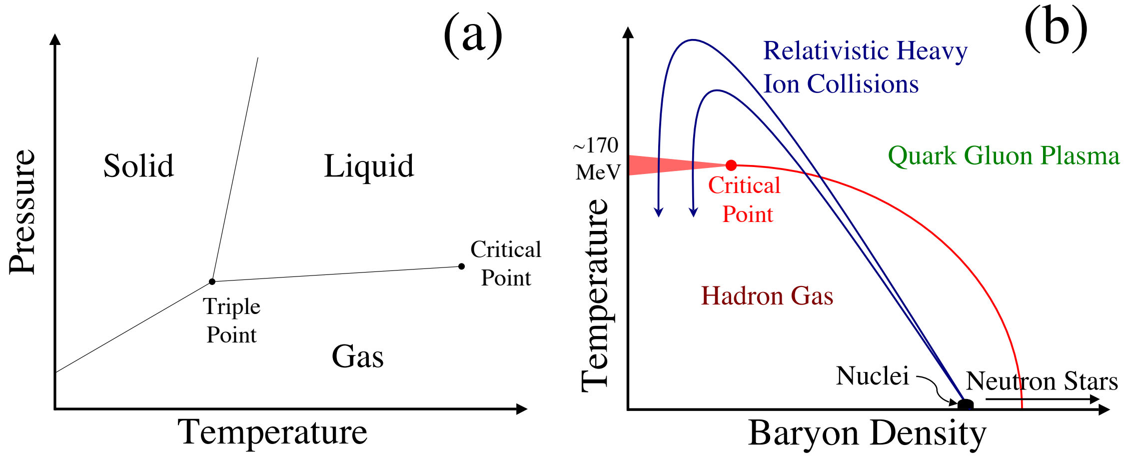

Figure 1.5: A typical phase diagram for (*a*) macroscopic atomic matter and (*b*) nuclear matter. Adapted from [10].

from vacuum to a nuclear gas, which is followed by a transition to a *quark gluon plasma* (QGP) phase that is characterized by the free movement of quarks and gluons beyond hadron boundaries. In this manner, the QGP phase is achieved due to an increase in parton density from particle production. If the density becomes great enough, hadronic boundaries will begin to blur allowing quarks and gluons to overcome hadron confinement. Once *deconfined*, the partons are able to move freely throughout the medium, as shown in Fig. 1.6(*b*).

Of special interest in the nuclear phase diagram is the critical point, whose conjectured position is displayed in Fig. 1.5(*b*). The critical point is the point where the properties of the hadron gas and QGP phases are so alike they are indistinguishable. To its right in the figure there is a sharp phase transition illustrated by the thin red line. To its left there is a smooth crossover between the two phases where both can coexist. This is signified by the broader red band.

A QGP was not obtainable in a traditional laboratory in the past so it was

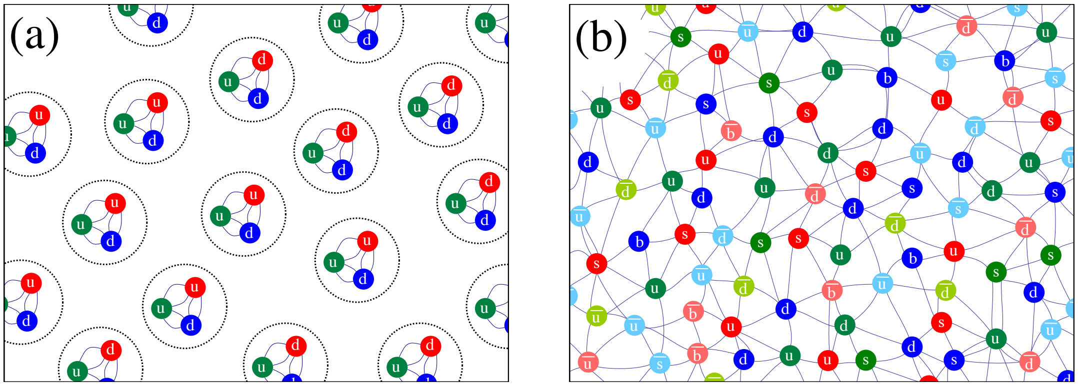

Figure 1.6: (*a*) The normal hadronic phase of nuclear matter where quarks and gluons are confined to hadrons. (*b*) Nuclear matter under extreme conditions of temperature, where quarks and gluons undergo a phase transition to a deconfined state of matter called a quark gluon plasma. In this phase quarks and gluons are no longer confined to hadrons, but are able to move freely throughout the medium. Adapted from [9, 11, 12].

in the realm of the theorists. Thanks to the commissioning and running of several new particle accelerators [13–15], this new phase of matter can now be studied via the collisions of heavy-ions, including copper, gold, lead etc. The next section will focus on these collisions and the evolution of the medium they create.

In principle, two approaches can be taken to access the QGP region of the nuclear phase diagram. The first approach is to increase the baryon density by compressing the nuclear matter at an extremely low temperature. However, these conditions cannot be created in today's laboratories, but can only be done with the large gravitational force of neutron stars. The second approach involves increasing the temperature of the nuclear matter to $\sim$170 MeV[1] $\approx 2 \times 10^{12}$ Kelvin (K) [16], where a phase transition to a QGP is theorized to occur. This is equivalent to an energy density of $\sim$1 GeV/fm^3 or about an order of magnitude higher than

---

[1] One eV is the amount of kinetic energy gained by an electron after being accelerated through a potential difference of 1 volt.

cold nuclear matter (0.14 GeV/fm^3 [17]). As indicated in Fig. 1.5(b), this can be achieved in the laboratory with particle accelerators that collide heavy ions at nearly the speed of light. For instance, the Large Hadron Collider (LHC) accelerates lead (Pb) nuclei (82 protons, 126 neutrons, and 0 electrons) to 1.38 TeV/nucleon, close to the speed of light. At that energy, the spherical nuclei when at rest would be longitudinally flattened due to *Lorentz Contraction*[2] into an oblate spheroid or thin "disk" when viewed from the laboratory's frame of reference. Once this energy is achieved, the nuclei are then collided with a beam of oncoming Pb nuclei of the same energy, for a total center-of-mass energy per nucleon pair ($\sqrt{s_{NN}} =$) 2.76 TeV. (Any reference to a beam energy will be assumed to be in the context of $\sqrt{s_{NN}}$ unless otherwise specified in this thesis.) When they collide, the nuclei have a temporary mean energy density far above the predicted 1 GeV/fm^3 necessary for creating a QGP, this energy density is fleeting and quickly wanes as the nuclei finish passing through and interacting with one another.

In this process, the nuclei become excited and begin to fracture and dissipate, while at the same time radiating particles in their wake. More particles are then created through the particle production described in Sec. 1.1.2. If the overlap between the nuclei is large during their crossing, then thousands of particles will be created. These particles generally have a momentum of $\lesssim 3$ GeV/c and are said to come from *soft* physics, while higher momentum particles, called *jets*, come from *hard* physics. Jets are formed via the elastic or hard scattering of quarks or gluons from the original nuclei and are characterized by a large momentum transfer away

---

[2] For a detailed discussion of Lorentz Contraction see Appendix A.

from the beam direction. To conserve momentum these high momentum particles are often created in pairs called *di-jets* that traverse the newly created medium undergoing gluon radiation, which is similar to the Bremsstrahlung[3] radiation electrons can experience in QED. As the jets exit the medium they fragment due to confinement, producing a cone shaped cluster of particles. Intuitively, jets are created in pairs, but they can also be formed in triplets or in multiple directions to conserve energy. Another particle production mechanism is gluon fusion where two gluons can fuse to create heavy particles such as the J/ψ ($c\bar{c}$). After the new particle production, the original particles together with the new particles can interact with the newly produced medium, enabling us to probe the beauty of QGP with some of the phenomenon triggered by this kind of interaction such as "jet quenching". More details of jets will be discussed in Sec. 1.3.2.

From various types of particle productions, the particle density of the medium begins to increase , leading to the blurring in the hadronic boundaries of the particles and weakening of quark confinement. If the particle density becomes sufficiently high, deconfinement will occur resulting in a QGP. This phase was illustrated in Fig. 1.6(b), where the quarks and gluons are shown to no longer be bound as hadrons, but able to move freely throughout the system.

Throughout the process described above, the medium is constantly expanding and undergoing binary collisions between the particles. If these particles are strongly interacting then they may result in a quick thermalization of the system before it

---

[3] Bremsstrahlung radiation is the emission of a photon from a particle, mainly an electron or positron, due to an acceleration that deviates the particle from its straight-line course. The acceleration can be caused by an attraction to a nucleus as the particle traverses a medium or a man-made magnetic field in a particle accelerator.

"evaporates". Via experiments and model prediction, it is estimated that the system does achieve a rapid thermalization after ∼0.15–0.6 fm/c with a temperature of ∼300–600 MeV ≈ 3.5–7×10^{12} K [4]. This corresponds to an energy density of $\gtrsim$ 9 GeV/fm^3, well above the estimated QGP phase transition of ∼1 GeV/fm^3 and ∼170 MeV.

As the system continues to evolve it further expands resulting in a more diffuse system with a smaller energy density. Eventually the energy density becomes small enough that there is a phase transition from the QGP to a hadron gas. This process is called *hadronization* and is where confinement exerts power over particles and free (anti)quarks and gluons no longer exist. With continued expansion of the system, the temperature of the system decreases, inelastic scattering ceases to occur, resulting in a *chemical freeze-out*, where the quark flavors inside the hadrons are frozen and no longer change due to scattering. The last stage of the collision is called *thermal freeze-out* and at this point the hadrons and leptons are so dispersed that they no longer interact in any manner, resulting in their properties being fixed unless they undergo a weak decay. From here, the particles, such as the colorless hadrons, propagate to detectors where their angular and momentum distributions get recorded. Note that only these colorless particles are detectable in the detector and the colored particles before this phase are only theorized and are not observables in these physics experiment. Figure 1.7 briefly illustrates the main stages of the collision evolution.

---

[4] For comparison, this is ∼2.2–4.4×10^5 times hotter than the center of the sun [18].

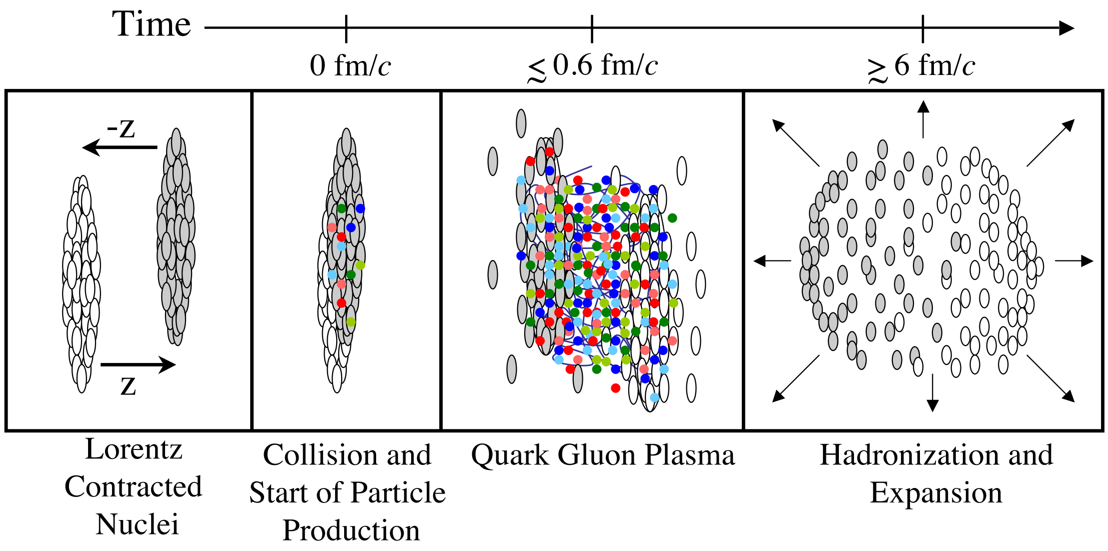

Figure 1.7: Evolution of a heavy-ion collision from *left→right*: (1) Lorentz contracted nuclei composed of colorless (white) hadrons move toward one another. For distinction those hadrons moving in the $-z$ direction are tinted gray. (2) Nuclei collide, become excited, and particle production begins. (3) After $\lesssim$ 0.6 fm/c the original nuclei are dissociating and a QGP is created from the produced particles. (4) The medium expands, cools, and after $\sim$6 fm/c, hadrons reform, followed by chemical and thermal freeze-out and finally detection. Adapted from [19].

1.3 Heavy-ion Collisions

Heavy-ion collisions are essential in probing the QGP. The event characterization will be discussed in Sec. 1.3.1 . A myriad of methods have been employed to probe its properties, such as utilizing di-hadron correlation, J/ψ suppression, nuclear modification factor, etc. The definition of the jet nuclear modification factor, which is the focus of this thesis, is found in Sec. 1.4.

1.3.1 Event Characterization

It is critical to have an understanding of the characteristics of a heavy-ion event in order to probe the formation of the QGP. The position and the vertex of the collision are usually described by a Cartesian coordinate system (x,y,z) in the laboratory frame, with the collision point set as (0,0,0) and z as the beam-line by convention. The positioning of an emitted particle can also be described by polar coordinates, where the angle of the emitted particle with respect to the beam-line (z) is represented by θ and the projected angle of the particle on the (x,y) plane is noted by ϕ. Rapidity (y) is a dimensionless variable describing the velocity of a particle with respect to the collision point, formulated as

$$\mathrm{y} = \frac{1}{2}\ln\frac{1+\frac{v}{c}\cos\theta}{1-\frac{v}{c}\cos\theta} = \frac{1}{2}\ln\frac{1+\frac{v}{c}_z}{1-\frac{v}{c}_z}, \tag{1.3}$$

in which v is the velocity of the travelling particle and c the speed of light.

Utilizing the polar coordinate system provides the advantage of understanding another variable pseudo-rapidity η. The mathematical definition of rapidity requires the velocity of the particle to be able to do the calculation, which is quite a challenge. However, with the known parameter θ, the pseudo-rapidity can be derived from the following formula:

$$\eta = \frac{1}{2}\ln\frac{1+\cos\theta}{1-\cos\theta} = -\ln[\tan\frac{\theta}{2}]. \tag{1.4}$$

Assuming the emitted particle travels at nearly the speed of light, η and y will become equivalent. In this sense, η will be used in this analysis to describe the positioning of the particle. The relationship between η and θ is illustrated in Fig. 1.8. A more thorough description of y and η can be found in Appendix B

The challenge of utilizing rapidity is the particle identification for the sake of

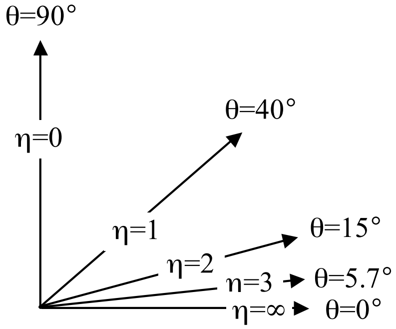

Figure 1.8: The relationship of η-θ

obtaining its velocity. In this sense, using pseudo-rapidity provides the advantange of acquring the particle position information without the need of identifying it in the first place.

1.3.2 Jets

One of the experimental signatures of the QGP formation is the attenuation or disappearance of the spray of hadrons resulting from the fragmentation of a hard scattered parton having suffered energy loss, i.e., "jet quenching" [20]. A jet is the collimated set of hadronic decay products of a parent parton. Parton is a collective term for quarks and gluons in general. The energy lost by a parton in a medium provides fundamental information on its thermodynamical and transport properties (see [21] for reviews). To a first approximation, a jet can be considered as a hard parton that has undergone soft and collinear showering and then hadronization. Jets are used both for testing our understanding and predictions of high-energy QCD processes.

Figure 1.9 is the illustration of a back-to-back dijet pair in a heavy-ion collision.

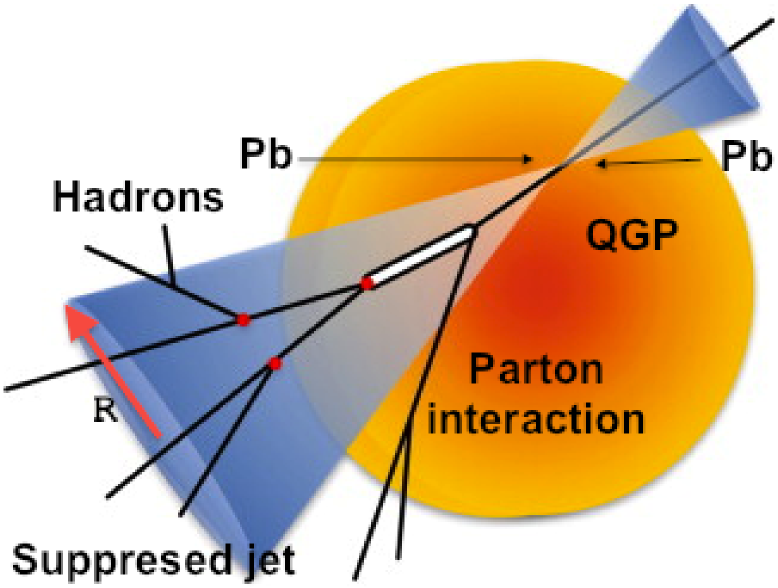

Figure 1.9: Di-jet event in heavy-ion collision. The orange-shaded circle is the animanted QGP. The dark lines inside each cones represent the particles inside the jet. The red arrow is the resolution parameter R, defined as the radius of the cone. The particles in the jet pair originate in the violent scatterings of gluons or light quarks. Adapted from [22].

The two jets are separated in the azimuthal angle ϕ larger than 3 in radians. The red arrow is the radius of the jet cone, R. The particles in the jet pair originate in the violent scatterings of gluons or light quarks (up, down, or strange). Particles that interact via the strong interaction (quarks and gluons) are expected to lose a significant fraction of their energy while propagating through the QGP. Therefore, the jet on the side with the particles trying to propagate through the QGP further is more severely suppressed in p_T compared with that on the other side. This is commonly referred as "jet quenching". It serves as a quantitative probe for the QGP because this medium-induced energy loss largely depends on the density of the medium (the QGP).

Jet momentum is determined as the vectorial sum of all particle momenta within the selected jet. The type of jets can be categorized into three levels with respect to the timeline of their formation: parton, particle, and reconstruction level. The parton jet is a conceptual object instead of an experimental observable, corresponding to the single parton from which the jets evolves. The particle level jets, commonly referred to as the truth jet or generator level jets, are the observable stream of particles sprayed out of the collision point. The reconstruction level jets, for instance, calorimeter level jets, further indicate where and how these particle level jets were observed inside the detector.

Due to the limitation of center-of-mass energy and statistics, RHIC was able to research “jet quenching” through charged hadron particles that form the jets. With a much higher collision beam energy and more statistics, LHC provides an opportunity to further investigate this phenomenon. The leading hadron measurements are preferentially from the population of jets that has the least interaction with the medium. These measurements are not sufficient to discriminate quantitatively between partonic energy loss models and to extract key parameters, such as the transport coefficient of the hot medium to measure the stopping-power of the QGP precisely [23]. The most recent CMS (Compact Muon Solenoid) experimental results from PbPb collisions demonstrated the jet reconstruction capabilities of the detector system and showed that dijets become increasingly imbalanced compared to those observed at RHIC [24, 25]. In this thesis, the method of studying the jet quenching is by comparing the jet yields between proton+proton and heavy-ion collisions to quantify the modification in the QGP.

1.4 Nuclear Modification Factor R_{AA}

For the most central collisions, a significant fraction of the "lost" jet energy is observed to be radiated via low transverse momentum (p_T) particles outside the jet cone. To gain sensitivity to the properties of the QGP and to quantify the underlying mechanism of the quenching effects, the ratio of inclusive jet yields per event in PbPb collisions(dN^{AA}_{jets}) over the ones in pp(dN^{pp}_{jets}) is studied via the jet nuclear modification factor (R_{AA}), formulated as

$$R_{\mathrm{AA}} = \frac{dN^{AA}_{jets}/dp_T}{< N_{\mathrm{coll}} > dN^{pp}_{jets}/dp_T} = \frac{dN^{AA}_{jets}/dp_T}{< T_{\mathrm{AA}} > d\sigma^{pp}_{jets}/dp_T}, \tag{1.5}$$

in which $< N_{\mathrm{coll}} >$ is the average number of nucleon-nucleon collisions occurring in heavy-ion (AA) collisions. The effective overlap area in which a specific nucleon A can interact with another given nucleon A is defined as T_{AA}. It is called the nuclear overlap function, calculated from a Glauber model (see Sec. 3.2.4) and formulated as $< T_{\mathrm{AA}} > = < N_{\mathrm{coll}} > /\sigma^{NN}_{\mathrm{inel}}$ with $\sigma^{NN}_{\mathrm{inel}}$ being the cross section of inelastic nucleon collisions. The detailed mathematical deduction of this definition can be found in [26].

If the full jet energy is recovered inside the jet cone, independent of the fragmentation details, even in the presence of strong jet quenching, this ratio should be equivalent to one. If the ratio is less than one, it would suggest broadening of the jet structure due to jet-medium interactions. The measurements of nuclear modification factors has the potential to differentiate between competing models of parton energy loss mechanisms, hence reducing the large uncertainties introduced by different theoretical formalisms [27].

Chapter 2

Experimental Overview

The Large Hadron Collider (LHC) is described in Sec. 2.1. As the biggest particle accelerator on earth, it not only provides a platform for new physics, but also extends our horizon of the existing theories and experiments, such as Quark Gluon Plasma and jet quenching. Section 2.2 focuses on the general purpose detector installed at the Large Hadron Collider, the Compact Muon Solenoid(CMS), from which all the data was acquired for this analysis.

2.1 Large Hadron Collider

The Large Hadron Collider (LHC) was built at the French-Swiss border near Geneva with a circumference of 27 kilometers (Fig. 2.1). In 2009, this world's highest-energy accelerator was put into operation. Compared to the Tevatron, the beam energy of the LHC increases from 1 TeV to 7 TeV for proton-proton collision. Figure 2.2 is a beam injection layout for the LHC with four detectors installed on different points in the main ring to record the collisions, including A Toroidal LHC Apparatus (ATLAS), Compact Muon Solenoid (CMS), LHC beauty (LHCb) and A Large Ion Collider Experiment (ALICE). Not only the search for the missing piece of the standard model, the Higgs Boson, is significant; the physics beyond the standard model, and the QGP are as well important physics topic addressed by the

LHC. This has opened up a new discovery era that is currently being vigorously explored by the first long run with PbPb collisions at $\sqrt{s_{NN}} = 2.76$ TeV. The top LHC energy of $\sqrt{s_{NN}} = 5.5$ TeV exceeds that of RHIC by almost a factor of 30. CMS and ATLAS are the two large general-purpose detectors located at Point 5 and inside the SPS, respectively. The primary purpose of LHCb is to study the anti-matter and bottom quarks. ALICE focuses on the research of the QGP. This thesis focuses on the analysis and results generated from the CMS experiment.

Initially the two beams are pre-accelerated by the PS, SPS, LINAC2 (for protons) and LIER (for lead), enter the main ring with the two beams travelling counter-directed, and then are accelerated to a higher energy until the collisions. The beam parameters for PbPb collisions are shown in Table 2.1 with data extracted from [28].

Table 2.1: Beam Parameters of Lead-Lead Collisions in LHC in Peak Luminosity

Beam Parameters	Injection	Collision	Unit
Lead ion energy E	36900	574000	GeV
Lead ion energy/nucleon E	177.4	2759	GeV
Number of ions per bunch N	7×10^7		
Number of bunches N	592		
Circulating beam current I	6.12		mA
Peak Luminosity at IP2 L	1×10^{27}		$cm^{-2}s^{-1}$

2.2 Compact Muon Solenoid Detector

A diagram of the Compact Muon Solenoid (CMS) apparatus can be seen in Fig 2.3. It is composed of a superconducting solenoid of 6-m internal diameter,

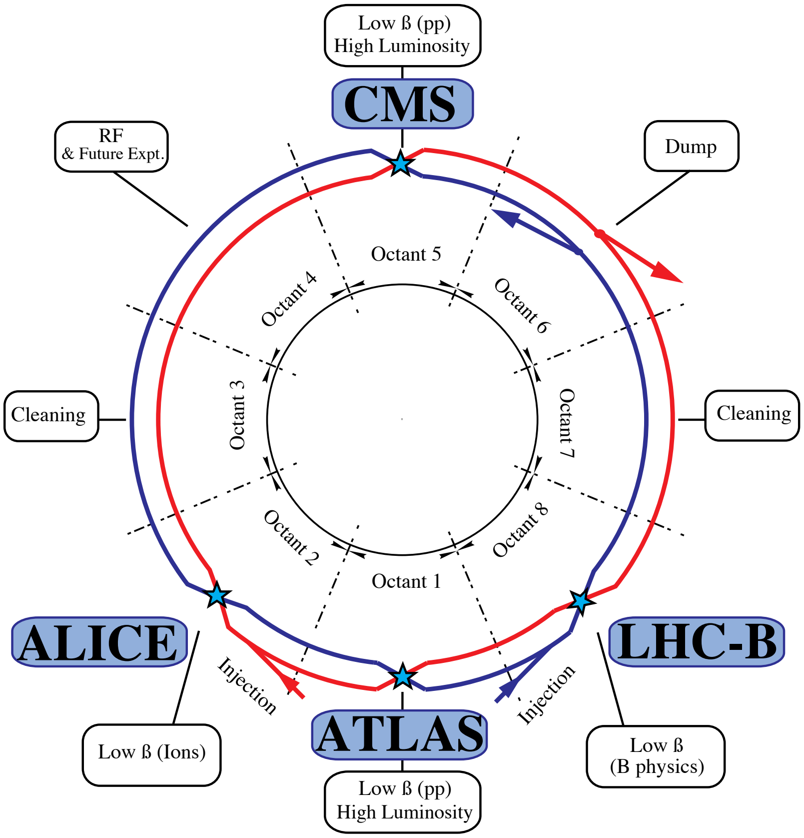

Figure 2.1: LHC physical layout.

providing a magnetic field of 3.8 T. It has an overall length of 22 m, a diameter of 15 m, and weighs 14,000 tonnes. Within the field volume are a silicon pixel and strip tracker, a lead tungstate crystal electromagnetic calorimeter (ECAL), and a brass/scintillator hadronic calorimeter (HCAL). Muons are measured in gas-ionization detectors embedded in the steel return yoke with nearly 1 million electronic channels. Extensive forward calorimetry complements the coverage provided by the barrel and endcap detectors. The zero degree calorimeter (ZDC) and centauro and strange object research (CASTOR) calorimeters are made of quartz fibers/plates

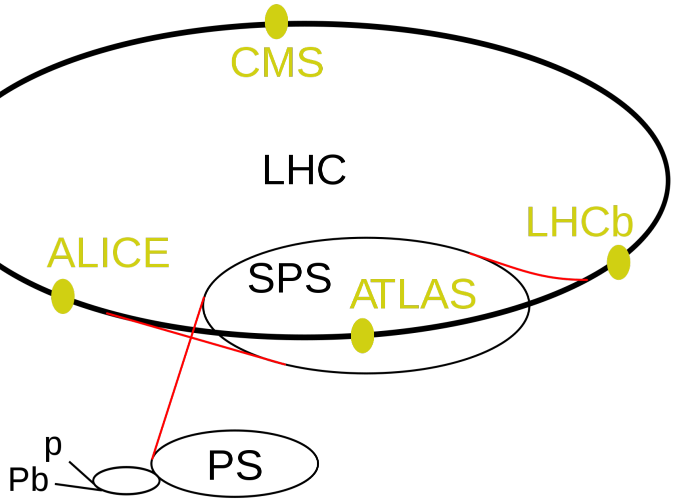

Figure 2.2: LHC injection system layout. Proton and lead ions are pre-accelerated in linear accelerators, then injected into the Proton Synchrotron (PS) and Super Proton Synchrotron (SPS), and finally injected into the main ring. Four detectors are shown here, including ALICE, ATLAS, CMS, LHCb.

embedded in tungsten absorbers. In total, there are $\sim 10^8$ data channels checked in each bunch crossing.

CMS uses a right-handed coordinate system, with the origin at the nominal interaction point, the x axis pointing to the center of the LHC, the y axis pointing up (perpendicular to the LHC plane), and the z axis along the anti-clockwise-beam direction. The polar angle θ is measured from the positive z axis and the azimuthal angle ϕ is measured in the x-y plane. The ECAL has an energy resolution of better than 0.5% for unconverted photons with transverse energies above 100 GeV. The HCAL, when combined with the ECAL, measures jets with a resolution $\Delta E/E \approx 100\%/\sqrt{E\,[GeVns]} \oplus 5\%$. $\oplus$ indicates a sum of quadrature. Figure 2.4 is a diagram describing the pseudo-rapitidy range of each sub-detector in CMS. In the region $|\eta| < 1.74$, the HCAL cells have widths of 0.087 in pseudorapidity and 0.087 in

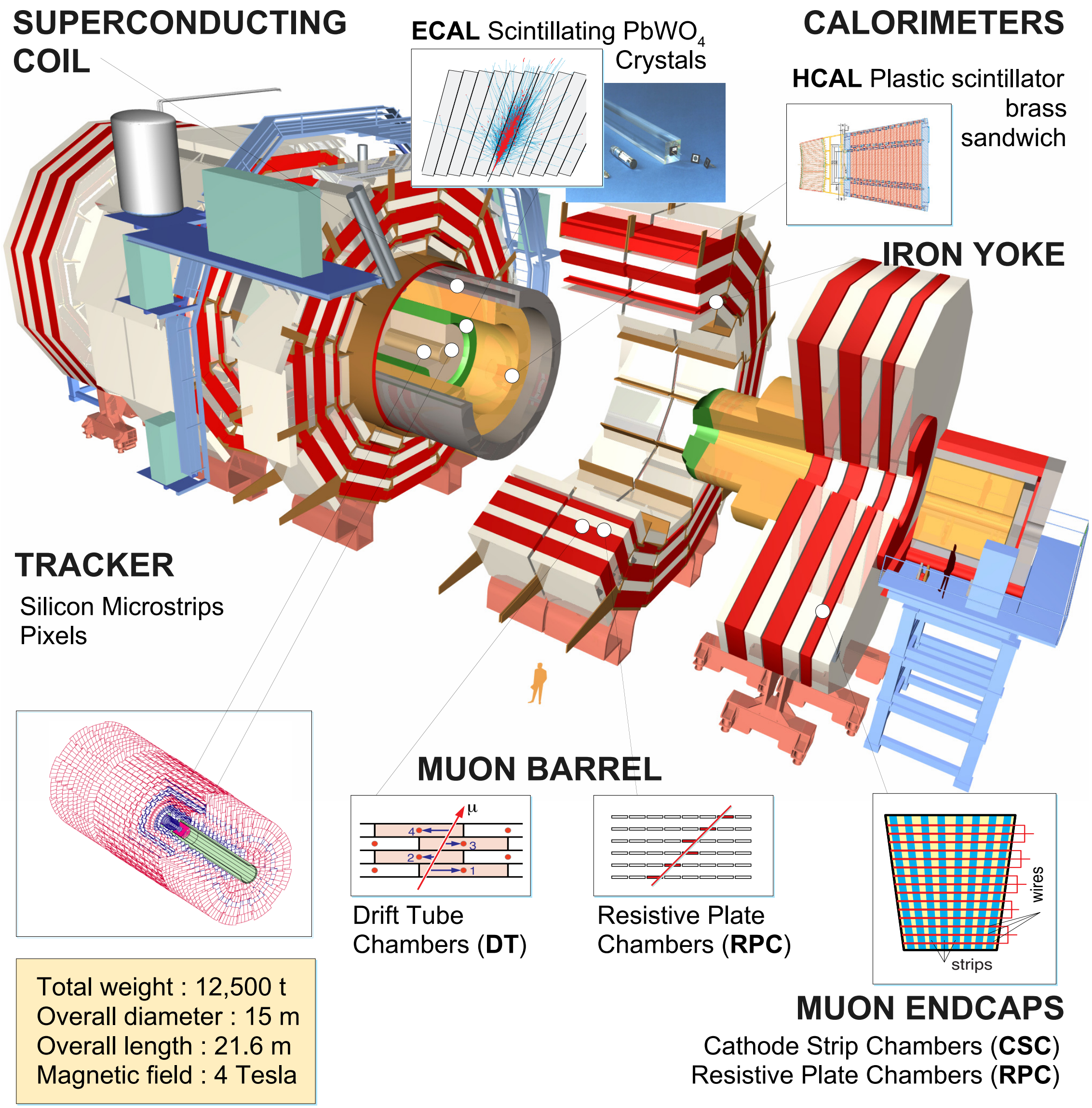

Figure 2.3: CMS detector and sub-detectors

azimuth (ϕ). In the η-ϕ plane, and for $|\eta| < 1.48$, the HCAL cells map onto 5×5 ECAL crystal arrays to form calorimeter towers projecting radially outwards from close to the nominal interaction point. At larger values of $|\eta|$, the size of the towers increases and the matching ECAL arrays contain fewer crystals. Within each tower, the energy deposited in ECAL and HCAL cells are summed to define the calorimeter tower energies, subsequently used to provide the energies and directions of hadronic jets.

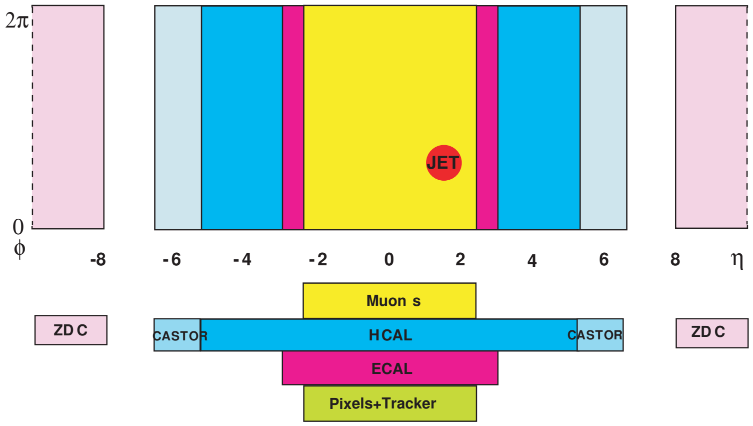

Figure 2.4: CMS Acceptance. Jets are mostly collected within HCAL and ECAL of $|\eta| < 2$.

Figure 2.5 is the transverse view of the detector. The energy of photons is directly obtained from the ECAL measurement. The energy of electrons is determined from a combination of the track momentum at the main interaction vertex, the corresponding ECAL cluster energy, and the energy sum of all bremsstrahlung photons attached to the track. The energy of muons is obtained from the corresponding track momentum. The energy of charged hadrons is determined from a combination of the track momentum and the corresponding ECAL and HCAL energy, and calibrated for the nonlinear response of the calorimeters. Finally, the energy of neutral hadrons is obtained from the corresponding calibrated ECAL and HCAL energy.

The first heavy-ion event in CMS was observed in November 2010 and is shown in Fig 2.6. The orange lines represent the trajectories of particles recorded by the tracker system. The green towers are the ECAL and HCAL energy deposits

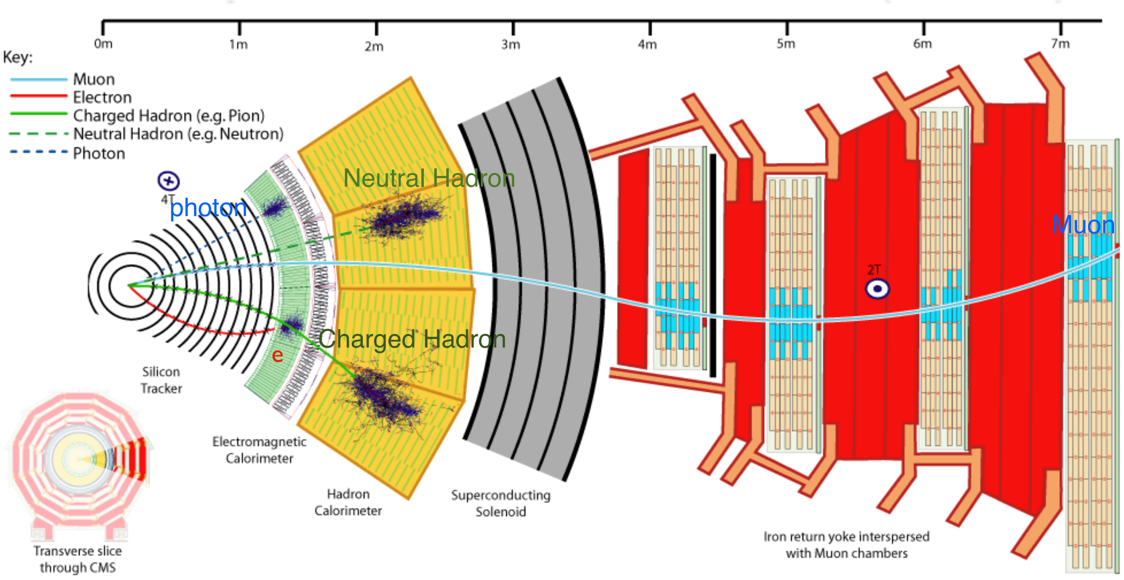

Figure 2.5: The transverse view of CMS detector

reconstruction of the particles.

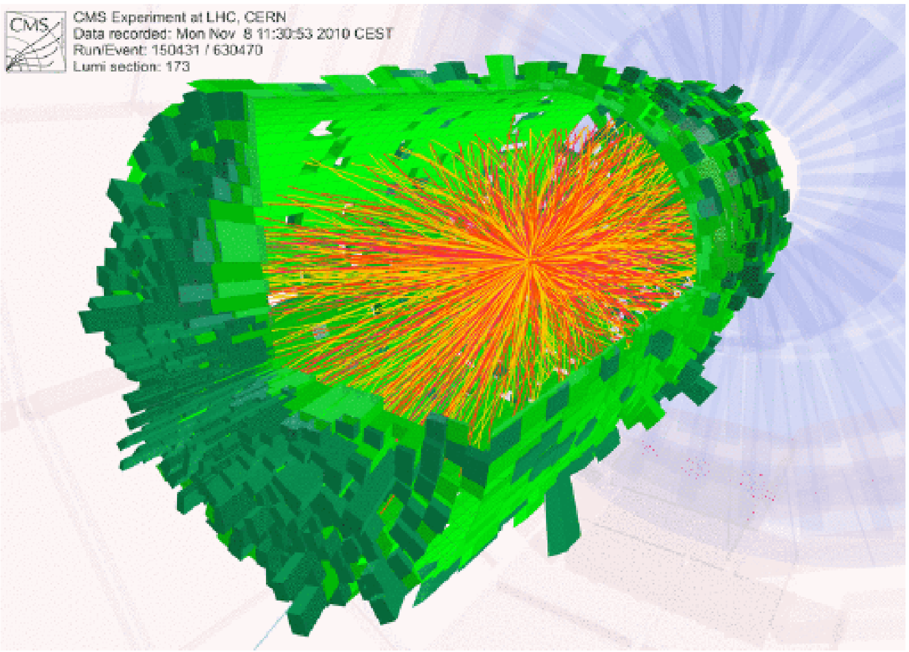

Figure 2.6: First heavy-ion event in CMS at $\sqrt{s_{NN}} = 2.76$ TeV collected in 2010. The orange lines demonstrate the particle trajectories reconstructed from the collision events. The green towers are the reconstructed energy from the calorimeter towers.

Chapter 3

Event Selection

To obtain a clean dataset, an efficient trigger system is used in CMS. Section 3.1 discusses the first level (L1) of the CMS trigger system, composed of custom hardware processors, and using information from the calorimeters and muon detectors to select the most interesting events in a fixed time interval of less than 4 μs. In Sec. 3.1.3, the High Level Trigger (HLT) processor farm, which further decreases the event rate from around 100 kHz to around 300 Hz before data storage, will be covered. Other offline selection criteria will be further assessed including Hadronic Calorimeter noise removal and leading track jet identification in Sec. 3.2.1 and Sec. 3.2.2, respectively. The discussion of luminosity for both pp and PbPb collisions and the datasets used in this thesis are given in Sec. 3.2.3. The details of centrality determination for the PbPb events can be found in Sec. 3.2.4.

3.1 Online Selection

In order to select the events of interest and save the recording space of the detector, a sophisticated trigger mechanism has been established. The trigger strategy of CMS for PbPb collisions was constrained by the long (10–200 microseconds - depending on the run/date) holdoff time (during which the trigger is ignored) imposed by the pixel detector (on average introducing about 1.7% of deadtime), issued after all accepted L1 trigger signals, and by the overall rate limitations of about 300 Hz (physics) for recording events, constrained mainly by the volume of data produced due to the high occupancy of the Silicon Strip Tracker and storage limitations downstream. The hadronic collision rate varied between 5 Hz and ~ 4000 Hz, depending on the number of colliding bunches (between 2×2 and 358×358) and on the varying bunch intensities. For these reasons, the L1 trigger system had to provide a very efficient and clean trigger on hadronic collisions, with prescale for minimum bias events, meaning the minimum bias events are partially recorded for the sake of recording space, and no prescale for high-p_T jets, muons, or photons.

3.1.1 Types of Collisions and Available L1 Triggers

The CMS apparatus has various ways to trigger on PbPb collisions. The expected cross section for hadronic inelastic collisions is 7.65 barns, while ultraperipheral collisions (UPC) with large impact parameters lead to the breakup of one, or both, Pb nuclei with a much larger probability. (more than 200 barns for one or more neutrons in one ZDC and the cross section for ZDC coincidences is almost twice the hadronic interaction rate.) Collisions in which the Pb nuclei interact hadronically can produce anywhere from just a few up to about 1600 particles per unit pseudorapidity, depending on the impact parameter. As a result, more than 95% of these collisions produce double-sided (coincidence) trigger signals in the Beam Scintillator Counters (BSC), and in the Hadronic Forward (HF) calorimeters. In addition, most of collisions are also detected by coincidences in the ZDC. About

75% of the hadronic collisions also fire the BSC High Multiplicity trigger. In order to suppress non-collision related noise, cosmics, radioactivity, trigger afterglow, and beam background, all of these triggers were protected by the BPTX coincidence, i.e. two colliding ion bunches were required to be present in coincidence with each of these triggers.

In 2011, the collision rate was 1–8.4 Hz per colliding bunch pair during the PbPb data taking period. Therefore (taking into account the 11245 Hz orbit frequency) the average number of collisions per bunch crossing was $0.9 - 7.5 \times 10^{-4}$. The effect of pile-up is negligible in this analysis.

In contrast to nuclear interactions, only a small fraction of UPC collisions were found to be able to activate the HF and BSC coincidence triggers. However, they contribute significantly to coincidence and singles triggers in the ZDC. The additional trigger rate for these coincidence triggers from UPC collisions is comparable to that from hadronic collisions, while the single sided rates (which have very low or no noise) are more than an order of magnitude higher than the hadronic collision rate. For these reasons, the BSC and HF coincidence triggers are used to select hadronic PbPb collisions. These triggers have low noise (fake) rate (less than 1 Hz with two non-colliding beams at full intensity with 358 bunches), but very high efficiency.

3.1.2 Selecting Minimum Bias Collisions

As described in the beginning of Sec. 3.1, minimum bias (hadronic inelastic) collisions were selected by the L1 trigger system. Two clean and highly efficient triggers were used. One of them was the BSC coincidence "threshold 1", which requires at least one segment firing on each side of the interaction point. The minimum bias trigger was "L1 Algorithm 126" ("L1_HcalHfCoincPmORBscMinBiasThresh1_BptxAND"). The latter trigger bit is based on HF, and requires at least two HF towers to have deposited energies that exceed the threshold set by the firmware. It has similar efficiency as the BSC coincidence, and is also noise-free, but adds some small additional rate (efficiency) to detect minimum bias collisions. It is also more in line with (but less strict than) the offline event selection, which uses HF as well. Finally, in case either the BSC or the HF detector develops a problem, the use of an OR allows "L1 Algorithm 126" to continue to record minimum bias collisions. For instance, the HF trigger was not correctly timed in and arrived too early in the beginning of the run. The HF trigger efficiency decreased dramatically. The BSC based trigger does not only help trigger on the collisions but also to diagnose this problem.

3.1.3 Collisions With High Energy Jets

The minimum bias trigger was unprescaled at L1 level before reaching about 60 Hz collision rate, and then it was prescaled, depending on the collision rate, to fit into the 300 Hz total HLT physics trigger limitation. The HLT passed all of these (prescaled) minimum bias events through to the HIMinBiasUPC data stream.

The Minimum bias triggered sample was used to check the jet trigger efficiency. Since the minimum bias triggers in PbPb collisions are prescaled, making use of the jet triggers at the L1 and HLT levels is necessary to keep the full jet statistics. In the L1 trigger, two jet triggers were enabled: L1_SingleJet36_BptxAND and L1_SingleJet52_BptxAND. The HLT trigger HLT_HIJet80 used in this analysis was seeded by the L1 bit L1_SingleJet52U_BptxAND. The online jet reconstruction and the p_{T} cut done at the HLT reduced the rate of the trigger, with respect to the rate of the L1 seed, by a factor of about 1010, for thresholds of 80 GeV/c. The rate of the jet trigger with a threshold of 80 GeV/c did not exceed a few Hz. The trigger that was finally used to select events for the analysis is HLT_HIJet80, for the reason that it was never prescaled in the easily accessible HIHighPt dataset. The HLT_HIJet80 has a low enough threshold to be able to record all events with an offline reconstructed jet of 100 GeV/c or greater in an unbiased fashion, which is the primary set of events used in this thesis.

In pp collisions, the trigger used for jet selection is HLT_Jet60. This trigger is based on the anti-k_{T} calorimeter based jet finding algorithm with resolution parameter of 0.5, and performs at 100% for jet $p_T > 90$ GeV/c.

The efficiency (turn-on) curve for the HLT_HIJet80 trigger is shown in Fig. 3.1. The efficiency is the ratio of the number of triggered events over the number of minimum bias events, as a function of the p_T of the leading jet with $|\eta| < 2$. It is important to note that the HLT_HIJet80 trigger uses the iterative cone calorimeter jet algorithm with a 0.5 radius and pileup subtraction (icPu5Calo). The offline analysis, as described in Sec. 4.2, uses anti-k_{T} particle flow jets with pileup subtraction and resolution parameter of 0.2, 0.3, or 0.4 (akPu2PF, akPu3PF, akPu4PF). The turn-on is not infinitely sharp since the offline jet reconstruction used here includes more sophisticated tower cleaning and selection algorithms than the online one. Out of 137 akPu3PF jets with $p_T > 100$ GeV/c and $|\eta| < 2$ in the analyzed minimum bias sample, there is one event which did not pass jet trigger HLT_HIJet80 (0.7%). This possible inefficiency is included as a systematic uncertainty.

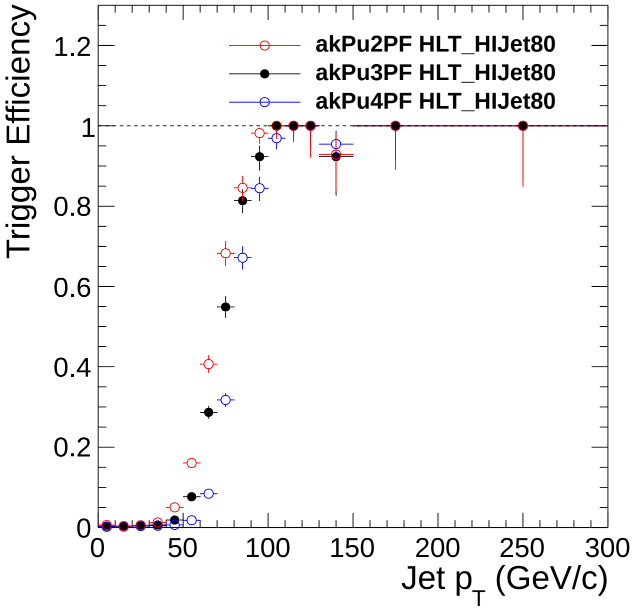

Figure 3.1: Efficiency curves for the HLT_HIJet80, as a function of the leading jet transverse momentum with $|\eta| < 2$ evaluated from minimum bias sample.

The selection of events in this thesis was based on the these HLT triggers as applied to the jet events. It was checked that the events selected by the jet trigger bits also satisfy all triggers and selections imposed for minimum bias events.

3.2 Offline Event Selection

The event selection used in CMS for PbPb collisions in 2011 is documented in other jet analysis papers [25, 29] and described in this section. The cleaning cuts that remove background, beam gas, Previously Known As "Monster" (PKAM) noise events generated from the electronics, and ultraperipheral collisions, have only a small effect on the number of selected events. The same settings are used in this thesis, except for the addition of requiring a primary vertex in the z direction to be within ± 15 cm, which resolves differences in vertex range simulated in Monte Carlo in comparison to data.

- BSC halo filter: events where any of the BSC halo bits fired (L1 Technical Trigger bits 36, 37, 38 or 39) were excluded from the analysis. This happened only in 0.1% of the events triggered by the HLT jet trigger with 80 GeV/c threshold, thus any possible biases are negligible.

- Requirement of a reconstructed 2-track primary vertex was imposed. In peripheral events, all tracks above 75 MeV/c transverse momentum were used to reconstruct the vertex. In central events, the minimum p_T requirement was increased, and the tracking region was narrowed down, to keep the maximum number of fitted tracks stable around at 40–60, ensuring time-efficient reconstruction. This requirement removes non-inelastic-collision events (e.g. beam-gas, UPC) with large HF energy deposits but very few pixel hits.

- A cut to remove PKAM events, which is a requirement of pixel cluster-length compatibility with the vertex.

- A requirement of an off-line HF coincidence, which requires at least 3 towers on each side of the interaction point in the HF with at least 3 GeV total deposited energy per tower.

3.2.1 Removal of HCAL Anaomalous Signals

A basic offline collision event selection removes the majority of events caused by anomalous signals (or noise) in the HCAL. Filters for noise in the HB and HE subdetectors were implemented that were tuned for the PbPb data taking environment [25, 29, 30]. Events that were removed using these settings were looked at individually and found to consist of readout box (RBX) and hybrid photo-diode (HPD) noise, which has a characteristic signature.

3.2.2 Leading Track Jet Quality Identification

In previous dijet analyses, any remaining detector noise was studied with pairs of jets that were not back-to-back. However, that option is not possible in this inclusive jet study. The 2011 dijet quenching analysis selected jets that contained at least one track with track $p_T > 4$ GeV/c [25, 30]. With the intent to minimize bias in identification of the jet fragmentation pattern, as well as to optimize the efficiency of this selection, this requirement was modified. Jets were selected by comparing the maximum track p_T within a jet to that of the total jet p_T, keeping those jets with a ratio greater than 0.01. This selection rejects $\approx 1\%$ of jets in Monte Carlo studies. Events that met the full event selection but failed the maximum track p_T over total jet p_T selection and had a reconstructed jet with $p_T > 400$ GeV/c were inspected individually. Of those 11 events, ten showed signal characteristic of HCAL HPD noise.

3.2.3 Luminosity and Dataset

The 2011 PbPb dataset used in the analysis contained runs 181530 - 183013, which is equivalent to 129 μb^{-1}. The PbPb dataset used is /HIHighPt/HIRun2011-hiHighPt-PromptSkim-v1/RECO. Data was reconstructed with CMSSW software versions 4_4_2 and 4_4_2_patch6, as well as Global Tag GR_P_V27A. Figure 3.2 shows the recorded integrated luminosity for the heavy-ion run recorded by CMS (including luminosity sections with detector problems).

The pp data used in this analysis was recorded at 2.76 TeV center-of-mass energy in March 2011, covering runs 161366-161473, with an equivalent luminosity of 212 nb^{-1}. Studies on the pp data were analyzed with software version 4_4_2_patch5 and reconstructed with Global Tag GR_P_V27A. The pp dataset used is /AllPhysics2760/Nov2011_HI-SD_JetHI-276TeV_ppRereco/RECO.

A summary of the offline event selection and the numbers of events remaining is given in Table 3.1 for PbPb data, and Table 3.2 for pp data. The fraction of events remaining is always with respect to the previous cut (one above it in the table). The selection was analyzed in a data file from a skim of the RECO dataset. In the PbPb sample, collision event selection and an η cut of the leading jet was

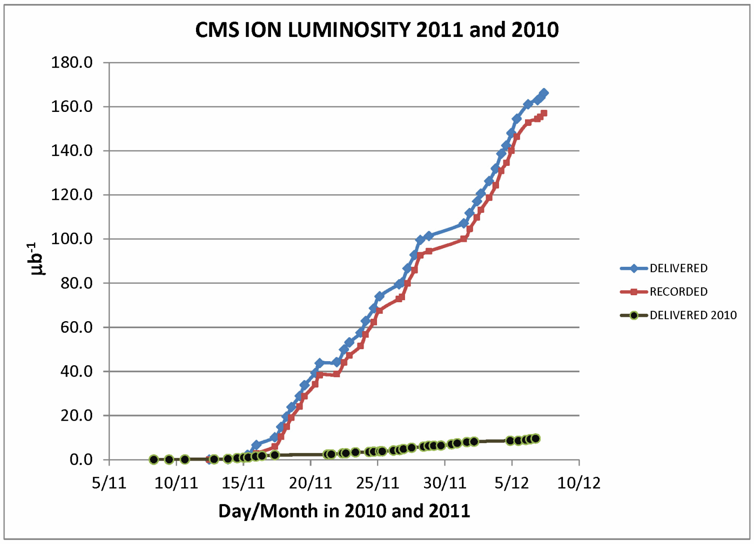

Figure 3.2: Recorded integrated luminosity for the heavy-ion runs.

applied at skim level.

3.2.4 Centrality Determination

For analysis of PbPb events, it is important to determine the overlap or impact parameter of the two colliding nuclei, discussed in Sec. 1.3.1, as this is an essential variable in this analysis [31].

In heavy-ion collisions, thousands of particles are produced, generating a much more complicated system compared with proton-proton collisions. As nuclei are themselves made up of nucleons (protons and neutrons), it is intuitive to study the number of nucleons involved in a sample of selected collisions in order to make a reasonable comparison with the single nucleon collision (proton-proton collision).

Table 3.1: The Effects of Various Cuts on the PbPb Triggered Data Sample. % values are always with respect to the line above (the cuts are applied in sequence).

Cut	events remaining	% of events remaining
Without Selection	496680	100.00
Collision event selection	496680	100.00
HCAL cleaning	494280	99.52
$0-90\%$ Centrality	494173	99.98
$\lvert\eta\rvert < 2$	494173	100.00
$p_T > 100$ GeV/c	131474	26.60
$\lvert$Primary Vertex z$\rvert < 15$ cm	127718	97.14
Maximum track p_T / Jet p_T	127175	99.57

Table 3.2: The Effects of Various Cuts on the pp Triggered Data Sample. % values are always with respect to the line above (the cuts are applied in sequence).

Cut	events remaining	% of events remaining
Without Selection	23031	100.00
Collision event selection	23023	99.97
HCAL cleaning	22732	98.74
$\lvert\eta\rvert < 2$	22695	99.84
$p_T > 100$ GeV/c	9096	40.08
$\lvert$Primary Vertex z$\rvert < 15cm$	8935	98.23
Maximum track p_T / Jet p_T	8791	98.39

Since the number of nucleons involved in one heavy-ion collision is closely related to the geometry of the collision, it is essential to characterize the degree of overlap of the interacting nuclei such as their shape.

Figure 3.3 left panel depicts the geometry of two Lorentz-contracted heavy -ion nuclei appoaching each other before collision. The impact parameter b is the distance between the center of the overlapping nuclei. The larger the overlapping area of the collision, the larger b is. Those nucleons that do not participate in the collision, or more precisely, are out of the overlapping area, will be defined as spectator nucleons. In the later phase of the collision, they hit the subdetectors (i.e. Zero-Degree Calorimeter) installed at large pseudorapidities (see Sec. 2.2).

Though the femtoscopic length scales of the system rules out the possibility of direct observation of the impact parameter (b) or number of participating nucleons (N_{part}) or binary nucleon-nucleon collisions (N_{coll}) (Fig. 3.3), model techniques have been developed to allow prediction and estimation of these quantities from experimental data. These techniques, which consider the multiple-scattering of nucleons in nuclear targets, are generally referred to as Glauber Models [32], which were proposed and studied by Roy Glauber. This model serves as a standard method to determine the overlapping collision geometry, or the terminology we use more commonly in the experiments, the collision centrality.

Since a direct measurement of b is not obtainable in laboratories, a new parameter“centrality” is introduced to characterize b. The centrality of an event is the percentage of collisions having a larger particle multiplicity than the current collision. In this sense, it is measured from the number of generated particles in

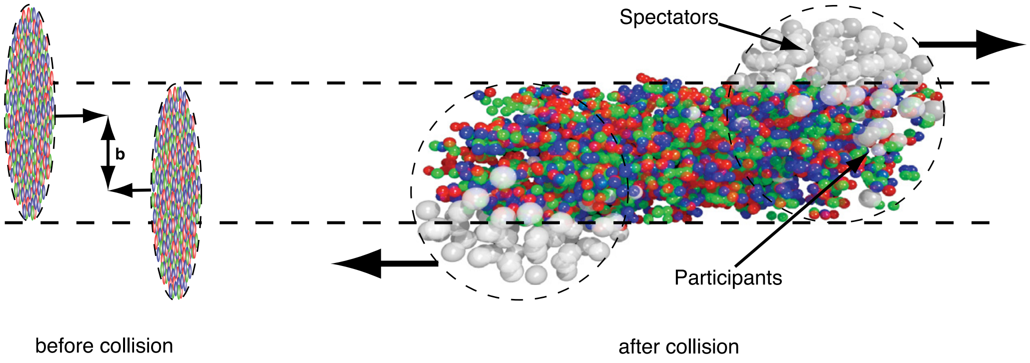

Figure 3.3: Heavy-ion collision geometry before and after the collision. The nucleons within the impact parameter b participate in the collisions and the ones outside the range are considered spectator ions, which are not involved in the collisions. Adapted from [33].

an event, where the more produced particles, the more collision participants and therefore the smaller the b and the centrality. The event with smallest centrality is the most central collision and the one with biggest centrality is the most peripheral collision. For example, an event with the centrality of 5% indicates 5% of events have a higher multiplicity than the current event. An uncertainty for determining the overlapping of an event occurs due to the dynamic properties of nuclei.

The centrality determination utilized the total sum of the transverse energy of calorimeter towers in the HF region (covering $2.9 < |\eta| < 5.2$). The distribution of this total transverse energy was used to divide the event sample into bins, each representing 2.5% of the total nucleus-nucleus interaction cross section. For the jet analysis, these fine-grained bins were combined into 6 larger bins corresponding to the most central 5% of the events (i.e. smallest impact parameter), the next most central 5% of the events (denoted 5%–10%), as well as bins of 10%–30%, 30%–50%, and 50%-70%, with the remaining peripheral bin of 70%–90%. The distribution of the HF signals used in the analysis, along with the cuts used to define the six event classes is shown in the left panel of Fig. 3.4. This shape is characteristic of all observables related to bulk particle production in heavy-ion collisions. The peripheral events produce very few particles while the central events, in which many more nucleon-nucleon interactions occur, produce a much larger number. Also shown in the left panel of Fig. 3.4 is the distribution of the total HF energy in the jet-triggered sample (HLT_HIJet80) used in this thesis. The events above 0% centrality in the jet triggered histogram are pile-up events.

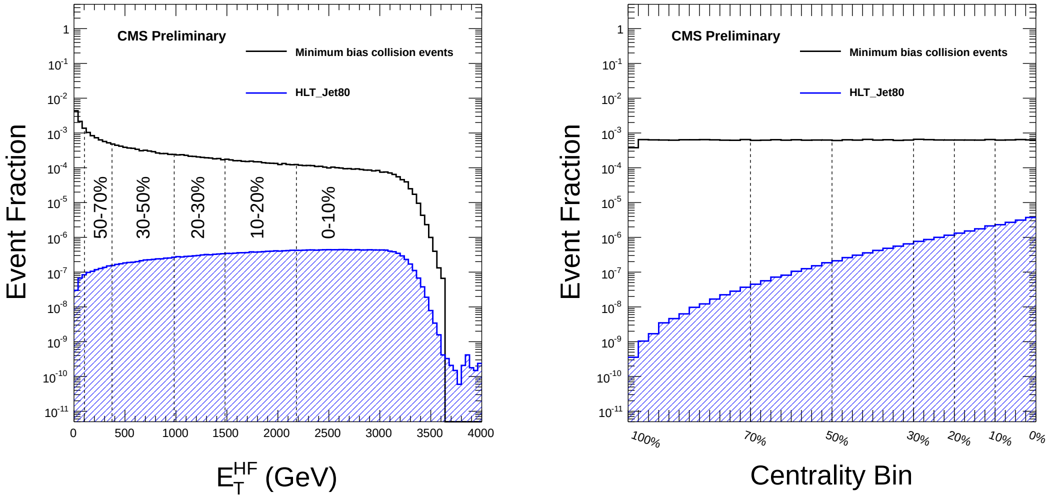

Figure 3.4: Left: Sum of HF E_T for minimum bias collisions (black) compared to those in jet triggered events (blue) in PbPb. Centrality bin division is shown with the dotted lines. The blue tail in the high energy deposit region corresponds to pile-up events. Right: Centrality bin event fraction for minimum bias collisions (black) - flat by definition, compared to jet triggered events (blue histogram).

The right panel of Fig. 3.4 shows the fraction of the events falling in each of the 40 centrality bins. Fractions of the total number of minimum bias events in the sample are shown for both minimum bias (black open histogram) and HLT jet triggered (blue cross-hatched histogram) events. Following the standard convention, the percentage cross section labels run from 100% for the most peripheral to 0% for the most central events. By construction, the fraction of events falling in each bin for minimum bias events is a constant 2.5% percent over the entire range, with the exception of the small inefficiency in a few of the most peripheral bins. From these two distributions, it can be seen that the HLT jets of roughly 80 GeV/c required to pass the on-line trigger are more common in central events, as expected due to the larger number of nucleon-nucleon collisions. The evolution of the fraction of minimum bias events that satisfy the online jet trigger is clear and it was found that jets of this magnitude occur, on average, in roughly 2–4% of the events in the most central bin. This imbalance of number of jet triggered events as a function of centrality is taken into account when using Monte Carlo(MC) samples.

Chapter 4

Jet Reconstruction

In this chapter, the jet reconstruction algorithm used in this analysis is summarized in Sec. 4.2. Monte Carlo simulation events, found in Sec. 4.1, are used to derive the jet response, study the resolution effects (Sec. 4.5), and monitor the performance of jet reconstruction (Sec. 4.4). The technique used for jet reconstruction is the same as in other CMS PbPb analyses [31, 34, 35] with jet resolution parameter R=0.3. As a cross-check, different resolution parameters (R=0.2, R=0.4) are also analyzed with the particle flow jets. One of the outstanding challenges in jet reconstruction, underlying event subtraction, will be evaluated in Sec. 4.3.

4.1 Monte Carlo (MC) Simulation

Monte Carlo (MC) simulations were made with Global Tag STARTHI44_V7, and CMSSW software version 4_4_2_patch6. QCD dijet events were simulated with PYTHIA [36], Z2 tune. These events were simulated in sets of different minimum $\hat{p_T}$ = 30, 50, 80, 120, 170, 200, 250, and 300 GeV/c. To simulate the copious soft heavy-ion background in a PbPb collision, these PYTHIA events (simulated pp events) were mixed into HYDJET (simulated heavy ion background) [37] (version 1.8, tune Drum). Analysis of the background that required a minimum bias sample used HYDJET alone. In order to produce the MC reference of inclusive jets, high p_T

jet production events were produced by the PYTHIA Monte Carlo event generator, which was modified to take into account the isospin of the colliding nuclei [37]. These events are propagated through the CMS detector using the GEANT4 package [38] to simulate the detector response. These samples are embedded in simulated minimum-bias events from the HYDJET [37] generator in order to study the effect of the PbPb underlying event on the jet reconstruction. Although it would be more advantageous to embed the PYTHIA signal into real minimum-bias data instead of simulations, this is technically not possible due to the difference between data and simulation in the way geometry is implemented in CMS. Such implementation does not provide the possibility of performing tracking simultaneously on the simulated signal and background data event, which is an important ingredient of the jet reconstruction in this analysis. The statistics of simulated MC samples and their cross sections calculated from PYTHIA generator are summarized in Table 4.1.

Table 4.1: PYTHIA Events Simulated and Embedded in HYDJET Samples

sample	$\hat{p}_{\mathrm{T}}$	Number of events	cross section (mb)
Di-Jet + PbPb data	30 GeV/c	100k	1.08×10^{-2}
	50 GeV/c	130k	1.02×10^{-3}
	80 GeV/c	130k	9.91×10^{-5}
	100 GeV/c	60k	3.07×10^{-5}
	120 GeV/c	60k	1.13×10^{-5}
	170 GeV/c	65k	1.47×10^{-6}
	200 GeV/c	55k	5.31×10^{-7}
	250 GeV/c	40k	1.19×10^{-7}
	300 GeV/c	50k	3.18×10^{-8}

4.2 Jet Reconstruction Algorithms

Jet reconstruction algorithms are divided into two categories: cone algorithm and successive recombination algorithm (to which the anti-k_{T} algorithm in this analysis belongs). The latter one is based on defining a distance d_{ij} between any pair of objects in an event, as well as a so-called beam distance d_{iB} for each object. For each event, the smallest distance is identified. If it is smaller than the beam distance, the two objects are combined into one. If it is larger, then the object is identified as a jet and removed from the event. This iterates until there is no remaining objects. The successive recombination algorithms are defined by the distance measures [39]:

$$\mathbf{d}_{ij} = \mathbf{min}(\mathbf{k}_{T,i}^{\mathbf{2p}}, \mathbf{k}_{T,j}^{\mathbf{2p}})(\Delta \mathbf{y}_{ij}^{2} + \Delta \phi_{ij}^{2}), \tag{4.1}$$

$$\mathbf{d}_{iB} = \mathbf{R}^{2}\mathbf{k}_{T,i}^{\mathbf{2p}}. \tag{4.2}$$

The interger p defines the algorithm, and the anti-k_{T} algorithm has p=1.

Jet reconstruction in heavy-ion collisions in CMS is performed with the anti-k_{T} jet algorithm that is encoded in the FastJet framework [40]. Although the default algorithm for pp collisions is anti-k_{T} with a resolution parameter of $R = 0.5$, a smaller resolution parameter of R=0.3 is used to minimize the effects of heavy-ion background fluctuations in this analysis. In this process, the contribution from each calorimeter tower is assigned a momentum, the absolute value and the direction of which are given by the energy measured in the tower, and the coordinates of the tower. The raw jet energy is obtained from the sum of the tower energies, and the raw jet momentum by the vectorial sum of the tower momenta, which results in a nonzero jet mass. The raw jet energies are then corrected to establish a relative uniform response of the calorimeter in η and a calibrated absolute response in transverse momentum p_T. While it is possible to subtract the heavy-ion background with the $FastJet$ framework using a definition of an active 4-vector area (A_{jet}), for this analysis an algorithm that is a variant of an iterative "noise/pedestal subtraction" technique is used to estimate the heavy-ion background event-by-event [41, 42], with details described in Section 4.3. The anti-k_{T} jet algorithm runs over the particle flow (PF) objects that are reconstructed by matching tracks from the Tracker to the ECAL and HCAL [43, 44]. The particle-flow event reconstruction consists in reconstructing and identifying each single particle with an optimized combination of all subdetector information. In comparison to previous PbPb jet analyses [25, 29, 31, 34], the reconstructed tracks used here are created with three iterations. The tracks are seeded by pixel triplets (as in the previous analyses), looser pixel triplets, and pixel doublets. The tracks are used as part of the particle flow objects, and their performance in this analysis is evaluated as part of the overall jet reconstruction performance.

The anti-k_{T} algorithm with a resolution parameter of R = 0.3 and the background subtraction described in Sec. 3.2 is used for the following study (akPu3PF). As the PbPb particle flow algorithm uses heavy-ion tracking that has different efficiency than pp tracking, η and p_T dependent energy correction factors (L2L3) for the jets are derived from the analysis of the PYTHIA sample at 2.76 TeV, similar to those used in pp [45, 46]. In analyses of pp data or PYTHIA, i.e. without heavy-ion background, the same heavy-ion tracking is utilized and thus the same L2L3 corrections are used. The jet p_T shown in this thesis has the energy correction applied unless otherwise marked.

Additional cross-checks are performed by using an iterative cone algorithm with a cone radius of R = 0.5, and calorimetric inputs. This iterative cone calorimeter algorithm is also used at the trigger level in PbPb collisions, and is referred to as icPu5Calo jets. The analysis is also checked with the anti-k_T algorithm applied at different resolution parameters: 0.2 (akPu2PF) and 0.4 (akPu4PF). A cross-check may also be performed with the equivalent anti-k_T algorithms utilizing only calorimetric inputs for jet reconstruction.

4.3 Underlying Event Subtraction

One of the major challenges in the jet reconstruction is to understand the uncorrelated background within the selected jet cone due to the large multiplicity in the heavy-ion collisions. This uncorrelated background may worsen the jet energy resolution in the data. This background is studied as a function of centrality and in two different regions of η that roughly correspond to the Barrel and Endcap regions in CMS experiment.

The algorithm to estimate and subtract the background energy for each jet event-by-event is a variant of an iterative "noise/pedestal subtraction" technique

[42] that is designed for discrete quantification of the energy in η and ϕ, which is perfect for a calorimetric measurement. To use the same subtraction code to candidates reconstructed with particle flow, which have a continuous distribution in momentum space, a calorimeter tower geometry is imposed on the particle flow objects. This is performed by summing up the p_T of the particle flow candidates that point to a fixed $\eta \times \phi$ bin that corresponds to the HCAL cell granularity, although evaluated with respect to the momentum values of candidates at the vertex, not the calorimeter surface. After this projection, the mean value and dispersion of the energies recorded in the particle flow objects are calculated for all rings of cells at constant pseudorapidity η.

The value of this pedestal function, $\mathrm{P}(\eta)$, containing the information on the mean and dispersion, is then subtracted from all cells. If a cell energy comes out negative, it is set to zero. The algorithm subtracts $\langle E_{\mathrm{cell}} \rangle + \sigma(E_{\mathrm{cell}})$ from each cell in order to compensate for the bias caused by this elimination of negative energy. Jets are then reconstructed, using the standard anti-k_{T} algorithm, from the remaining non-zero particle flow objects. In a second iteration, the pedestal function is recalculated using only particle flow objects outside the area covered by reconstructed high p_T jets ($p_T > 15$ GeV/c). The threshold of 15 GeV/c was chosen to optimize the final extracted jet energy resolution. The cell energies are updated with the new pedestal function (again subtracting mean plus dispersion) and the jets are reconstructed once more using the updated particle flow objects. The performance of this algorithm is documented in Ref. [42]. For jets of different cone sizes, a different threshold is used: 10 GeV/c for akPu2PF and 20 GeV/c for akPu4PF.

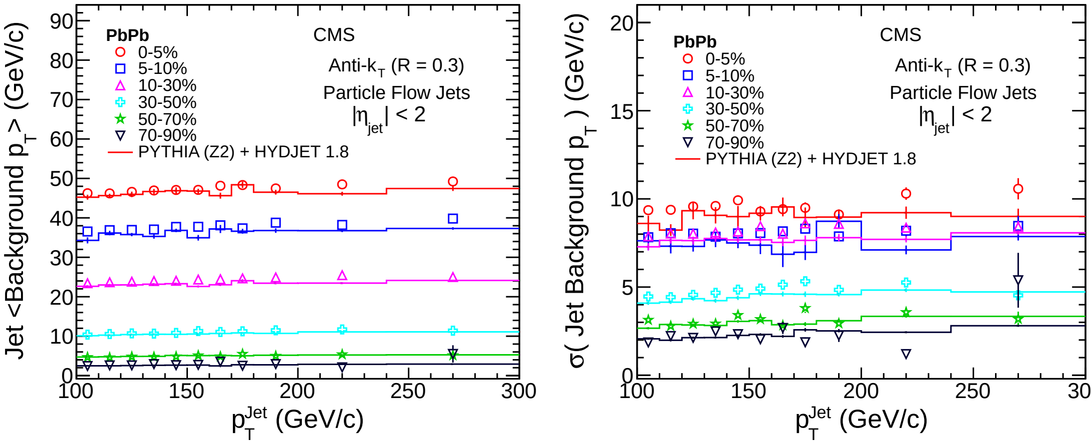

Figure 4.1: Underlying event background jet p_T mean and RMS for data and MC for various centrality bins within $|\eta|$<2 for PbPb collisions.

The sum background $\langle p_T \rangle$ for reconstructed jets within $|\eta| < 2$ as a function of collision centrality for anti-k_T PF jet algorithm with a resolution parameter of $R = 0.3$ in PbPb collision data is shown in Fig. 4.1. The average background (in terms of $\langle p_T \rangle$ and RMS) is fairly consistent with simulations over the wide range of reconstructed jet p_T.

As the individual points in Fig. 4.1 come from fits to the results, it is also important to look at the individual bin distributions. For the lowest jet p_T bin, the individual bin distributions are shown in Fig. 4.2.

4.4 Jet Finding Efficiency

The performance of jet reconstruction algorithms can be studied with simulations of PYTHIA events mixed into a HYDJET PbPb background (PYTHIA+HYDJET). This study is done by comparing reconstructed jets (RecoJets) to generator level jets (GenJets), where the GenJets are selected from the PYTHIA hard process. The

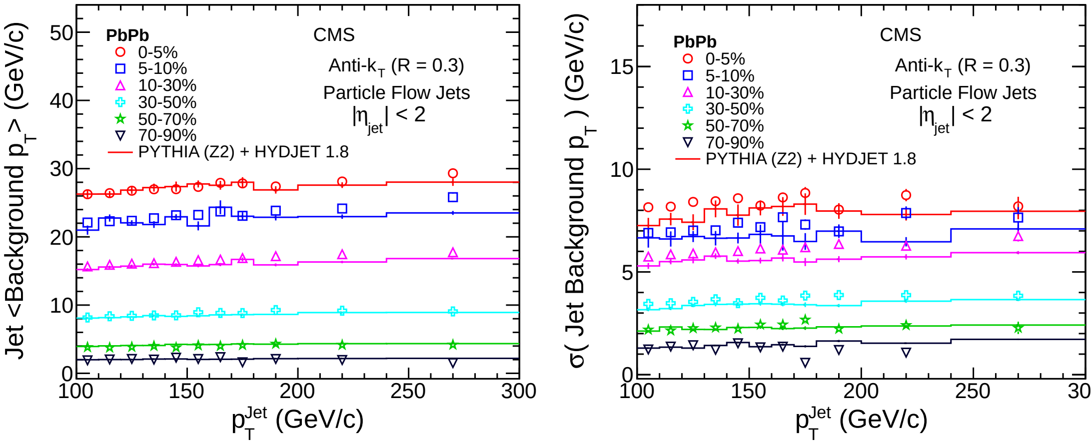

Figure 4.2: Subtracted underlying event background p_T for jets reconstructed with $100 < p_T(\text{ GeV}/c) < 110$ for different PbPb collision centralities. Data is represented by open symbols, MC by the lined histogram, and statistical uncertainty is shown.

RecoJets are matched to GenJets in position with $\Delta R = \sqrt{\Delta\phi^2 + \Delta\eta^2} < 0.3$ in each bin of GenJet p_T. The jet reconstruction efficiency is calculated as the fraction of GenJets that have matched RecoJets, and is shown in Fig. 4.3. The different particle flow cone algorithms are shown by size from left (0.2), middle (0.3), to right (0.4). Within the jet selection for this analysis, a 99% efficiency is achieved.

Figure 4.4 shows the total transverse momentum of the particle flow candidates in three different cone sizes for the given centrality bins. MinBias data is used to avoid the contribution of jets and the data is compared with the energy extracted in the same way with the Hydjet 1.8 (Drum) tune Monte Carlo. The distributions are fitted by Gaussian distributions shown as solid histograms for the MinBias and dashed for the Hydjet data. There appears to be some deviation from Gaussian Fits in the high tail due to expected contribution from hard scattering. The parameters are extracted from the Gaussian fits on both simulations and MinBias data. The

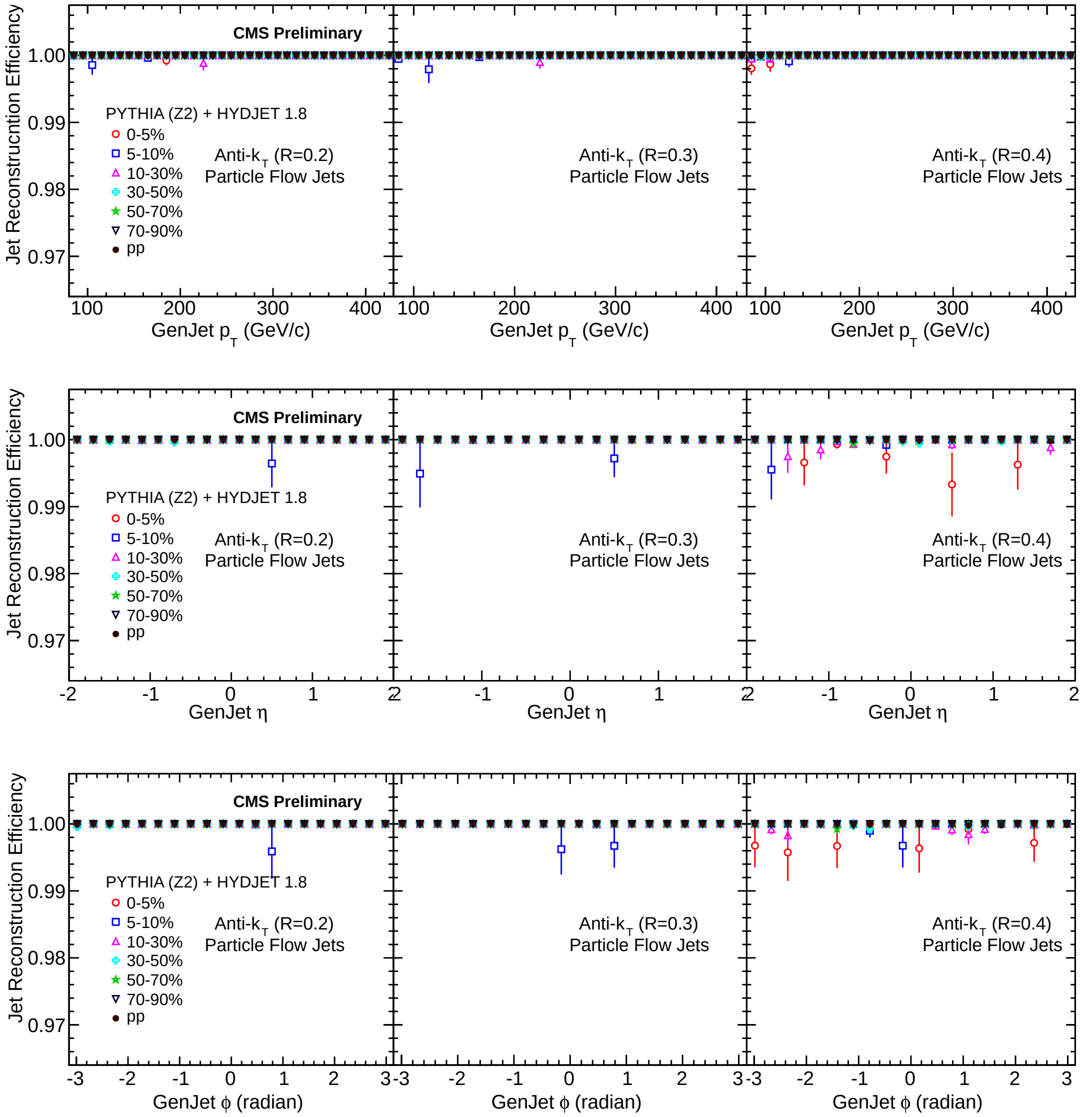

Figure 4.3: Jet reconstruction efficiency for different jet algorithms as a function of p_T (top), η (middle) and ϕ (bottom).

σ values are presented in Table 4.2 for MinBias data and Table 4.3 for the Hydjet data. The histogram of differences of the standard deviation of the Gaussian fits is shown in Fig. 4.4. This difference is used in extracting the systematic uncertainties for the smearing.

Table 4.2: σ Values from Gaussian Fits to Random Cone Distributions of the Minbias PbPb data for the given centrality bins and cone sizes.

% Centrality	R=0.2	R=0.3	R=0.4
0-5%	6.66 ± 0.05	10.88 ± 0.05	17.13 ± 0.10
5-10%	5.78 ± 0.04	9.06 ± 0.05	14.14 ± 0.07
10-30%	4.25 ± 0.02	8.66 ± 0.03	13.21 ± 0.05
30-50%	2.05 ± 0.06	3.85 ± 0.02	6.56 ± 0.03
50-70%	0.30 ± 0.18	1.98 ± 0.01	2.07 ± 0.01
70-90%	1.94 ± 0.10	1.91 ± 0.05	1.85 ± 0.03

Table 4.3: σ Values from Gaussian Fits to Random Cone Distributions of MC Simulations for the given centrality bins and cone sizes.

% Centrality	R=0.2	R=0.3	R=0.4
0-5%	6.42 ± 0.04	10.53 ± 0.05	16.67 ± 0.10
5-10%	5.51 ± 0.04	8.80 ± 0.04	13.43 ± 0.06
10-30%	3.96 ± 0.01	8.15 ± 0.03	12.61 ± 0.04
30-50%	1.99 ± 0.01	1.73 ± 0.01	5.98 ± 0.03
50-70%	0.25 ± 0.11	1.96 ± 0.01	2.09 ± 0.01
70-90%	0.17 ± 0.22	0.26 ± 0.23	0.37 ± 0.27

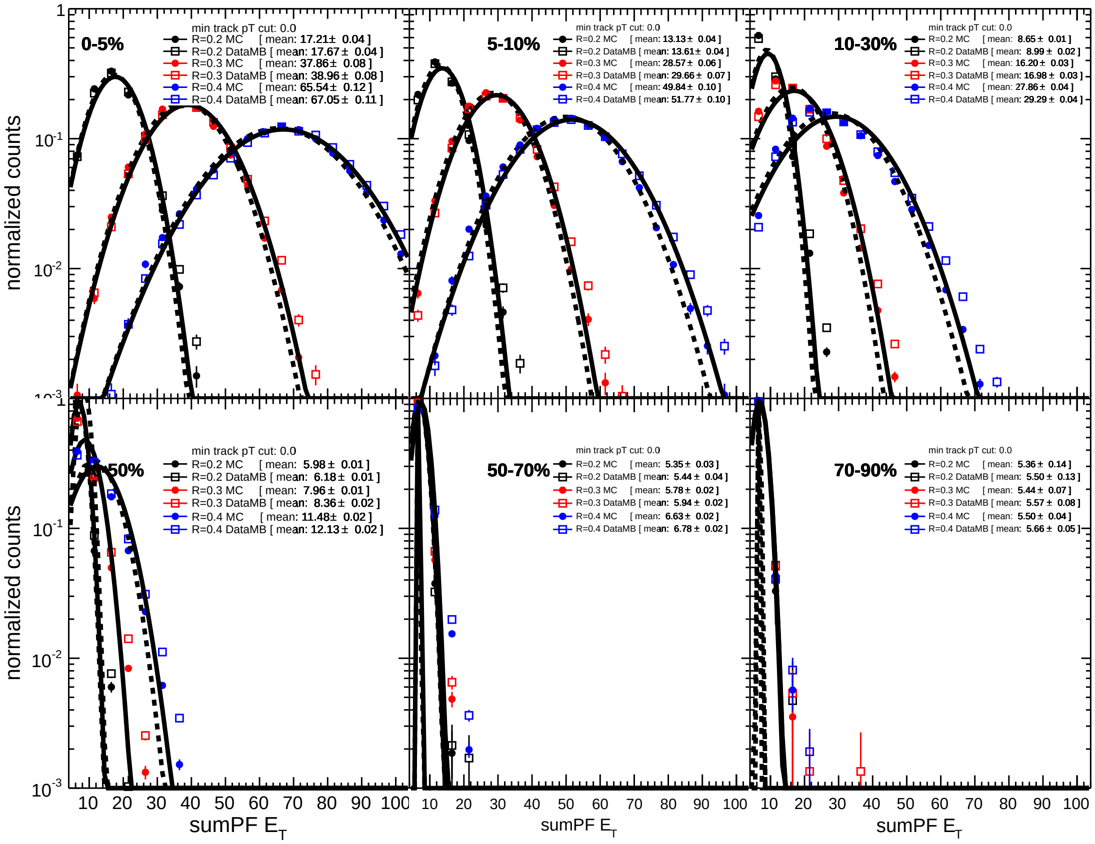

Figure 4.4: Total transverse momentum of the particle flow candidates in a cone (R=0.2, 0.3 and 0.4) around a randomly determined axis, for the given centrality bins. The MinBias data is compared with the Hydjet 1.8 (Drum) tune. The distributions are fitted by Gaussian distributions shown as solid histograms for the MinBias and dashed for the Hydjet data.

4.5 Jet Resolution and Response

The matched RecoJets and GenJets are then used to derive the jet response and resolution. In each bin of GenJet p_T, the ratio of RecoJet and GenJet is plotted. This has the shape of a Gaussian distribution. Individual bins are plotted later in the discussion in Sec. 5.3. The means of these distributions are found as the jet response, shown in the lower plots in Fig. 4.5. Response from pp simulations are shown as closed circles, and from PbPb as open circles. The PYTHIA results are close to 1, as expected. The response for PbPb deviates from 1, and is included in the systematic uncertainty.

The upper parts of Fig. 4.5 show the jet p_T resolution, which is found from the width of the RecoJet/GenJet distributions. In peripheral collisions, the PbPb resolution is similar to that of pp. However, in central collisions, the jet p_T resolution of PbPb simulations is worse at lower GenJet p_T, and closer to pp at higher GenJet p_T. As the effective jet radius increases (0.2 to 0.4) and the jet finder (even with pileup subtraction) has the opportunity to pick up more background, the jet p_T resolution worsens for lower GenJet p_T values. Figure 4.6 shows the comparison of the uncorrected and corrected jet energy scale for pp and different centralities in PbPb collision in MC. The jet energy correction factors are from 15-20% across the p_T range in each centrality class.

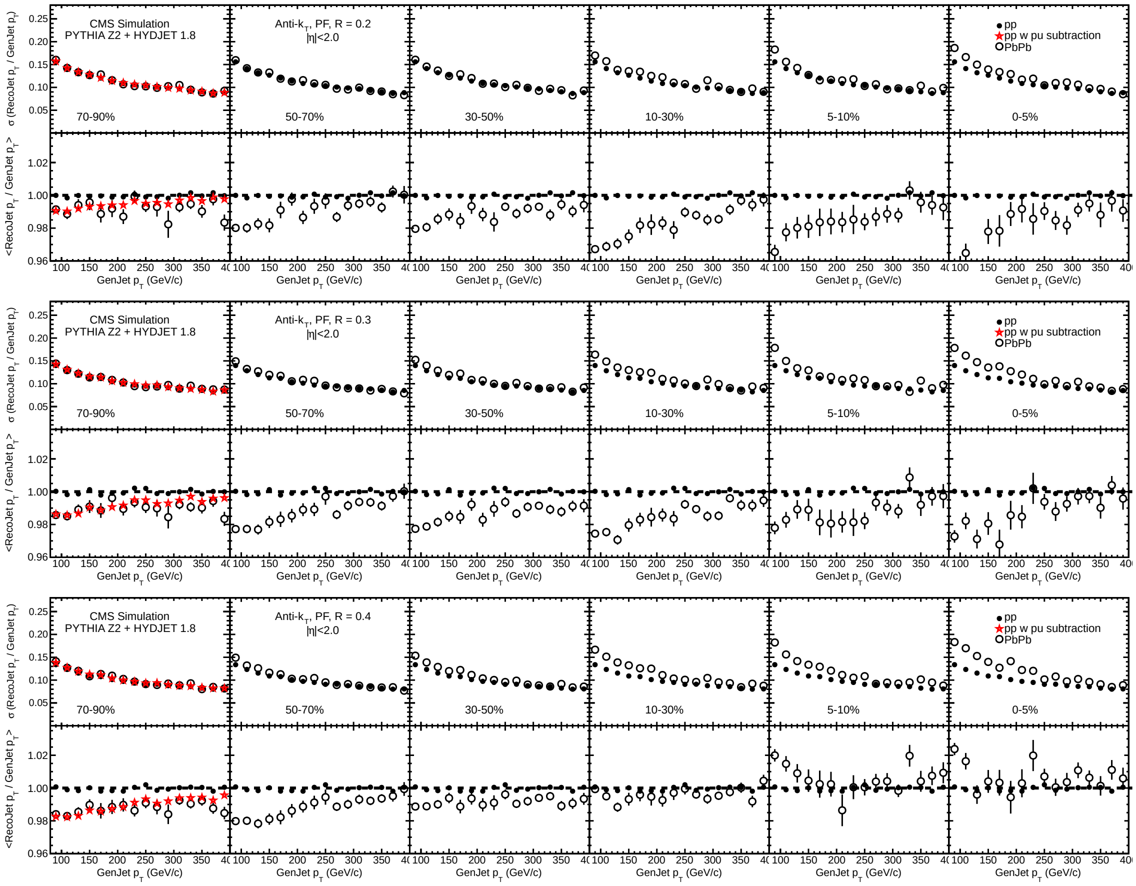

Figure 4.5: Jet p_T response and p_T resolution for anti-k_T jet algorithm with R=0.2 (top), 0.3 (middle) and 0.4 (bottom) for pp (PYTHIA Z2) and different centralities in PbPb (PYTHIA Z2 + HYDJET 1.8). Different centralities are shown from left (peripheral) to right (central) for PbPb, with the pp simulations repeated in all centralities.

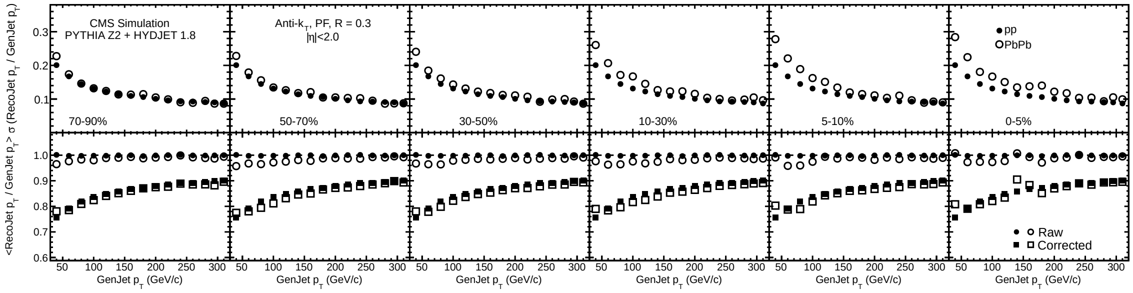

Figure 4.6: Jet p_T response and p_T resolution for anti-k_T jet algorithm with R=0.3 for pp (PYTHIA Z2) and different centralities in PbPb (PYTHIA Z2 + HYDJET 1.8). Different centralities are shown from left (peripheral) to right (central) for PbPb, with the pp simulations repeated in all centralities. Also shown is the jet energy scale of the uncorrected jet p_T(raw) (bottom panel) for the comparison.

Chapter 5

Analysis

With a solid jet reconstruction, the inclusive jet spectra are obtained for PbPb collisions in different centralities and pp collisions (see Sec. 5.1). These measured inclusive jet spectra can be then corrected for the resolution effects with the resolution matrix established from weighted combined MC samples (Sec. 5.2). As a cross check, a smearing method, in addition to the unfolding method used as a main correcting method for this analysis, will be discussed in Sec. 5.3

5.1 Measured Jet Spectra and Measured Jet R_{AA}

The measured inclusive jet spectra are constructed with the event selection described in Chapter 3 using jets within $|\eta| < 2$ and jet $p_T > 100$ GeV/c. The other offline selections include the primary vertex cut of 15 cm and the requirement of each jet passing the maximum track p_T / reconstructed jet $p_T > 0.01$. The jet quality checks are found in Appendix E. Figures 5.1 to 5.3 show the measured akPuPF jet spectra in different bins of collision centrality for PbPb data, as well as the pp data as reference. A multiplication factor was applied to the jet spectra to present the spectra without overlap. The normalization in the PbPb inclusive jet spectra is performed by dividing the number of jets by the number of events in each specific centrality interval and for the pp sample by dividing the number of jets by the number of events in the sample. The measured jet spectra for other jet resolution parameters (effective radii) are shown for R=0.2 in Fig. 5.1, for R=0.3 in Fig. 5.2, and for R=0.4 in Fig. 5.3. These measured jet spectra have not been corrected for any detector or jet resolution effects. The measured jet R_{AA} is shown from Fig. 5.4 to Fig. 5.6 in different cone sizes. The input jet spectra for both pp and PbPb are normalized by the minimum bias number of events due to their nature of being triggered samples. The PbPb inclusive jet spectra are scaled by the average number of binary collisions ($< N_{\mathrm{coll}} >$) as derived from a Glauber model in order to make a valid comparison with pp inclusive jet spectra.

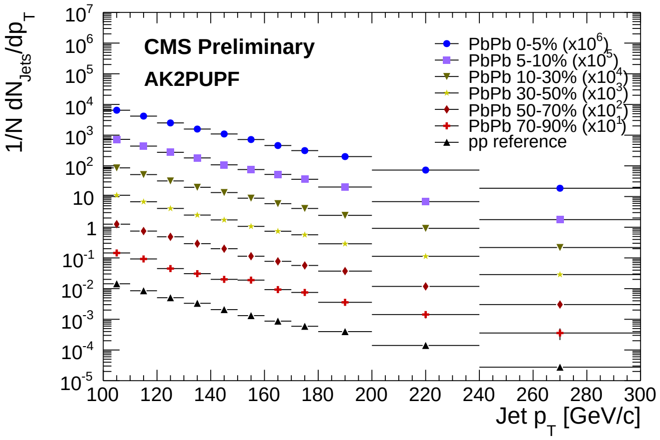

Figure 5.1: Measured inclusive jet spectra for PbPb with R=0.2 for jets in different centrality bins and pp reference data. All the jet spectra are normalized by the number of events in its corresponding centrality intervals. Additionally, PbPb jet spectra are scaled by $< N_{\mathrm{coll}} >$.

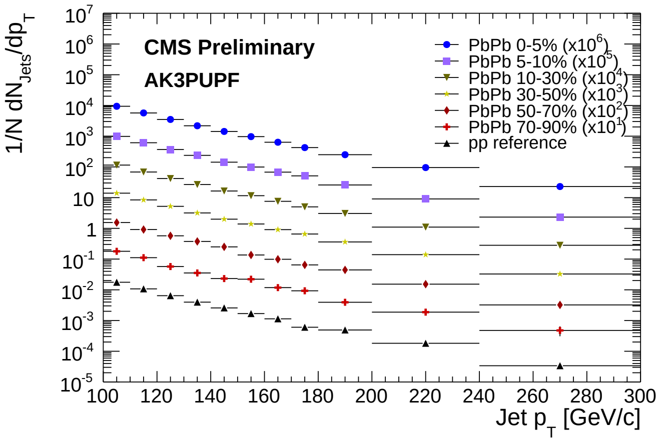

Figure 5.2: Measured inclusive jet spectra for PbPb with R=0.3 for jets in different centrality bins and pp reference data. All the jet spectra are normalized by the number of events in its corresponding centrality intervals. Additionally, PbPb jet spectra are scaled by $< N_{\text{coll}} >$.

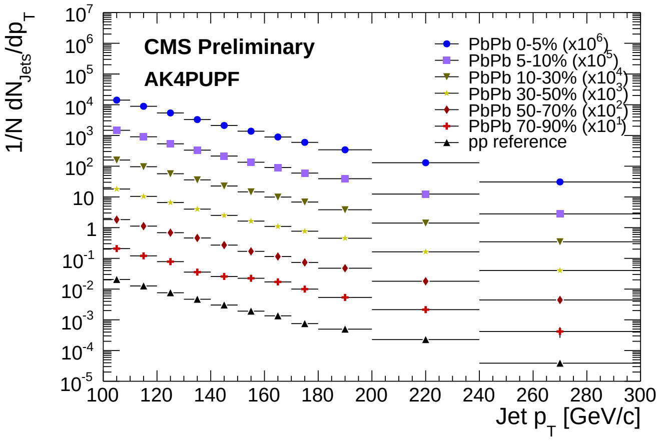

Figure 5.3: Measured inclusive jet spectra for PbPb with R=0.4 for jets in different centrality bins and pp reference data. All the jet spectra are normalized by the number of events in its corresponding centrality intervals. Additionally, PbPb jet spectra are scaled by $< N_{\text{coll}} >$.

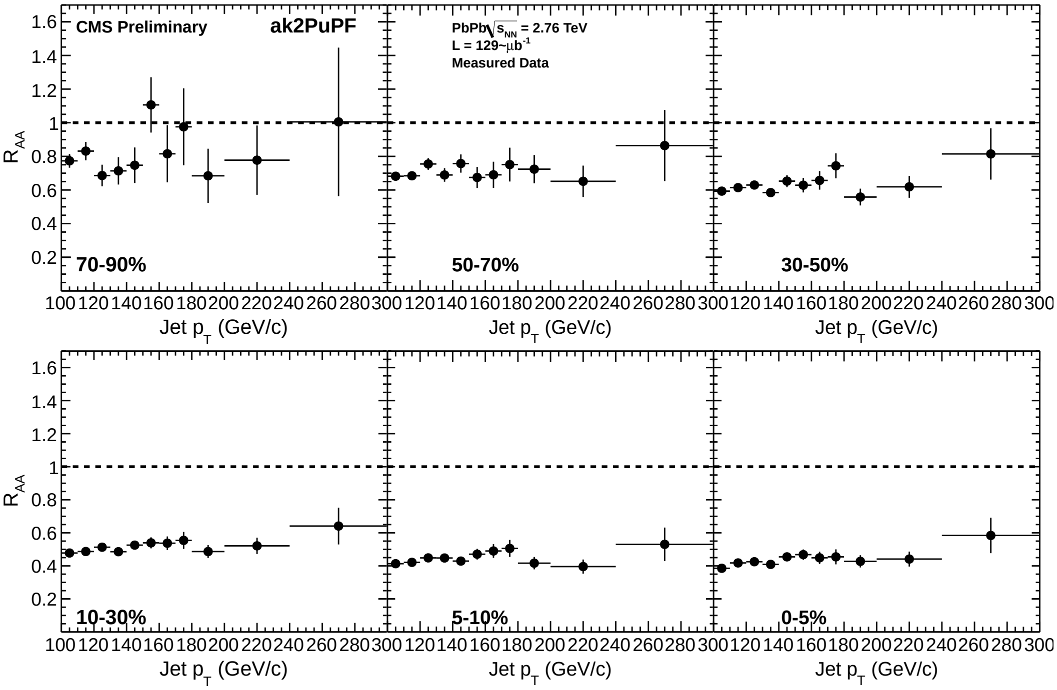

Figure 5.4: Measured R_{AA} constructed with anti-k_{T} particle flow jets in cone size 0.2. The error bars here are only for uncorrelated statisitcal uncertainties.

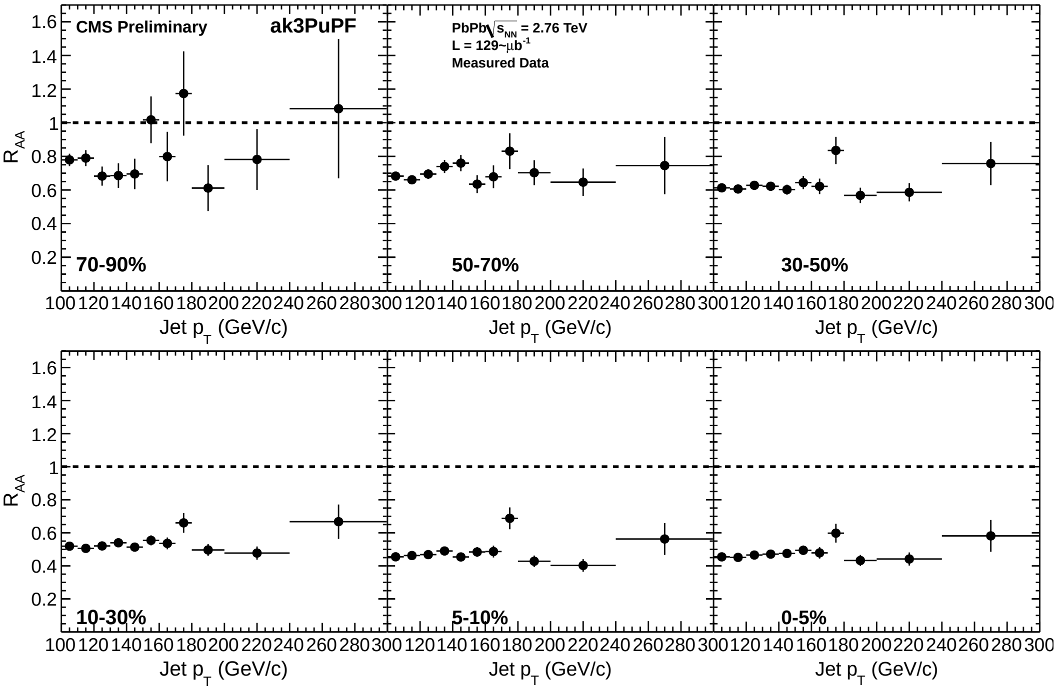

Figure 5.5: Measured R_{AA} constructed with anti-k_{T} particle flow jets in cone size 0.3. The error bars here are only for uncorrelated statisitcal uncertainties.

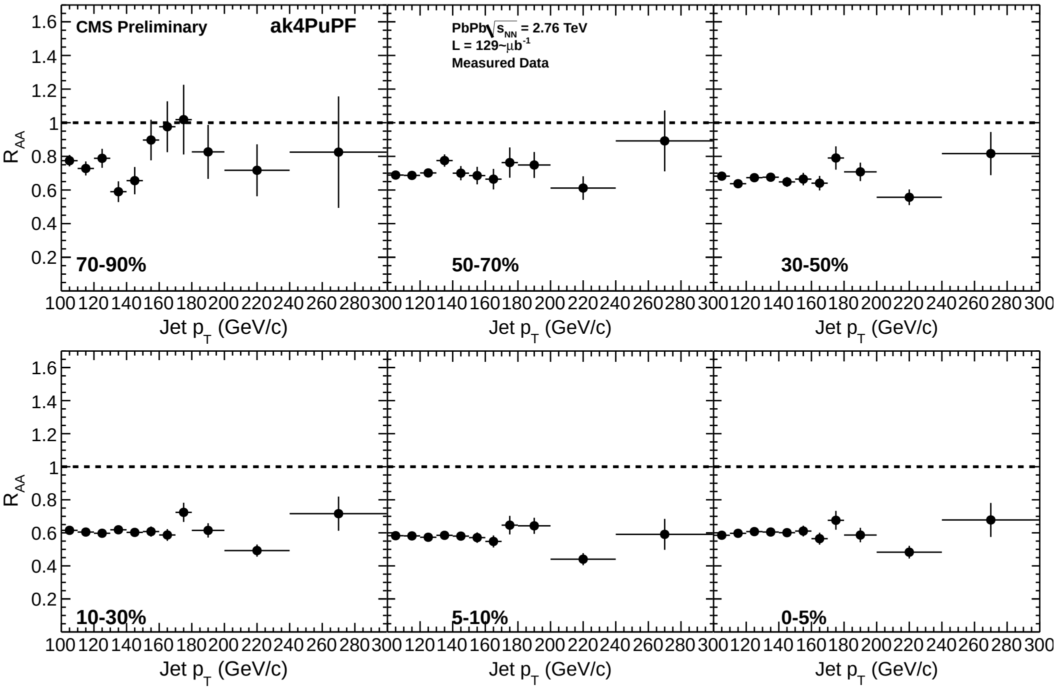

Figure 5.6: Measured R_{AA} constructed with anti-k_{T} particle flow jets in cone size 0.4. The error bars here are only for uncorrelated statisitcal uncertainties.

5.2 Unfolding the Jet Spectra

The measured jet spectra are a convolution of the "real" spectra and the effects of the jet p_T resolution and scale. A typical analysis would also include the effects of jet reconstruction efficiency, which is at 99% (see Chap. 6). The construction of an R_{AA} using both PbPb and pp data taken by the CMS detector has the advantage of canceling baseline detector effects of jet p_T resolution and scale. However, due to the copious soft background of PbPb collisions, the jet p_T resolution is worse in PbPb collisions than in pp collisions. The choice of a small effective cone size in the jet finding algorithm, together with the background subtraction algorithm, minimizes but does not totally eliminate that difference. Additionally, there is a 2% difference in the jet p_T scale between PbPb and pp MC simulations. The jet R_{AA} can be corrected for the effects of jet p_T resolution and scaled with two methods: spectra unfolding and smearing of pp data. The term "unfolding" is used to describe a set of techniques that are used to essentially "invert" the convolution of the spectra and the resolution. This is a non-trivial mathematical challenge because the p_T spectra are very steeply falling and the resolution is derived from MC simulations and therefore is not known exactly. Even if the transformation matrix due to the resolution were known exactly, statistical fluctuations in the measured spectrum can be transformed into unphysically large fluctuations in the unfolded spectra.

With binned histograms for the spectra, the unfolding problem can be understood as the matrix inversion to solve

$$\mathbf{A}\mathbf{x} = \mathbf{b} \tag{5.1}$$

with the correspondence

$$\begin{aligned} \frac{dN}{dp_T^{\mathrm{rec}}} &\leftrightarrow \mathbf{b} \text{ (the measured spectrum)} \\ P(p_T^{\mathrm{rec}}|p_T) &\leftrightarrow \mathbf{A} \text{ (the response matrix)} \\ \frac{dN}{dp_T} &\leftrightarrow \mathbf{x} \text{ (the true spectrum)} \end{aligned} \tag{5.2}$$

The unfolding procedures use a response matrix with MC simulation, and then attempt to reconstruct the true distribution from the measured distribution with this response matrix. (For MC sample details see in Sec. 4.1)

The three methods used to determine the true jet energy spectra include 1) linear least square (LLS) with Phillips–Tikhonov regularization [47–50] or "GSVD" unfolding [51], 2) the Richardson–Lucy [52–54] or "Bayesian" unfolding, and a 3) Bin-by-Bin unfolding technique. Note that technical details of the various unfolding techniques are given in the Appendix D.

Figures 5.7-5.9 show the response matrix from MC that is used in the analysis. The response matrix shows the distribution of reconstructed jet p_T in comparison to generator level jet p_T, finely binned (Fig. 5.7 and Fig. 5.9 (left)) in the actual bins used in the unfolding analysis for PbPb and pp. The response matrix is only shown for jet p_T used in the analysis, but in unfolding, the full range of MC jet p_T

is used, down to 15 GeV/c, which allows for jets to migrate to higher or lower bins. To understand the level of correction, the response matrix is shown in coarser bins of the final jet R_{AA} (Fig. 5.8 and Fig. 5.9 (right)). The matrices were normalized so that the integral of the bins within the same generator level jets bins is 1. All the MC samples used to construct the matrix were centrality, primary vertex and cross section re-weighted. Figures 5.8 and 5.9 right panel are the rebinned matrix with bins consistent to our final result. The range of the bins are indicated on each axis. The numbers inside each bin indicate the probablility of generator level jets in each generator level jet bin migrating to the reconstructed jet bin.

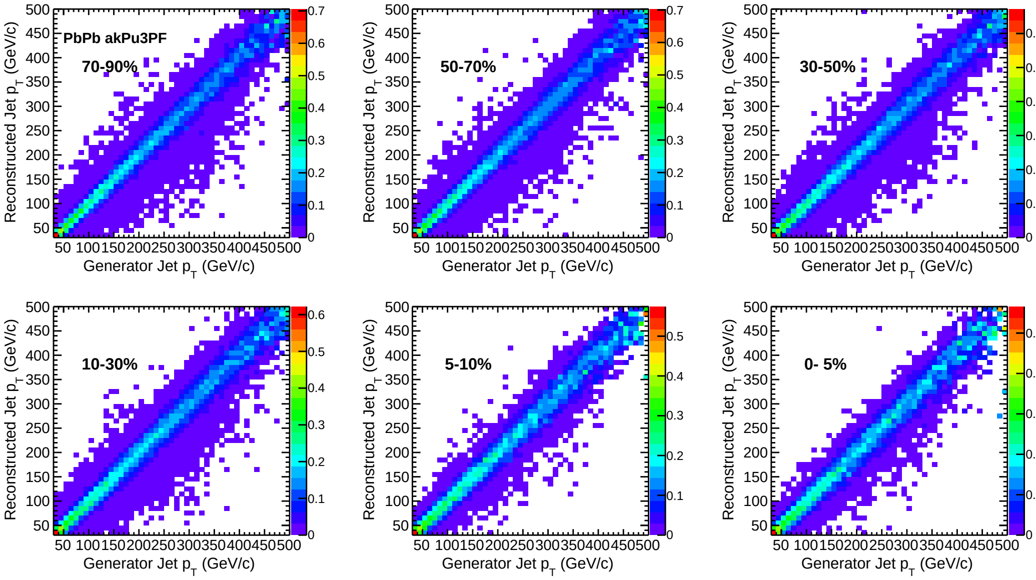

Figure 5.7: Response matrix constructed for PbPb from Bayesian unfolding method in different centrality bins. These are shown for finer bins in the full MC jet p_T range compared to Fig. 5.8.

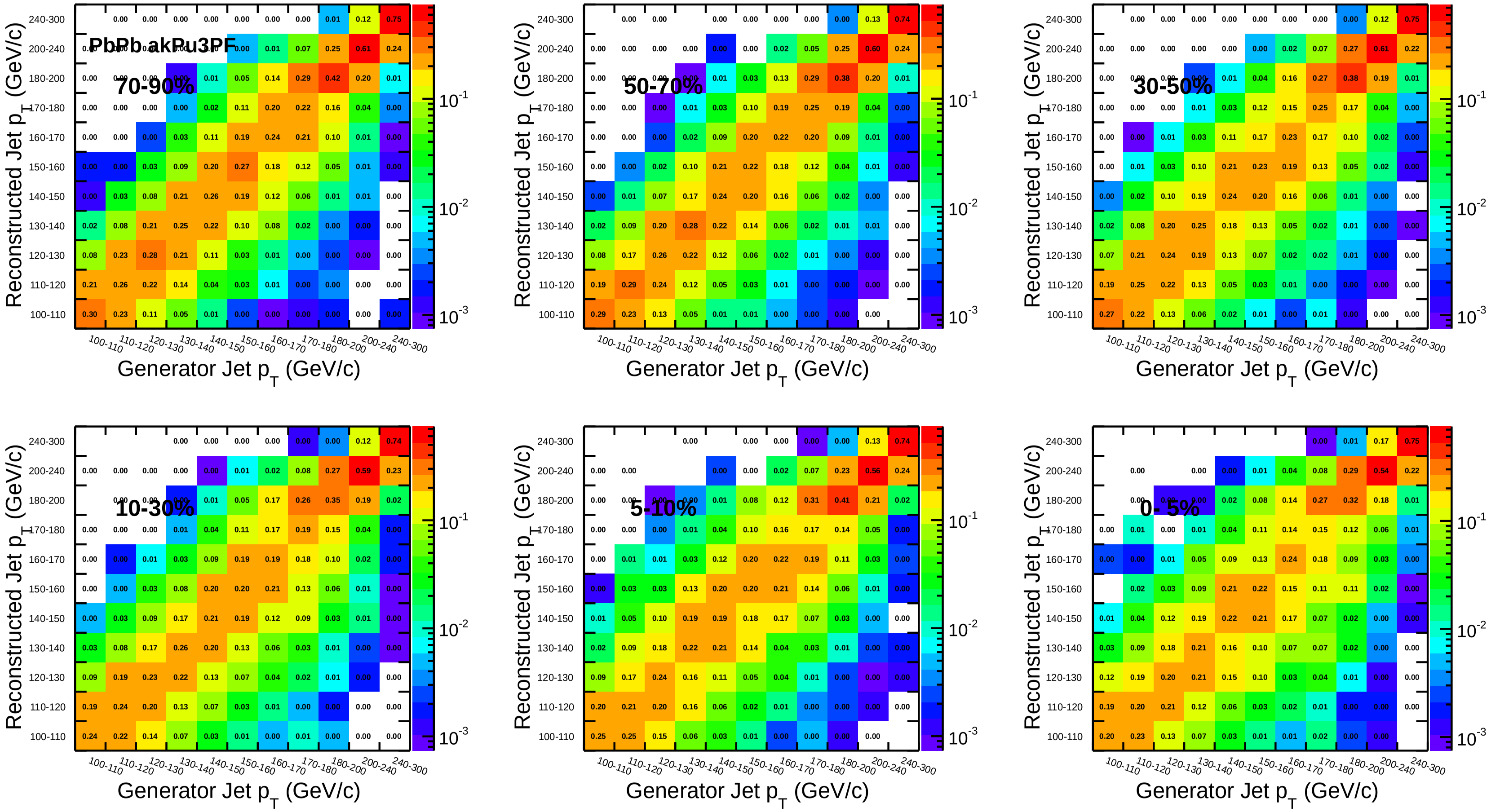

Figure 5.8: Response matrix constructed for PbPb from the Bayesian unfolding method in different centrality bins within the p_T range consistent with the final result.

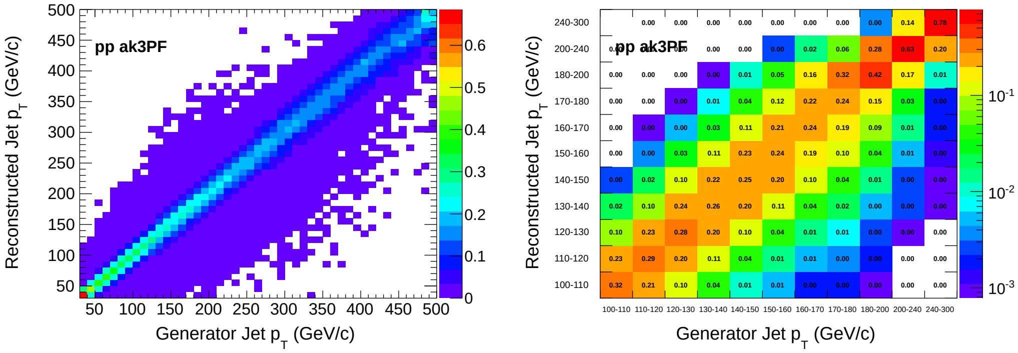

Figure 5.9: Response matrix constructed for pp from the Bayesian unfolding method. Left panel is the original matrix in finer bins and the right panel is consistent with the p_T range utilized in final result in coarser bins.

5.2.1 Bayesian Method and Bin-by-Bin Method

Bayesian unfolding uses the input MC truth and reconstruction information to create a smearing matrix. Using probability theory, the physical quantity of the jet p_T spectra is unfolded from the detector effects that modify it. Apart from the provided implementation of the root-based unfolding (ROOUNFOLD [55]), the standard Richardson–Lucy [52–54] method was also implemented. Correlated error propagation through the Bayesian unfolding is done by taking (numerical) partial derivatives with respect to the input spectrum, and propagating through them. Bayesian unfolding here is performed with 4 iterations. The choice of 4 iterations is twofold: first it is the default and recommended number of iterations for Bayesian unfolding and second, four iterations provide reasonable closure when tested in MC.

Unlike Bayesian unfolding, which allows for the migration of events between bins, the Bin-by-Bin method assumes no migration, and thus corrects for detector effects only in the height of each jet p_T bin. Bin-by-Bin unfolding can be a valid technique in the case where resolution is much smaller than bin size. However, this technique is only shown as a cross-check.

Monte Carlo closure has been done to verify the validity of the unfolding methods. Figures 5.10 and 5.11 show the closure test for the Bayesian and Bin-by-Bin unfolding methods with both pp and PbPb MC samples. This is done by taking half of the MC sample as “data”, and utilizing the other half to unfold the “data”. The jet spectra for unfolded, reconstructed MC jets from the “data” are compared to the generator level jets.

The ratio of unfolded jet spectra to generator level jet spectra and the ratio of measured jet spectra to generator level jet spectra are compared to show the closure of the Bayesian and Bin-By-Bin methods.

5.2.2 GSVD Method

For the (additive) LLS method, an “initial guess” x_{ini} is used to scale the problem such that the unfolding does not have to exhaust its total degrees of freedom (DOF) to purely reproduce the steeply falling spectrum shape. The standard method to perform Phillips–Tikhonov regularization is the generalized singular value decomposition (GSVD). As the different unfolding techniques use the same MC sample as input, the matrix used for GSVD can be seen in Figs. 5.7- 5.9.

To check that the unfolding is working properly, a MC closure test has also been performed. This is shown in Figs. 5.12-5.14 for PbPb in different jet cone sizes.

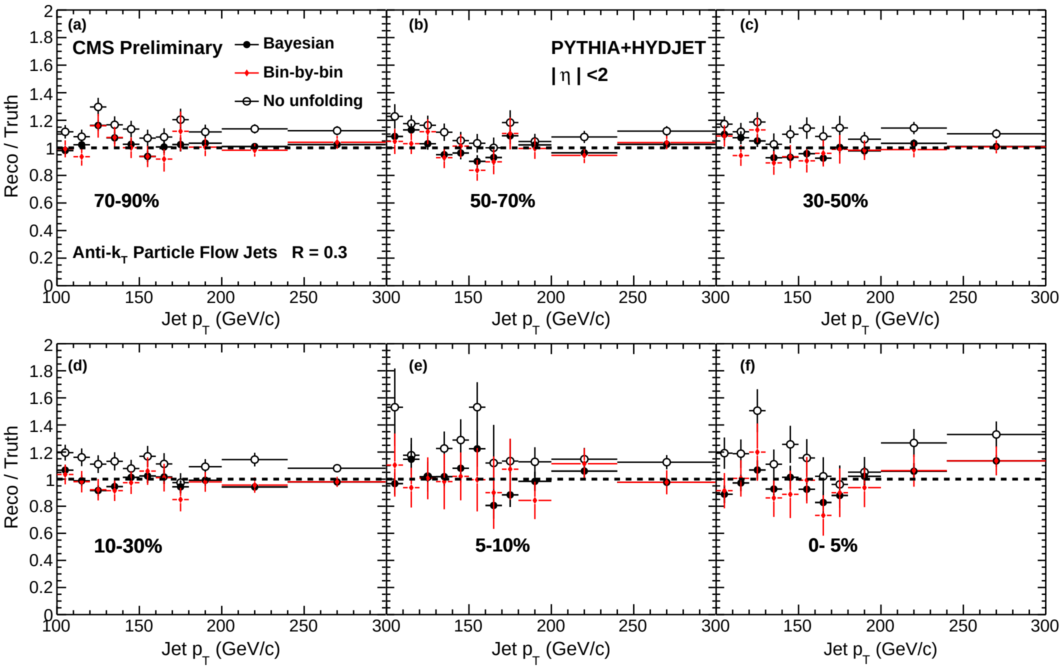

Figure 5.10: PbPb MC closure test for Bayesian method. The results are shown from the most peripheral events (top left) to the most central events (bottom right). The re-weighted and combined MC samples are used here with half being the "fake data" and the other half constructing the resolution matrix to unfold the "fake data". The closure test compares the reconstructed jets with and without unfolding to the generator level truth jets and tests whether the unfolding method is capable of correcting the reconstructed jets to the truth jets.

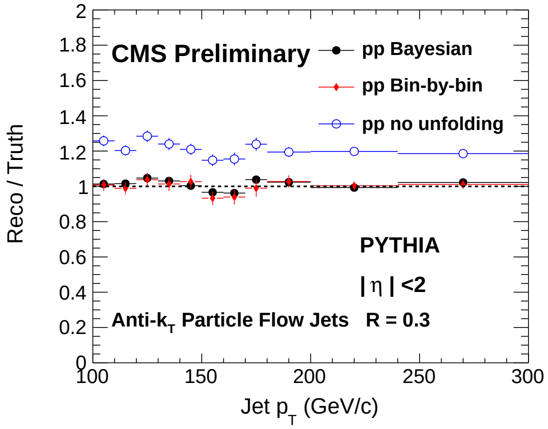

Figure 5.11: pp MC closure test for Bayesian method.

Figure 5.15 shows this same test performed on pp MC.

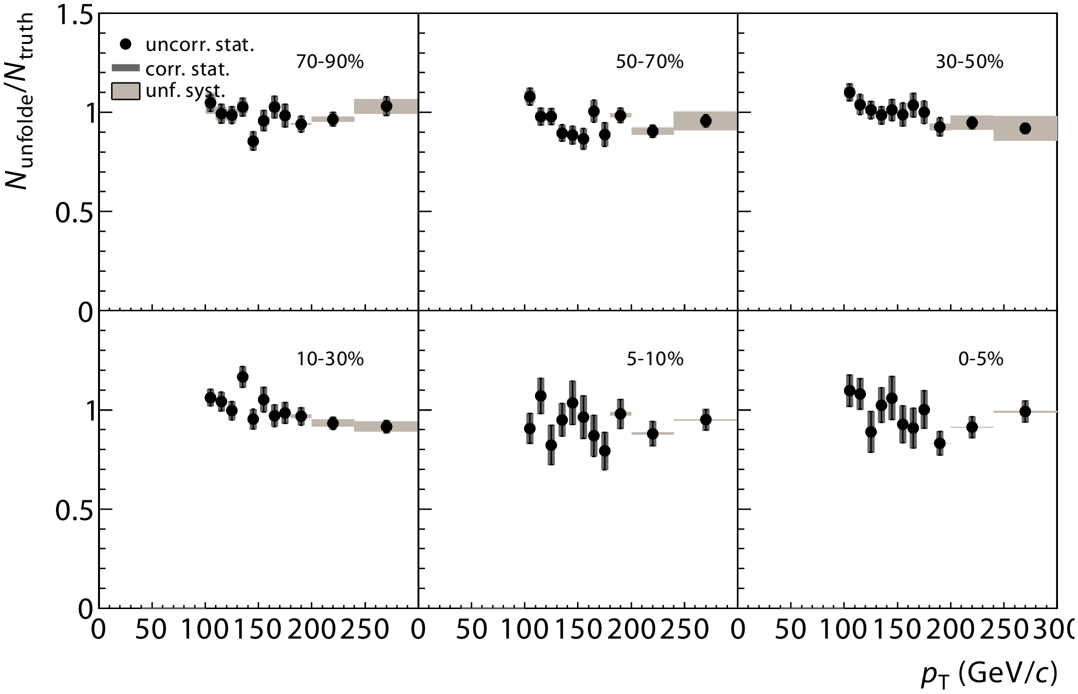

Figure 5.12: PbPb MC closure test for GSVD $R = 0.2$.

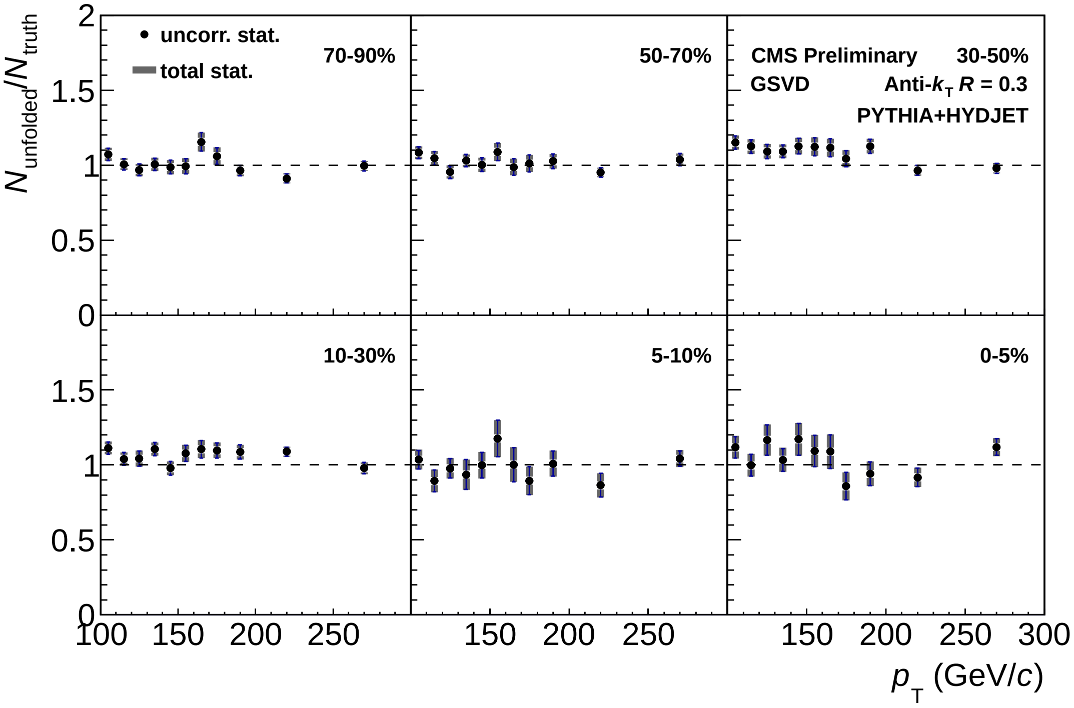

Figure 5.13: PbPb MC closure test for GSVD $R = 0.3$.

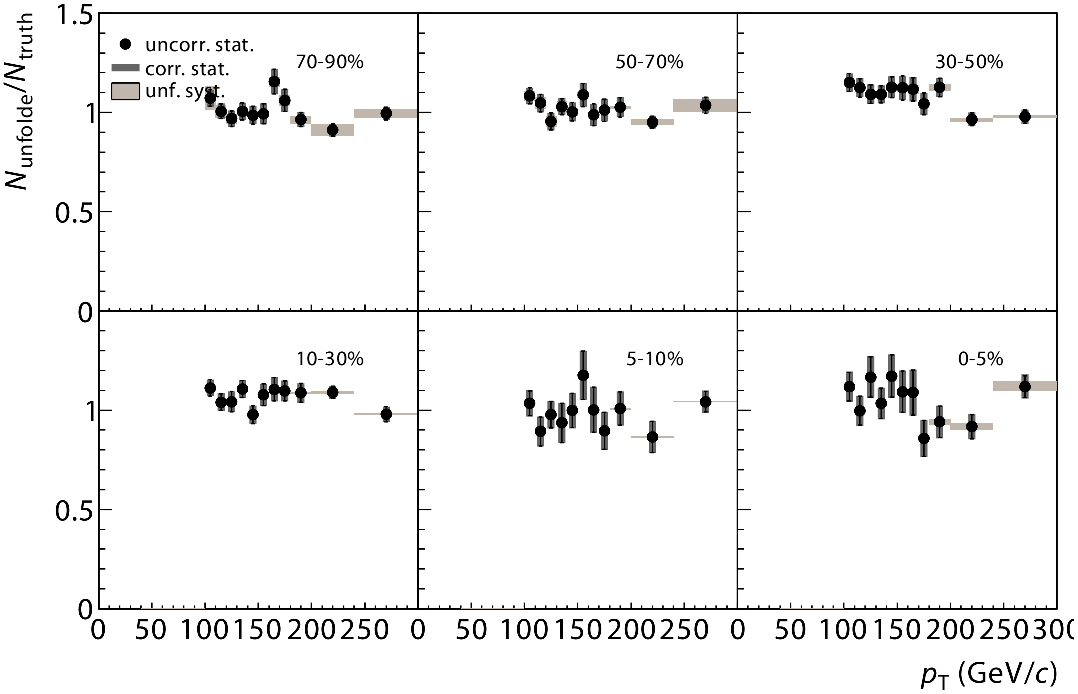

Figure 5.14: PbPb MC closure test for GSVD $R = 0.4$.

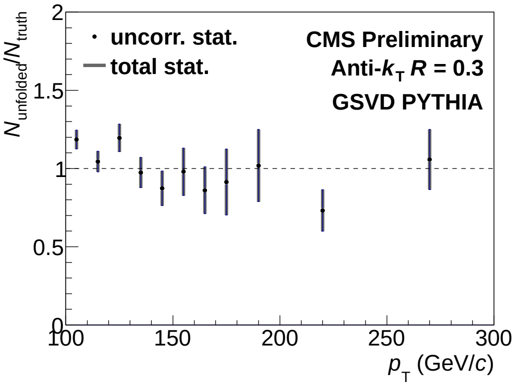

Figure 5.15: Proton-proton MC closure test for GSVD $R = 0.3$.

5.3 Smearing Method

The PbPb and pp jet energy resolutions differ by 5%. To take into account this resolution effect in the reconstructed jet spectra, the pp jet p_T spectra are smeared with the factors obtained from Sec 4.5. The reconstructed jet p_T values in the pp data are smeared by applying a Gaussian distribution, where the sigma of the distribution is the smearing factor obtained from MC. Figures 5.16 and 5.17 show the comparison of the measured pp spectra and the smeared pp spectra. The differences are within 5% and 10% level for the smearing factors obtained from the Bin-by-Bin method and those obtained from the parametrization of the jet energy resolutions, respectively. It is important to note that the pp smearing technique introduced here is used as a cross-check to the unfolding jet R_{AA} analysis and not the main result.

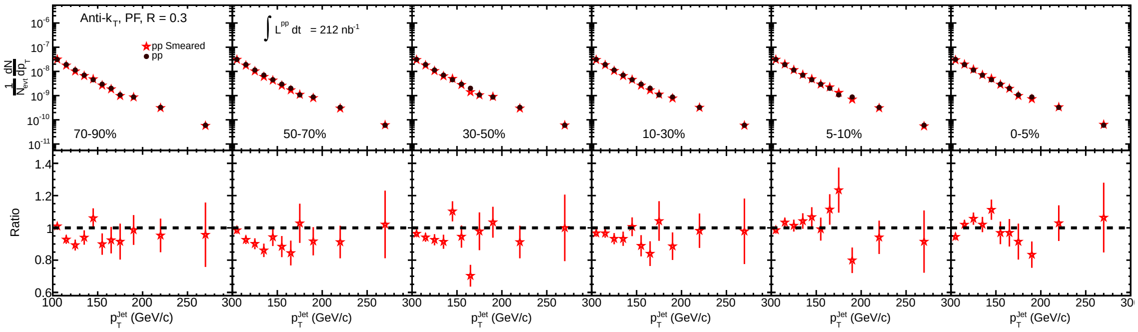

Figure 5.16: Top: Jet p_T spectra for pp collisions with (solid circles) and without (stars) smearing factors obtained by taking the difference in jet energy resolutions in PbPb and pp in quadrature on a bin-by-bin basis. Bottom: Ratio of the pp smeared to the unsmeared spectra.

The jet energy resolution has a centrality- and p_T-dependence, as is seen from Fig. 4.5. This may cause an artifact when the PbPb and pp spectra are divided

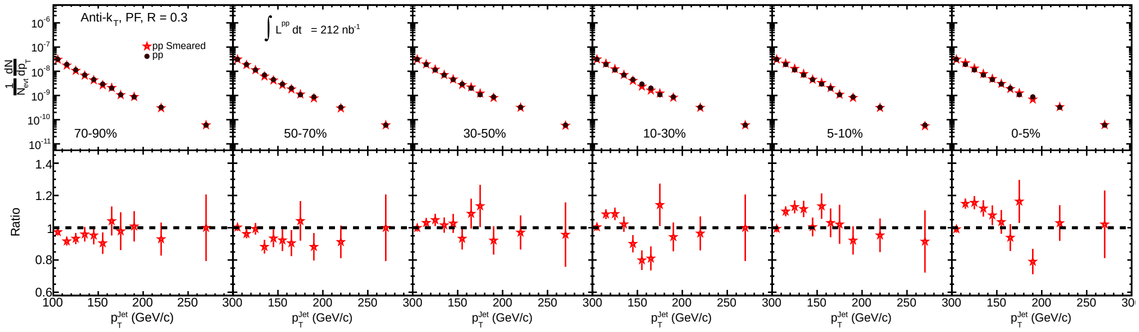

Figure 5.17: Top: Jet p_T spectra for pp collisions with (solid circles) and without (stars) smearing factors obtained by taking the difference in jet energy resolutions in PbPb and pp in quadrature from the parametrization of the resolutions. Bottom: Ratio of the pp smeared to the unsmeared spectra.

to obtain a quantity like R_{AA}. To remove this effect, the pp jet p_T resolution is smeared with a given smearing factor, so as to obtain a jet energy resolution that matches the PbPb jet energy resolution. The smearing factors are obtained using the MC generated events for each centrality bin in PbPb as a function of jet p_T. The smearing of the reconstructed jet p_T in pp is applied with a Gaussian function. For each centrality and jet p_T bin, the smearing factors are provided as the input to the width of the Gaussian that is used to smear the jet p_T. From Fig. 4.5, it can be seen that there is at most a 2% difference in the jet energy scale in the PbPb MC simulations (more at lower jet p_T). To take this effect into account the reconstructed jet p_T is shifted in pp collisions with the difference obtained from the jet energy scale in pp and PbPb in each centrality and as a function of p_T. The smearing factors are calculated by taking the difference of the resolutions between PbPb and pp in quadrature.

Figures 5.18 and 5.19 show the average of the ratio of the RecoJet p_T and the GenJet p_T for all jets above $p_T >$ 80 GeV/c within $|\ \eta\ |<$2.0 in PbPb (open circles),

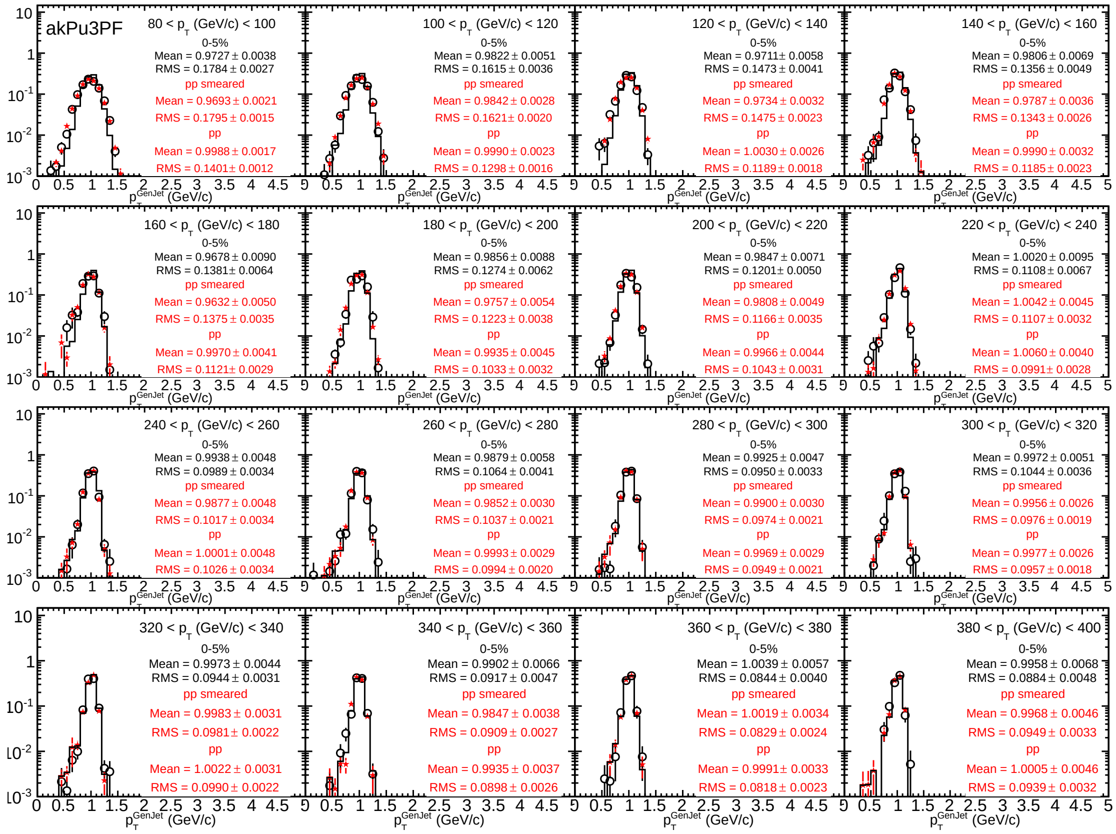

Figure 5.18: The ratio of reconstructed jet and generated jet p_T for PbPb (open circle), smeared pp (closed star) and histograms for the pp collisions for the anti-k_{T} jet algorithm with R=0.3 for 0-5% PbPb collisions in each p_T bin.

smeared pp (closed stars) and pp (line). Most of the smeared pp resolutions match within 5% with the PbPb resolutions. These smearing factors are then applied to the pp data before obtaining the jet R_{AA}.

Figure 5.20 shows the comparison between the smeared pp resolution and the PbPb resolution from the MC. The open stars are the smeared pp resolutions that are made to match the PbPb resolution of the given centrality bin. The bottom panels show the ratio of the resolutions between PbPb and pp with and without smearing factors. Figure 5.21 shows the comparison between the smeared pp resolution and the PbPb resolution from the MC for the jet p_T scale. Due to the small

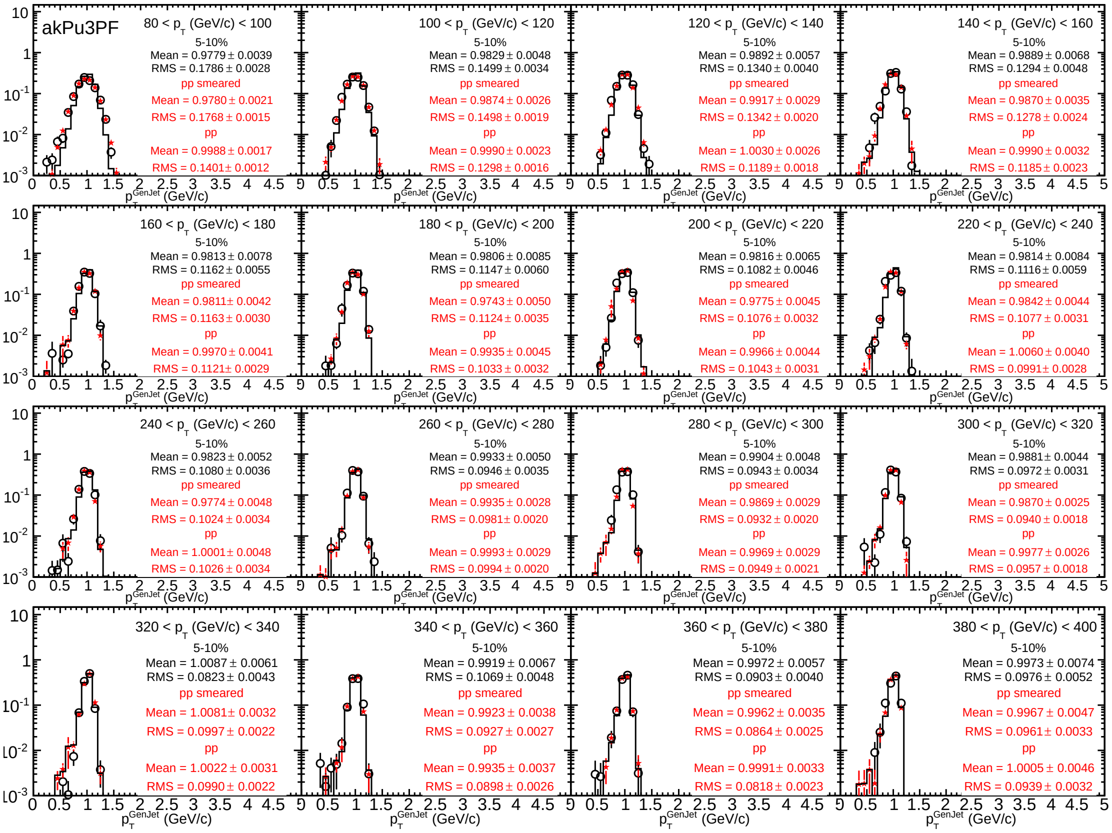

Figure 5.19: The ratio of reconstructed jet and generated jet p_T for PbPb (open circle), smeared pp (closed star) and histograms for the pp collisions for the anti-k_T jet algorithm with R=0.3 for5-10% PbPb collisions in each p_T bin.

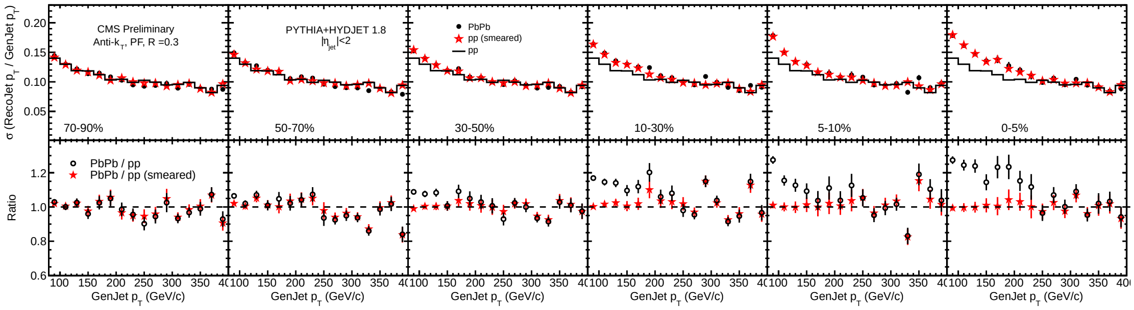

Figure 5.20: Top: σ of the RecoJet p_T over GenJet p_T as a function of centrality for various p_T bins for the anti-k_T jet algorithm with R=0.3. Shown is the PbPb σ (open circles), pp value (histogram), and the results of pp smeared by the jet energy resolution (closed red stars). Bottom: Ratio of PbPb sigma to smeared pp sigma (red stars) and to pp with out smearing factors (open circles) as a function of PbPb collision centrality.

residual left in the jet energy scale in the PbPb events, the mean of the distribution for pp is shifted such that it matches the PbPb jet energy scale. The top panel shows the comparison of the jet energy scales between pp, shifted pp to match the corresponding PbPb jet energy scale and PbPb events. The same procedure was also applied to the data and the reconstructed jet energy was reduced by this difference factor obtained from the MC.

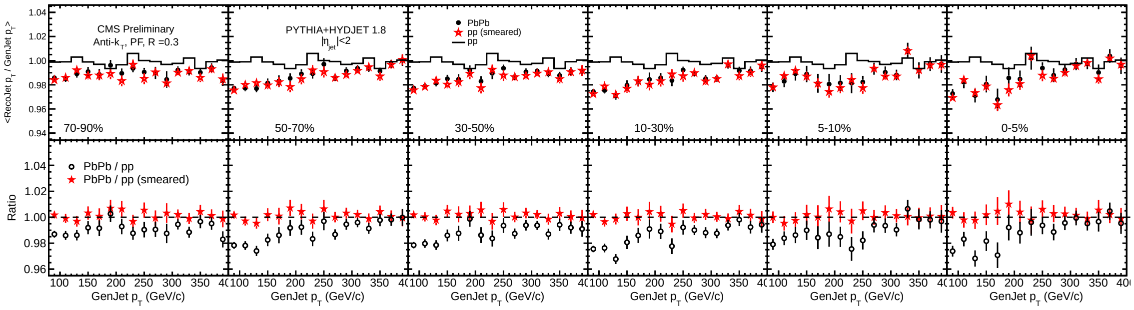

Figure 5.21: Top: Mean of the RecoJet p_T over GenJet p_T as a function of centrality for various p_T bins for the anti-k_T jet algorithm with R=0.3. Shown is the PbPb mean (open circles), pp value (histogram), and the results of pp shifted by the jet energy scale (closed red stars). Bottom: Ratio of PbPb mean to shifted pp mean (red stars) and to pp with out shifting as a function of PbPb collision centrality.

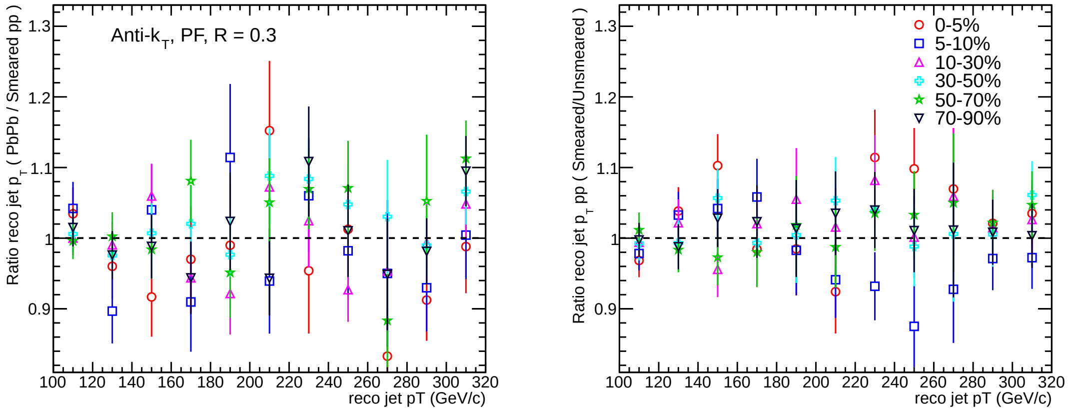

Figure 5.22: Left: Ratio of PbPb jet spectra to bin-by-bin smeared pp jet spectra as a function of reconstructed jet p_T. Right: Ratio of the bin-by-bin smeared and unsmeared pp of the reconstructed jet p_T spectra. Spectra are calculated from MC.

Figure 5.22 shows the MC closure (left) for the PbPb and the smeared pp in the reconstructed jet p_T spectra. The closer the MC smeared pp spectra is to the MC PbPb jet spectra, the better the closure test is. This shows the effectiveness of the pp smearing. The right panel shows the ratio of the smeared and unsmeared reconstructed jet p_T spectra from MC pp events. This shows the effective correction as a function of jet p_T and centrality that is applied to pp spectra.

Alternatively, the smearing factors were also obtained from the parametrization of the jet energy resolutions. The jet energy resolutions are parametrized using the following prescription:

$$\sigma\left(\frac{p_T^{\text{Reco}}}{p_T^{\text{Gen}}}\right) = C \oplus \frac{S}{\sqrt{p_T^{\text{Gen}}}} \oplus \frac{N}{p_T^{\text{Gen}}}, \tag{5.3}$$

where $\oplus$ indicates a sum in quadrature, and the quantities C, S, and N are fitted parameters. The first two terms of the parametrization are determined from PYTHIA (Z2) simulation, and the third term, which represents background fluctuations, is determined from PYTHIA (Z2) + HYDJET 1.8 simulation. Figure 5.23 shows the fit (top) and ratio of fit to the points (bottom). As seen in Table 5.1, C and S are fairly constant across the centrality, while N is increasing from pp to 0–5% PbPb collisions.

Another smearing approach is to fit the jet energy scale, shown in Fig 5.24, with a third order polynomial, though the parametrization in 0–5% and 5–10% centrality bin is not good because of the fluctuating data points. The smearing factors from this parametrization are obtained by the Eq 5.4, assuming that the

Table 5.1: Parameters of the functional form for the jet energy resolution for pp and PbPb centralities (indicated by the % ranges in parentheses). The units of S are $\sqrt{\text{GeV}/c}$ and the units of N are GeV/c.

Species	pp	70–90%	50–70%	30–50%	10–30%	5–10%	0–5%
C	0.05+-0.01	0.06+-0.01	0.05+-0.01	0.06+-0.01	0.04+-0.01	0.01+-0.02	0.05+-0.01
S	1.18+-0.01	1.03+-0.05	1.18+-0.05	1.20+-0.04	1.40+-0.04	1.48+-0.08	1.42+-0.08
N	2.03+-0.32	5.25+-0.41	4.19+-0.54	4.86+-0.4	4.57+-0.54	5.52+-0.84	5.89+-0.77

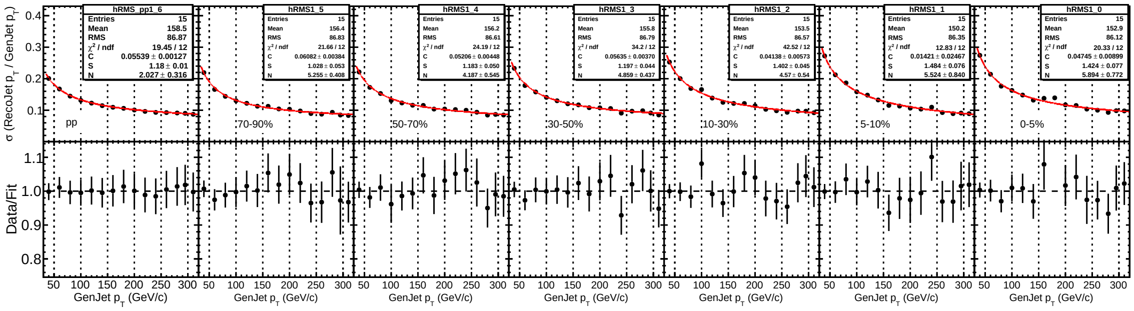

Figure 5.23: Top: Jet energy resolution as function of generated jet p_T fitted to Eq. 5.3 for pp and different collision centralities in PbPb. Bottom: Ratio of the points/fit.

ratio of reco jet p_T / gen jet p_T are Gaussian in nature.

$$SMF = \sqrt{JER_{PbPb}^2 - JER_{pp}^2}, \tag{5.4}$$

where JER_{PbPb} and JER_{pp} are the jet energy resolutions for the PbPb and pp. These smearing factors are calculated for each centrality bin in PbPb and as a function of gen jet p_T. As can be seen from Fig 5.24, there is a difference in jet energy scale in PbPb and pp collisions. To take this into account we also try to shift the jet energy scale in pp while trying to smear it with the smearing factors to obtain the PbPb jet energy resolutions. These mean shifts are within 2% of the pp jet energy scale.

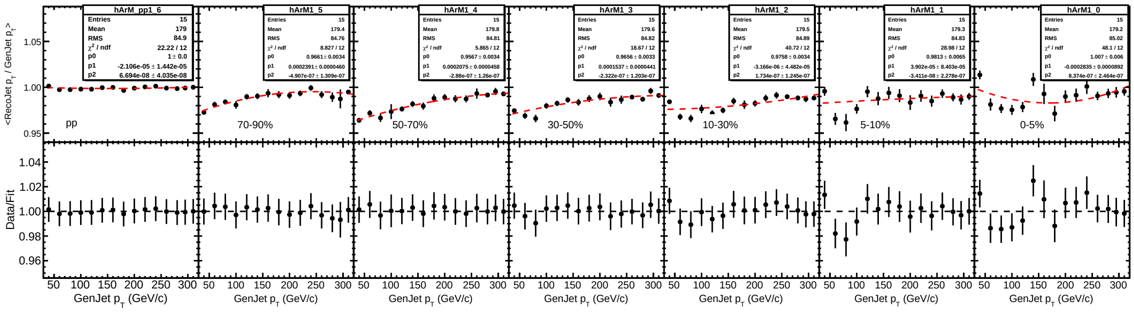

Figure 5.24: Top: Jet energy scale as function of generated jet p_T fitted with a third order polynomial for pp and different collision centralities in PbPb. Bottom: Ratio of the points/fit.

Due to the non-Gaussian nature of the ratio distribution of reco jet p_T and generated jet p_T, additional smearing is required so as to match the PbPb jet energy resolutions. This additional smearing is around 5% of the smearing factors obtained from Eq. 5.4. This can be seen in Fig. 5.25 and Fig. 5.26.

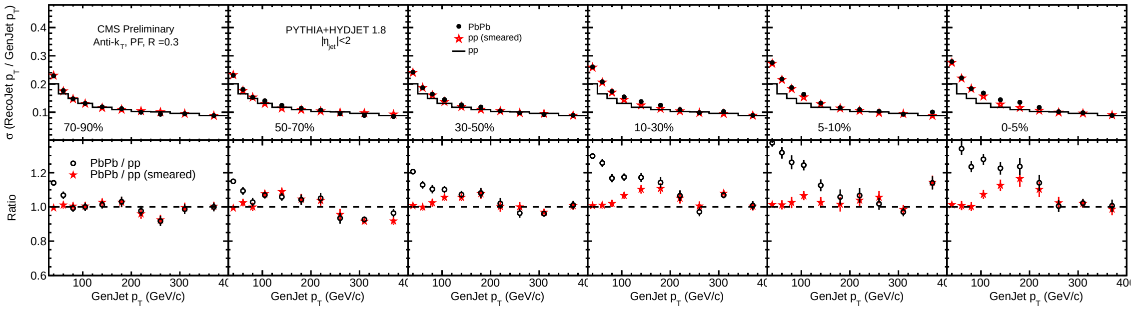

Figure 5.25: Top: Jet energy resolution as function of generated jet p_T for smeared pp reco jet p_T without the afterburner. Bottom: Ratio of the points/fit.

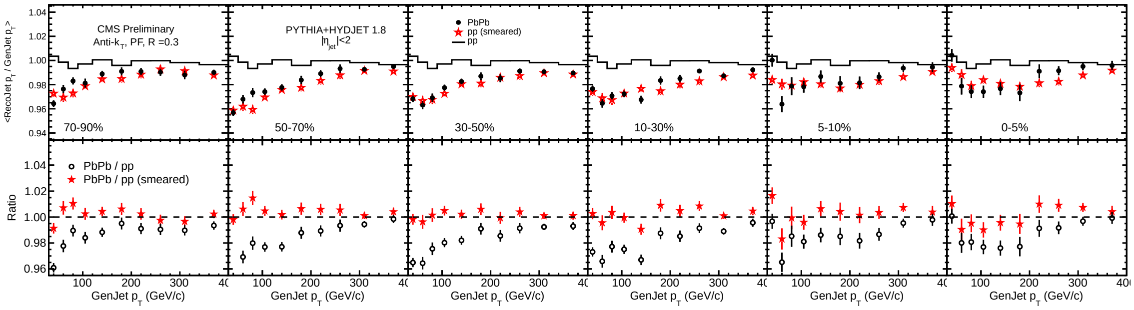

Figure 5.26: Top: Jet energy scale as function of generated jet p_T for smeared pp reco jet p_T without the afterburner. Bottom: Ratio of the points/fit.

Table 5.2 gives the comparison of the smearing factors obtained from bin-by-bin method and the fit resolution method. From Fig. 5.27 to Fig 5.32, it can be seen that the smearing factors work well for the pp collisions. There are slight deviations from the PbPb resolutions, but up to first order the pp distributions are matched well with the PbPb MC.

Table 5.2: Smearing Factors (in GeV/c) for pp in Different PbPb Centralities with Bin-by-Bin and Fit-based Methods.

Centrality	p_T(GeV/c)	Bin-By-Bin	Fit based
0-5%	80	10.60	9.80
	100	10.85	8.70
	120	11.53	12.04
	140	10.09	11.17
	160	11.05	12.04
	180	12.90	13.42
	220	11.25	10.25
	260	6.71	4.25
	300	6.88	4.37
30-50%	80	6.25	5.30
	100	6.02	4.62
	120	6.14	8.57
	140	3.17	8.06
	160	5.89	7.59
	180	3.83	7.24
	220	1.26	4.37
	260	3.89	2.20
	300	1.05	2.41
70-90%	80	2.95	2.61
	100	2.02	2.13
	120	2.99	3.58
	140	0	3.25
	160	0.87	3.86
	180	0.82	3.68
	220	0	0.83
	260	0	0.99
	300	0.01	1.45

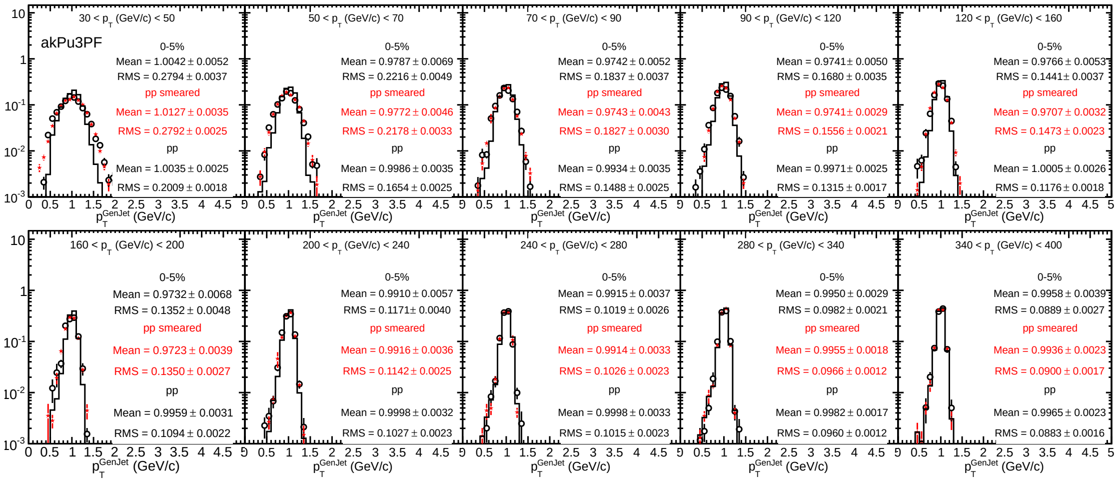

Figure 5.27: Comparison of the ratio of reconstructed jet p_T and the generated jet p_T distributions for pp, smeared pp and 0–5% PbPb collisions.

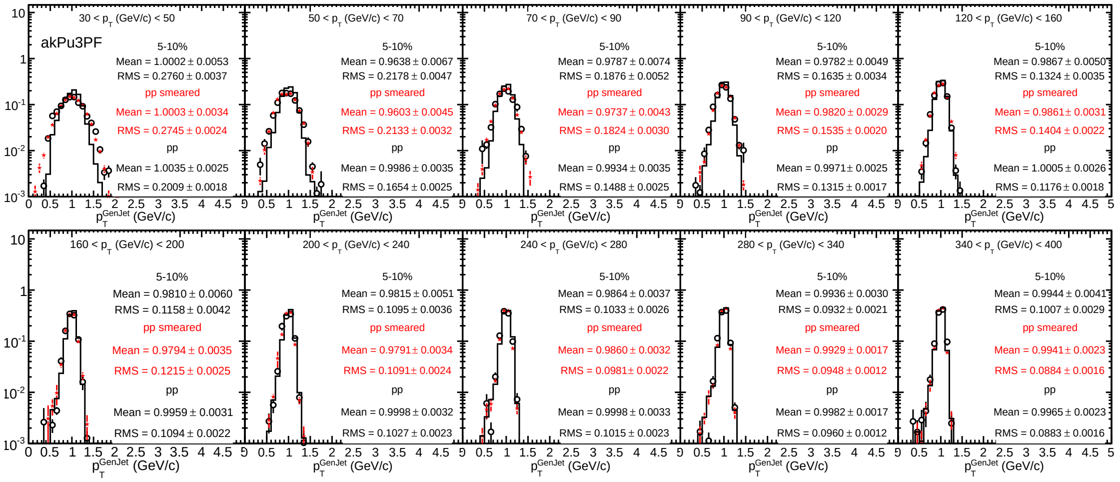

Figure 5.28: Comparison of the ratio of reconstructed jet p_T and the generated jet p_T distributions for pp, smeared pp and 5–10% PbPb collisions.

Figure 5.33 left panel shows the MC closure of the reconstructed jet p_T in pp and different collision centralities in PbPb. The right panel shows the effect of smearing on the reconstructed jet p_T in pp collisions.

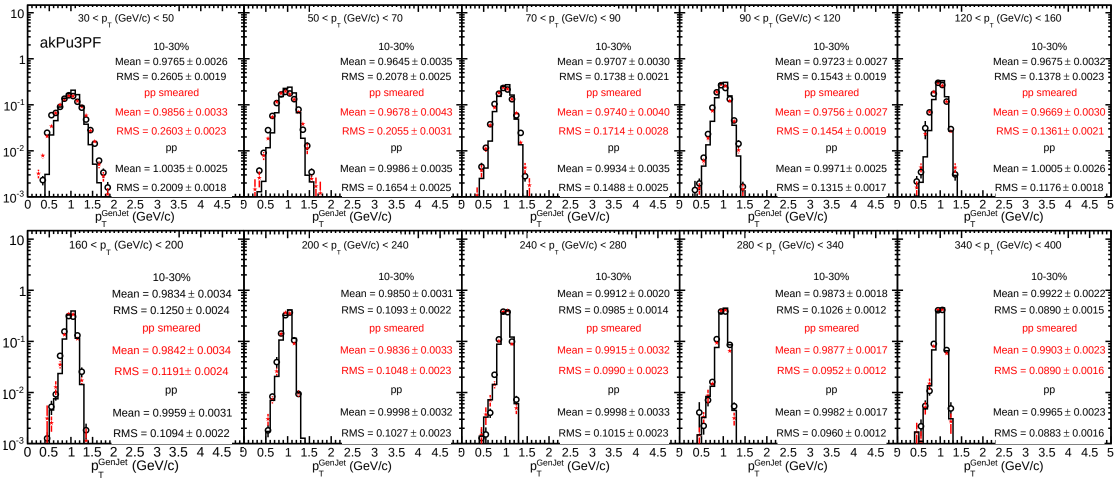

Figure 5.29: Comparison of the ratio of reconstructed jet p_T and the generated jet p_T distributions for pp, smeared pp and 10–30% PbPb collisions.

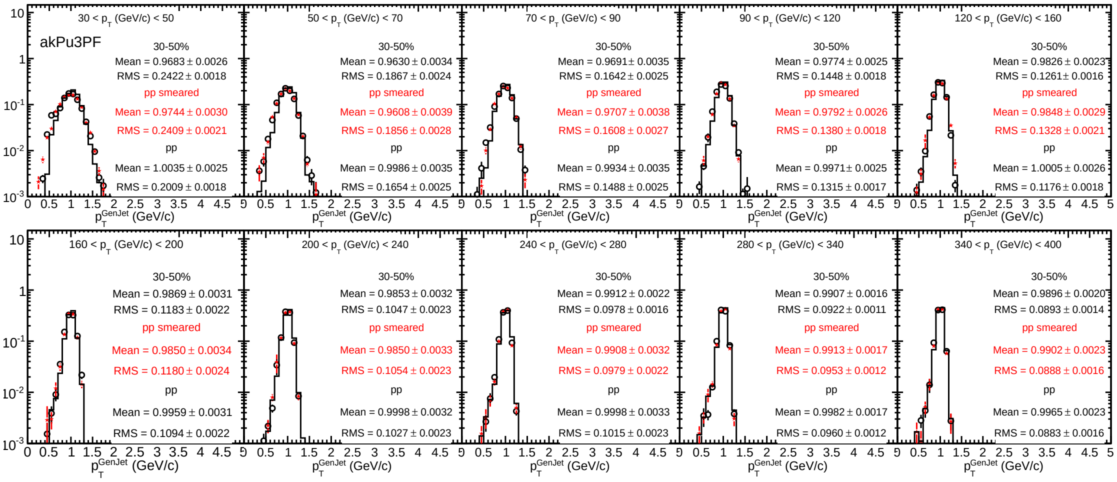

Figure 5.30: Comparison of the ratio of reconstructed jet p_T and the generated jet p_T distributions for pp, smeared pp and 30–50% PbPb collisions.

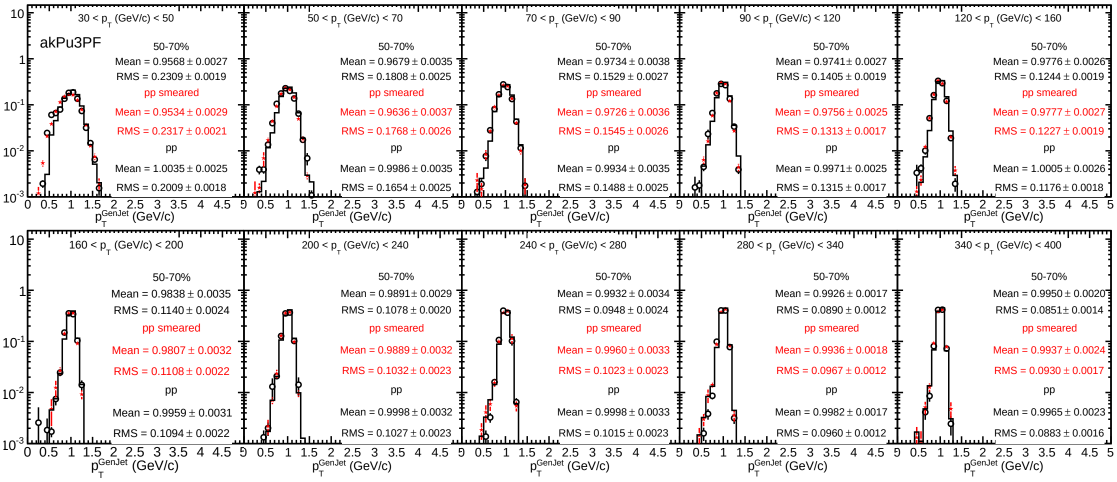

Figure 5.31: Comparison of the ratio of reconstructed jet p_T and the generated jet p_T distributions for pp, smeared pp and 50–70% PbPb collisions.

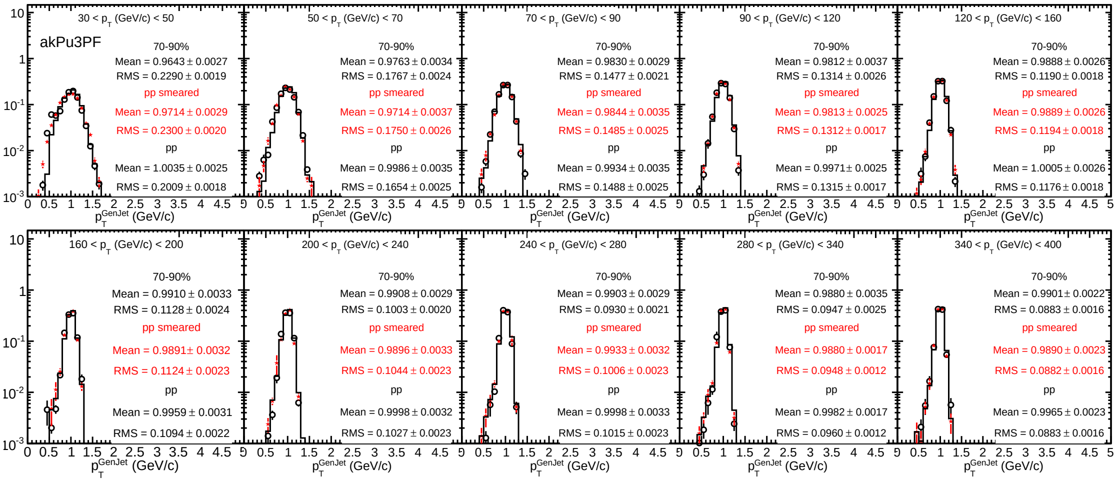

Figure 5.32: Comparison of the ratio of reconstructed jet p_T and the generated jet p_T distributions for pp, smeared pp and 70–90% PbPb collisions.

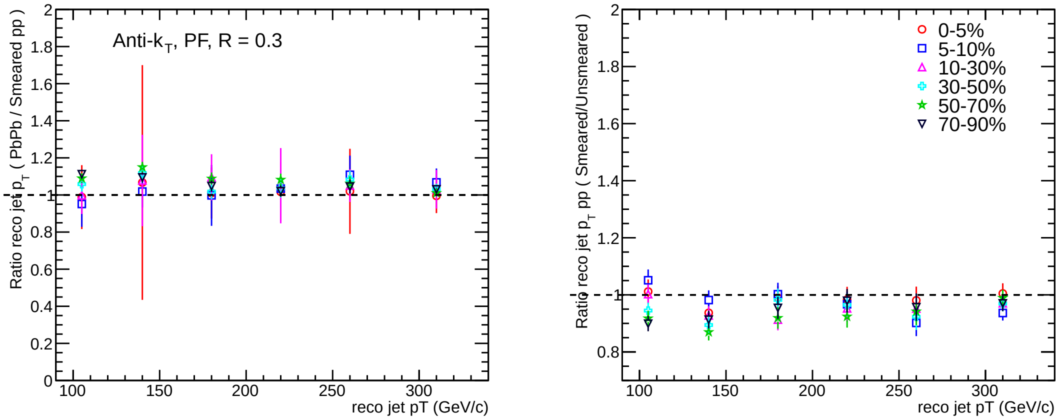

Figure 5.33: Left: Ratio of reconstructed jet p_T between pp and different collision centralities in PbPb. Right: Ratio of smeared and unsmeared reconstructed jet p_T for pp collisions. Different markers are the smearing factors according to the PbPb centralities.

Chapter 6

Systematic Errors

A variety of studies to investigate the systematic uncertainties of the inclusive jet spectra were performed. The dominant systematic uncertainties are from jet energy scale, jet energy resolution unfolding, T_{AA} uncertainty and pp integrated luminosity. These are described in the following sections.

The total systematic uncertainties of the jet nuclear modification factor measurement is summarized in Sec. 6.9.

6.1 Jet Resolution Systematics

In Fig. 4.5 (top) the jet resolution is shown for pp and PbPb as a function of jet p_T, as well as centrality bin (PbPb). The effect of the jet resolution and jet energy scale to the jet spectra is corrected with the unfolding step. In order to study the uncertainty related to the unfolding method and regularization, the following checks are done.

For the Bayesian unfolding, the systematic uncertainty is studied by varying the number of unfolding iterations, as shown in Fig. 6.1. The difference between the results from alternative number of iterations to 4 iterations is quoted as the systematic uncertainty. The typical size of this uncertainty for the Bayesian unfolding method is 10-17%. This is a standard technique used in unfolding studies.

The systematic uncertainty from unfolding found from the Bayesian technique is of a similar order of magnitude as that from the other unfolding techniques and pp smearing.

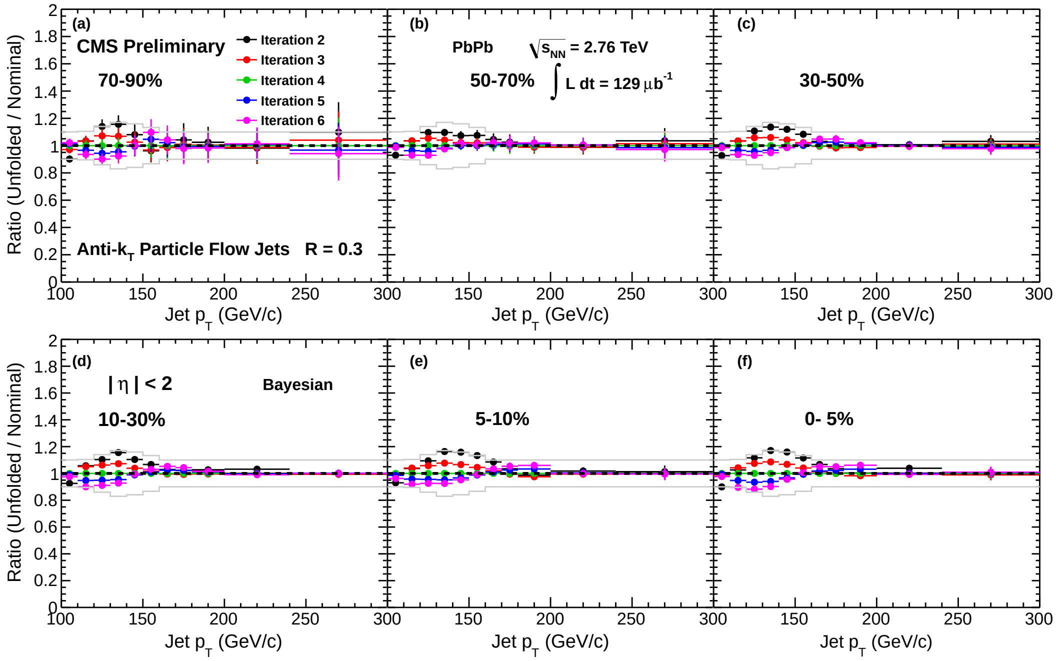

Figure 6.1: Bayesian unfolding method in various iterations. The systematicsrepresented as the grey envelope are derived from the ratios of various iteration numbers of to 4 iterations.

In the case of the pp smearing analysis, this effect is corrected directly by smearing the pp spectra. The jet resolution difference between pp and PbPb is taken as a function of centrality and jet p_T and the systematic uncertainty is estimated to be 10-20% based on the comparison between PbPb spectra and smeared pp spectra (Fig. **??**).

6.2 Background Fluctuation

To estimate the possible difference between data and MC in terms of in-cone background fluctuations that may directly affect the jet energy resolution, the following cross-checks are done in order to probe the difference. The soft PbPb background is shown to be well modeled by the MC, as can be seen in the background jet p_T (Fig. 4.1). To quantify the possible difference, random cone studies were performed and the width was compared between Minimum Bias events in data and MC simulation (Fig. 4.4). The difference in width (estimated by a Gaussian fit to the random cone energy) is found to be smaller than 1 GeV/c.

The jet p_T spectra were smeared by a Gaussian distribution with a width of 1 GeV/c and smeared spectra were compared to the original spectra. The difference is found to be smaller than 2%, which is quoted as the systematic uncertainty.

6.3 Hadronic Calorimeter Noise

The anomalous electronic signals from the Hadronic Calorimeter accounts for the main contributor to the noise in the inclusive jets study. Figures 6.2 and 6.3 show the fraction of jets in the event that pass the HCAL noise rejection, which has a rejection efficiency of $\sim 70\%$ based on studies with di-jet pairs, as a function of the leading akPu3PF jet after collision event selection is applied. The estimated fraction of HCAL noise before noise rejection is up to ∼10-20% after collision event selection.

As stated in Chapter 3, the offline selection for jets is $|\eta| < 2$, jet $p_T >$

100 GeV/c, the primary vertex cut of 15 cm, and the maximum track p_T / reconstructed jet $p_T > 0.01$. By using events that are rejected by the HBHE noise filter, the track-based jet ID selection efficiency can be studied in a data-driven way, which is illustrated in Fig. 6.4 and 6.5. The combined rejection efficiency based on the studies of di-jet events and non-collision events is estimated to be $\sim 95\%$. With a 95% noise rejection efficiency, the estimated remaining contribution of the HCAL noise is 0-1%, increasing as a function of jet p_T, which is quoted as the systematic uncertainty.

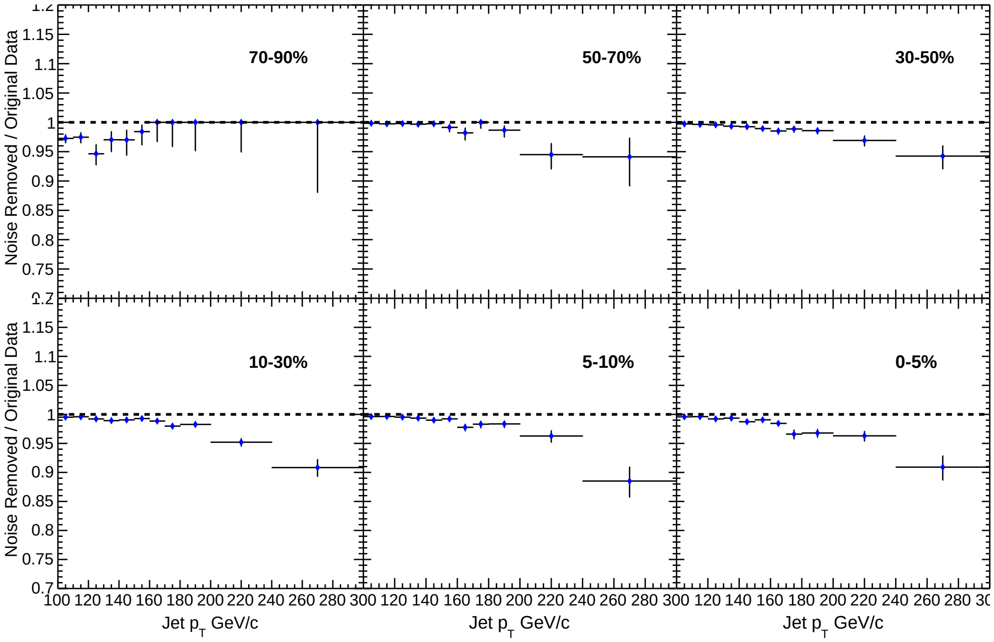

Figure 6.2: The ratio of the anti-k_T particle flow inclusive jet spectra in cone size 0.3 with HCAL noise rejection to the jet spectra without HCAL noise rejection for PbPb in different centrality bins.

The effect of the jet quality track p_T cut and the HCAL noise cut were studied in PbPb and pp data, and included in the systematic uncertainty. Additionally, the effect of the jet quality maximum track p_T selection was studied in simulation.

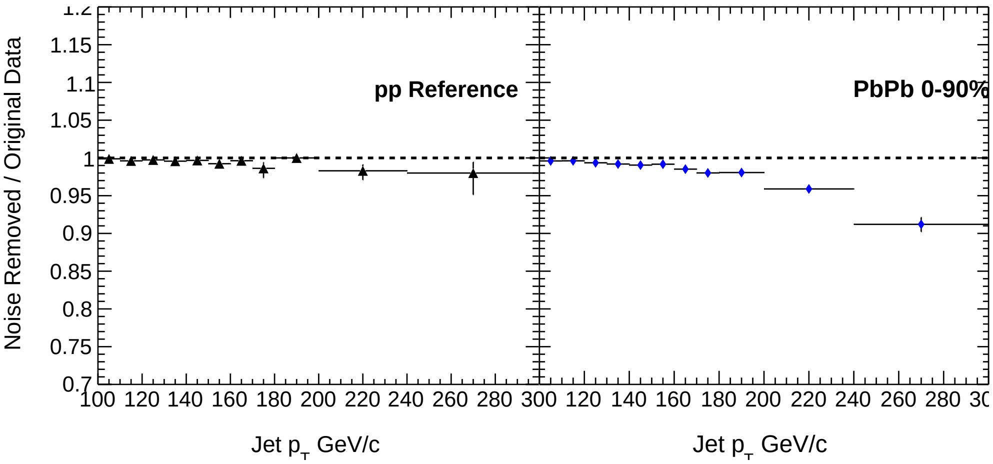

Figure 6.3: The ratio of the anti-k_T particle flow inclusive jet spectra in cone size 0.3 with HCAL noise rejection by the jet spectra to that without HCAL noise rejection for PbPb 0-90% and pp reference data.

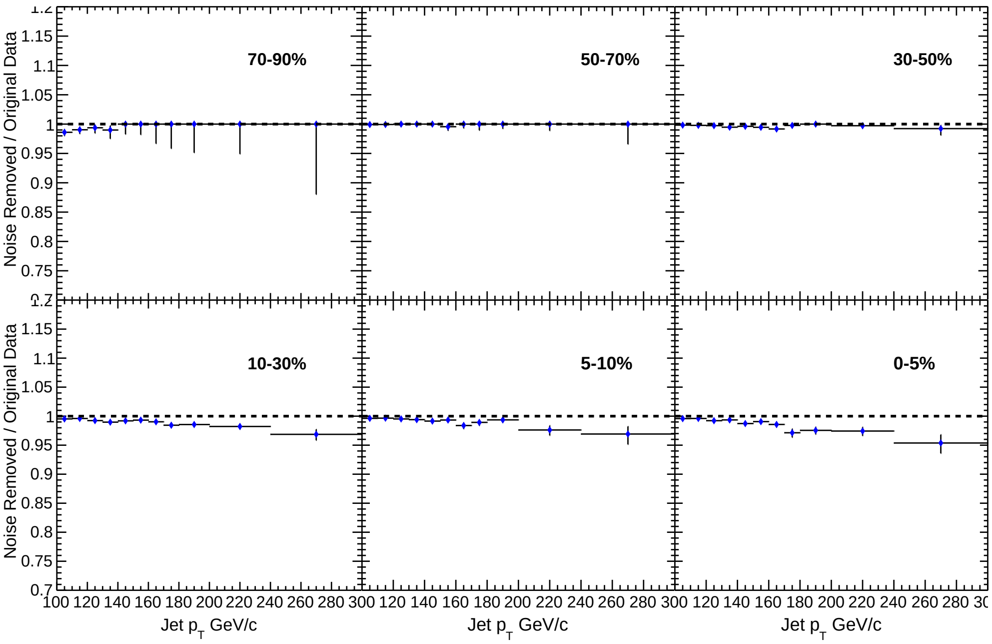

Figure 6.4: The jet spectra after maximum track p_T selection. The ratio of the anti-k_T particle flow inclusive jet spectra in cone size 0.3 with HCAL noise rejection to the jet spectra without HCAL noise rejection for PbPb in different centrality bins.

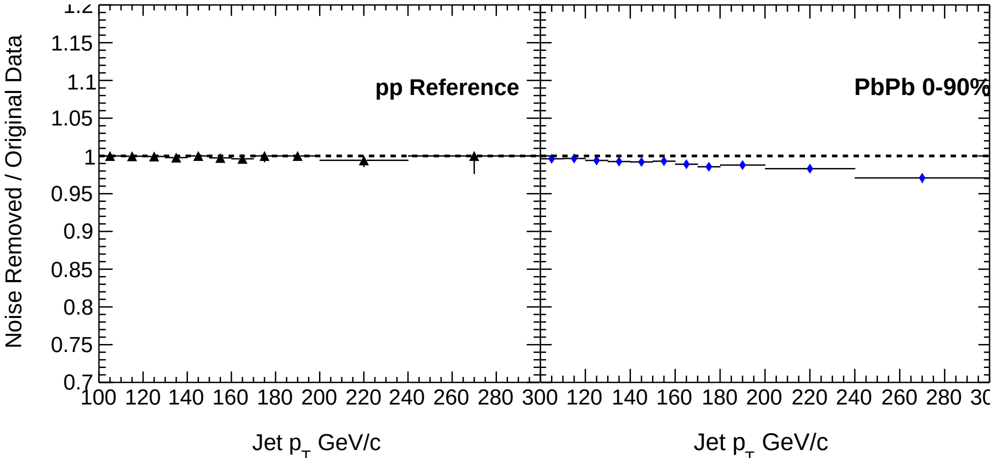

Figure 6.5: The jet spectra after maximum track p_T selection. The ratio of anti-k_T particle flow inclusive jet spectra in cone size 0.3 with HCAL noise rejection to the jet spectra without HCAL noise rejection for PbPb 0-90% and pp reference data.

Figure 6.6 shows the jet selection efficiency as a function of reconstructed jet p_T for MC simulations of di-jet (pp), as well as di-jet embedded into PbPb background (PbPb). One jet selection efficiency number is taken for each of the PbPb centralities and pp, as is shown in Table 6.1. The jet R_AA is corrected by the ratio of PbPb to pp jet finding efficiencies. It is important to note that this factor is done as a correction to the overall jet R_AA and not an uncertainty.

Table 6.1: Jet Selection Efficiency from MC Studies.

Centrality	Jet selection efficiency
0–5%	0.998
5–10%	0.998
10–30%	0.995
30–50%	0.991
50–70%	0.987
70–90%	0.977
pp	0.966

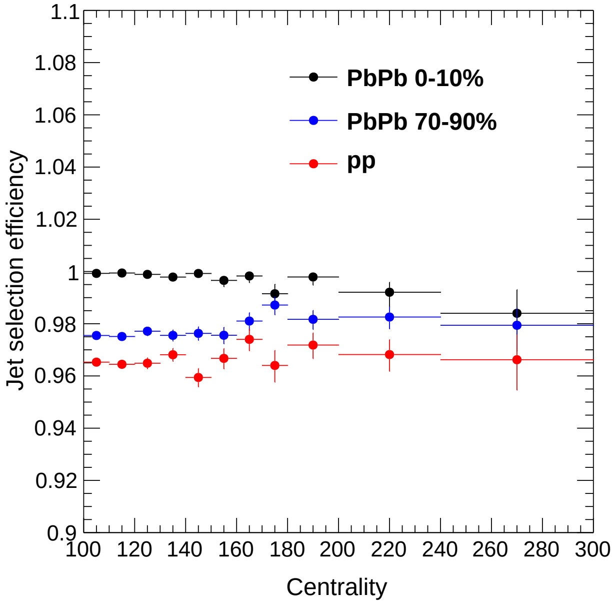

Figure 6.6: Jet efficiency as a function of jet p_T for the selection (maximum track p_T within the jet)/(jet $p_T > 0.01$) for Monte Carlo simulations of pp dijets, as well as pp dijets embedded in PbPb simulated background (PbPb) for two different centralities, covering the most central two centrality bins (0-10%), as well as the most peripheral (70-90%).

6.4 Jet Finding Efficiency Uncertainty

As shown in Fig. 4.3, the jet finding efficiency calculated with dijet PYTHIA +HYDJET sample is greater than 99% with jet $p_T > 100$ GeV/c in all centrality ranges. There is no centrality dependence found in the kinematic range $p_T > 100$ GeV/c. The jet finding efficiency uncertainty is therefore evaluated to be $< 1\%$.

6.5 Jet Trigger Efficiency Uncertainty

As shown in Fig. 3.1 , the jet trigger efficiency calculated with the minimum-bias sample is greater than 99% with jet $p_T > 100$ GeV/c in all centrality ranges. A 1% jet trigger efficiency uncertainty is therefore assumed.

6.6 Luminosity and Event Selection Uncertainty

In this analysis, reconstructed jet spectra in pp collisions are used as a reference in the nuclear modification factor calculations. Systematic uncertainty related to the integrated luminosity of the pp sample is 6% as measured in the inclusive isolated photon R_{AA} analysis.

The recorded number of minimum-bias event (N_{MB}) is estimated by counting the number of minimum-bias triggered events, corrected by the averaged prescale and event selection efficiency. The uncertainty of event selection efficiency is estimated to be 3%.

6.7 Jet Energy Scale Uncertainty

Figure 4.5 shows the jet energy scale for pp and PbPb simulations. The uncertainty in the scale of jet p_T can contribute to the final jet $R_{\rm AA}$ measurement by introducing an uncertainty in which bin a particular jet should be placed in, shifting it left or right for the jet spectra. The largest uncertainty in the jet energy scale in comparison between pp and PbPb is 2%. To estimate the contribution of the jet energy scale to the final jet $R_{\rm AA}$, the jet energy scale is varied by 0-2% (in different centrality bins). The ratio between the varied unfolded spectra to the nominal (unvaried) unfolded jet spectra is shown in Fig. 6.7. The resulting variation in the spectra is used for the systematic uncertainty in the jet $R_{\rm AA}$.

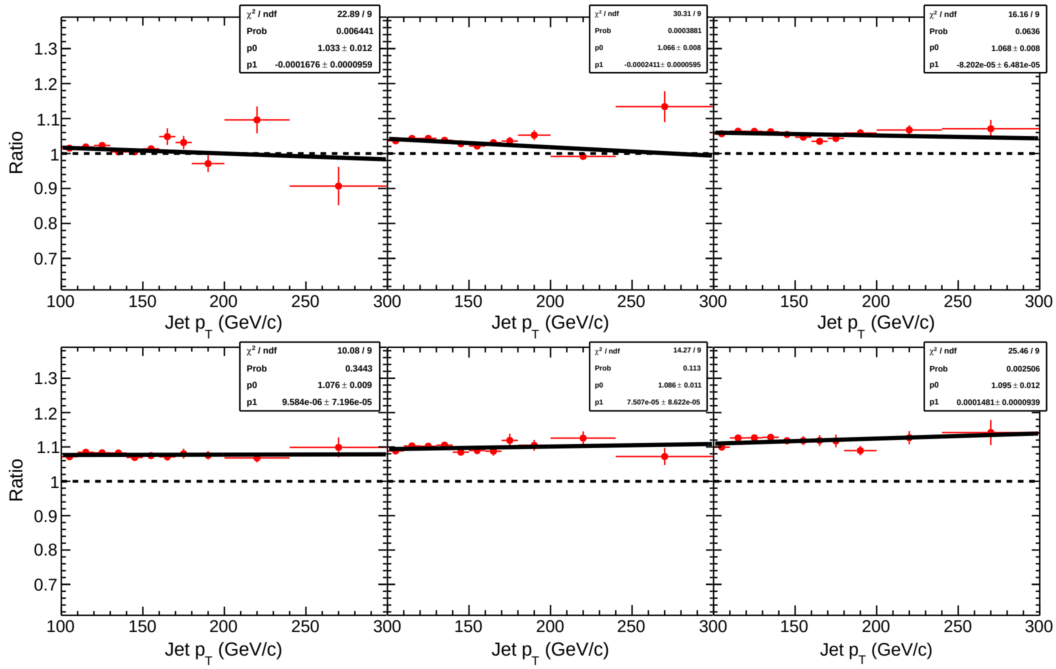

Figure 6.7: Ratio between unfolded jet p_T spectra varied by the 2% jet p_T scale and the unvaried jet p_T spectra.

6.8 Uncertainty in T_{AA}

In units of 1/mb, the $< T_{AA} >$ in PbPb collisions at $\sqrt{s_{NN}} = 2.76$ TeV is summarized in Table. 6.2. The $< T_{AA} >$ in each centrality bin used in this study is identical to what is used in charged particle R_{AA} analysis [56]. These numbers are computed with a Glauber Model calculation [26], using the same parameters as in [24]. The quoted uncertainties are derived by varying the Glauber parameters and the Min-Bias trigger and event selection efficiencies within uncertainties.

Table 6.2: The average number of participating nucleons $< N_{\text{part}} >$, number of binary nucleon-nucleon collisions $< N_{\text{coll}} >$, and nuclear overlap function $< T_{\text{AA}} >$ for the centrality bins used in this analysis. The r.m.s. (root-mean-squared) values give the spread over the centrality bins, which are expressed as fractions of the total inelastic PbPb cross section.

Centrality bin	$\langle N_{\text{part}} \rangle$	r.m.s.	$\langle N_{\text{coll}} \rangle$	r.m.s.	$\langle T_{\text{AA}} \rangle$ (mb^{-1})	r.m.s.
0–5%	381 ± 2	19.2	1660 ± 130	166	25.9 ± 1.06	2.60
5–10%	329 ± 3	22.5	1310 ± 110	168	20.5 ± 0.94	2.62
10–30%	224 ± 4	45.9	745 ± 67	240	11.6 ± 0.67	3.75
30–50%	108 ± 4	27.1	251 ± 28	101	3.92 ± 0.37	1.58
50–70%	42.0 ± 3.5	14.4	62.8 ± 9.4	33.4	0.98 ± 0.14	0.52
70–90%	11.4 ± 1.5	5.73	10.8 ± 2.0	7.29	0.17 ± 0.03	0.11

6.9 Total Systematics

Based on the studies summarized in this chapter, the systematic uncertainties for Bayesian unfolded jet R_{AA} are summarized in Table. 6.3. The total systematic uncertainty is the contributions added in quadrature, giving 12-21% (for centralities from peripheral to central).

The different contributions to the total systematic uncertainty as a function

Table 6.3: Summary of the Systematic Uncertainties.

Source	Jet R_{AA}
Jet trigger efficiency	1%
Jet reconstruction efficiency	$< 1\%$
Jet energy scale	2-10%
Jet resolution unfolding	10-17%
Detector noise	0-1%
Underlying Events fluctuation	2%
pp integrated luminosity	6%
PbPb event selection (N_{MB})	3%
Total	12%-21%

of jet p_T can be seen in Fig. 6.8, with the total shown in grey.

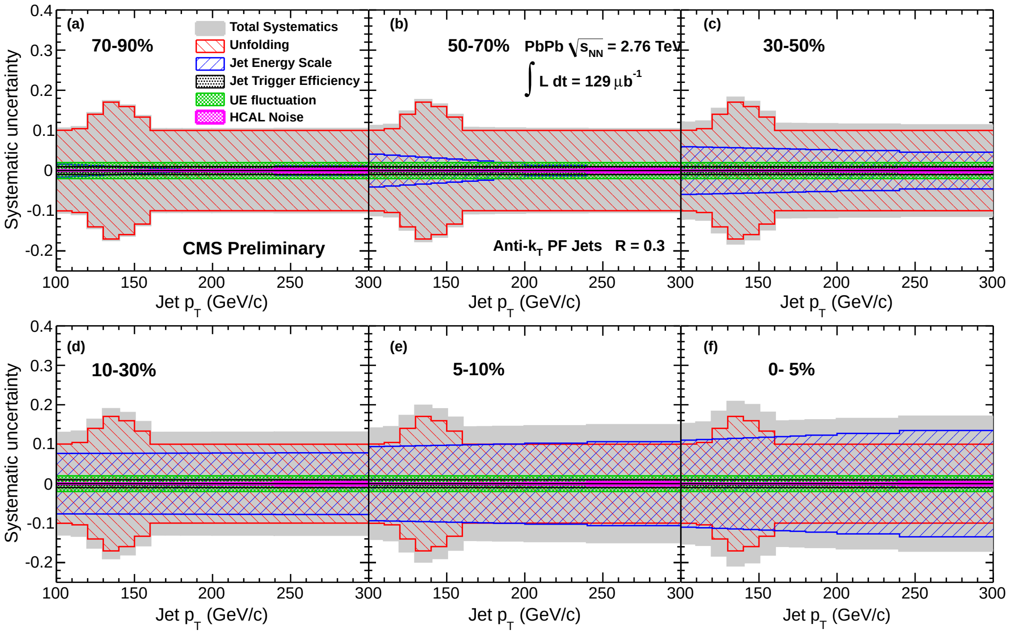

Figure 6.8: Total systematic uncertainties. The grey band represents the total systematics with the red stripes representing the biggest uncertainties, contributed by unfolding iterations in the Bayesian method.

Chapter 7

Results

7.1 Jet R_{AA} vs. p_T Result

The main jet R_{AA} result is shown in Fig. 7.1, corrected by the Bayesian unfolding method with anti-k_{T} particle flow jets of a 0.3 resolution parameter with a pile-up subtraction for PbPb collisions (ak3PuPF) and no pile-up subtraction for pp collisions (ak3PF). Due to the effects of unfolding corrected jet p_T, the unfolded jet spectra are not bin-by-bin uncorrelated. The statistical uncertainty is separated into the uncorrelated (thin vertical line), and the total statistical uncertainty (including correlated) represented by a thicker magenta vertical box. The systematic uncertainty, described in Chap. 6, is indicated by a wide grey band over the whole jet p_T range. An overall uncertainty combining the uncertainty of T_{AA} and the luminosity is shown as a green box located at above jet p_T of 300 GeV/c. For the most peripheral PbPb collisions, the nuclear modification factor is around 0.9. The jet R_{AA} lowers with decreasing collision centrality, reaching the value of 0.5 and independent of jet p_T in the p_T range studied in this analysis.

Figure 7.2 is the final R_{AA} result for ak3PuPF with all of our correcting methods including Bayesian unfolding, GSVD unfolding, Bin-by-Bin unfolding, and pp smearing method. The R_{AA} without unfolding, i.e. measured R_{AA}, is presented in hollow black points as a comparison. Observations can be made from this figure

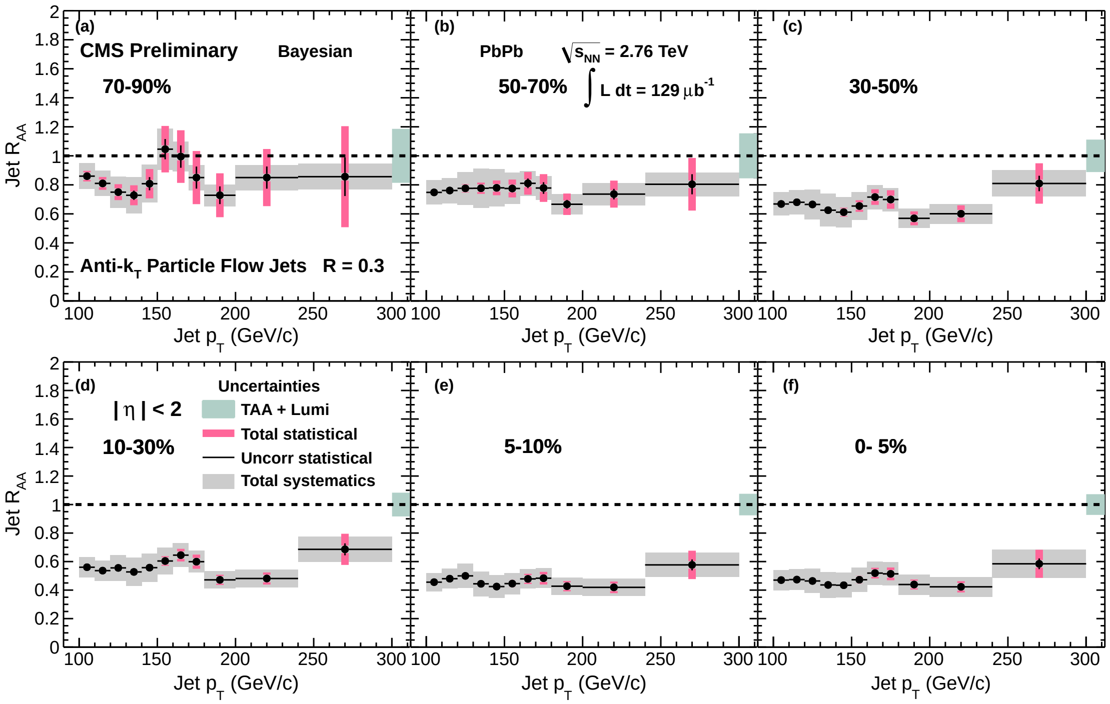

Figure 7.1: Bayesian unfolded jet R_{AA} for anti-k_{T} jets of R=0.3. Bars represent the uncorrelated statistical uncertainty, thin magenta vertical bands the total statistical uncertainty, and the wide grey band represents the systematic uncertainty. The overall combined uncertainty from T_{AA} and luminosity is represented as a green box above 300 GeV/c.

that all the methods have a consistent jet R_{AA} within the uncertainties.

The jet R_{AA} in Fig. 7.3 shows anti-k_{T} particle-flow jets reconstructed with different effective cone sizes with Bayesian unfolding. The systematic uncertainty (grey box) is shown for only R=0.3 jets. Jets of different sizes, thus sampling different amount of p_T, show the same jet R_{AA} from 100 to 300 GeV/c within the uncertainties. Bin-by-Bin unfolding of anti-k_{T} particle-flow jets reconstructed with different effective cone sizes is shown in Fig. 7.7, which serves as a cross-check and is consistent with the Bayesian unfolding.

In a previous CMS measurement of the the jet fragmentation function [57]

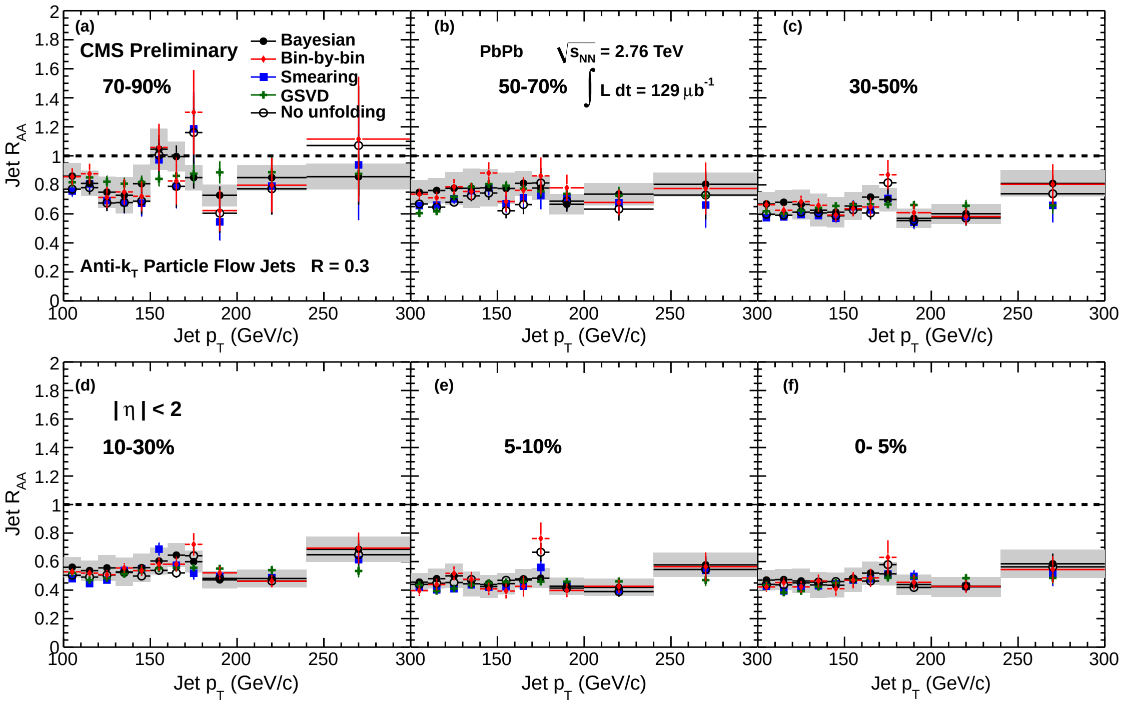

Figure 7.2: Jet R_{AA} constructed for ak3PuPF jets using Bayesian unfolding, GSVD unfolding, and Bin-by-Bin unfolding, as well as pp smearing for the given centrality bins. The thin lines indicate uncorrelated statistical uncertainty and the wide band the systematic uncertainty for Bayesian unfolding.

(into tracks $p_T > 4$ GeV/c), it was found that di-jet pairs in PbPb, both imbalanced and balanced, fragment like those of pp. This indicates that there should be little difference in the amount of suppression as a factor of jet size for PbPb jets.

Additional cross-checks of jet R_{AA} are shown in Fig. 7.4 to 7.9. Fig. 7.4 and 7.5 are the third unfolding method implemented in this analysis, GSVD, to correct the anti-k_T reconstructed jets in various cone sizes. Figures 7.6 to 7.7 illustrate anti-k_T particle flow jets with pile-up subtraction in different cone sizes for various unfolding methods. Jet reconstruction in this document is performed with particle-flow objects, that is consisting of matching information from the tracker and calorimeters.

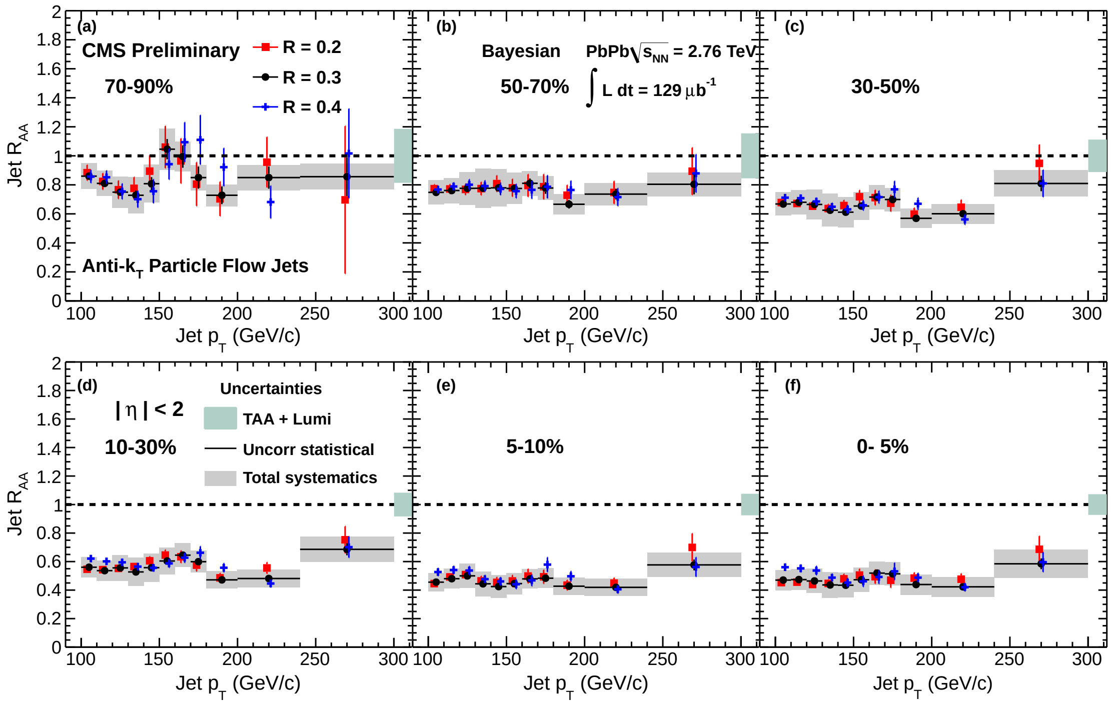

Figure 7.3: Jet R_{AA} in various resolution parameters for anti-k_{T} jets using Bayesian unfolding method for the given centrality bins. The lines indicate uncorrelated statistical uncertainty, and the wide band the systematic uncertainty for Bayesian unfolding R=0.3. The green box above 300 GeV/c represents the overall combined uncertainty from T_{AA} and luminosity.

To remove the tracking from the analysis, jets are reconstructed from calorimeter objects using the same anti-k_{T} algorithm, R=0.3, and the iterative "noise/pedestal subtraction" technique to remove the PbPb background. Jets reconstructed in pp are found the same way without background subtraction. As particle-flow jets include tracking information, the CMS detector η and p_T jet energy correction amount is smaller than that used in calorimeter jets, which gives a smaller uncertainty from that correction. The jet R_{AA} constructed from Bayesian unfolded calorimeter jets is shown in Fig. 7.8 in comparison to the particle-flow results. Even with the differences in jet reconstruction technique, the results are equivalent. Figure 7.9 and

7.10 are other cross checks from pp smearing with ak3PF jets, as a comparison the Bayesian result and the one without unfolding are on the same plot.

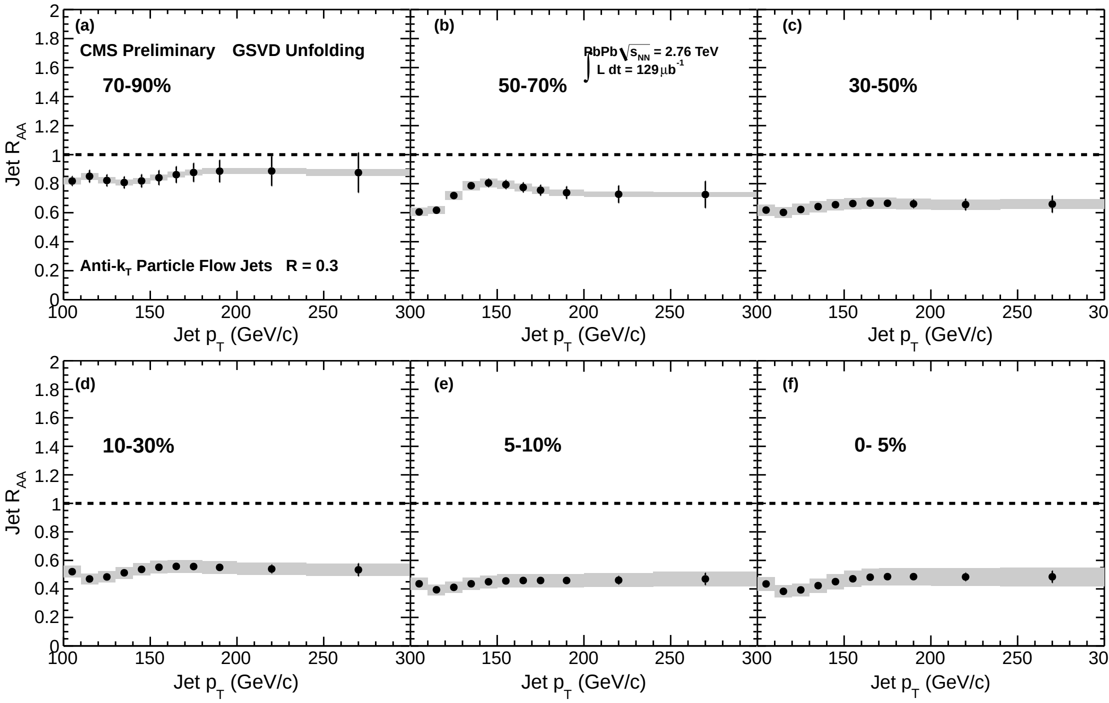

Figure 7.4: Jet R_{AA} constructed by anti-k_{T} particle flow jets in cone size 0.3 using GSVD unfolding.The total systematics are represented by the grey band.

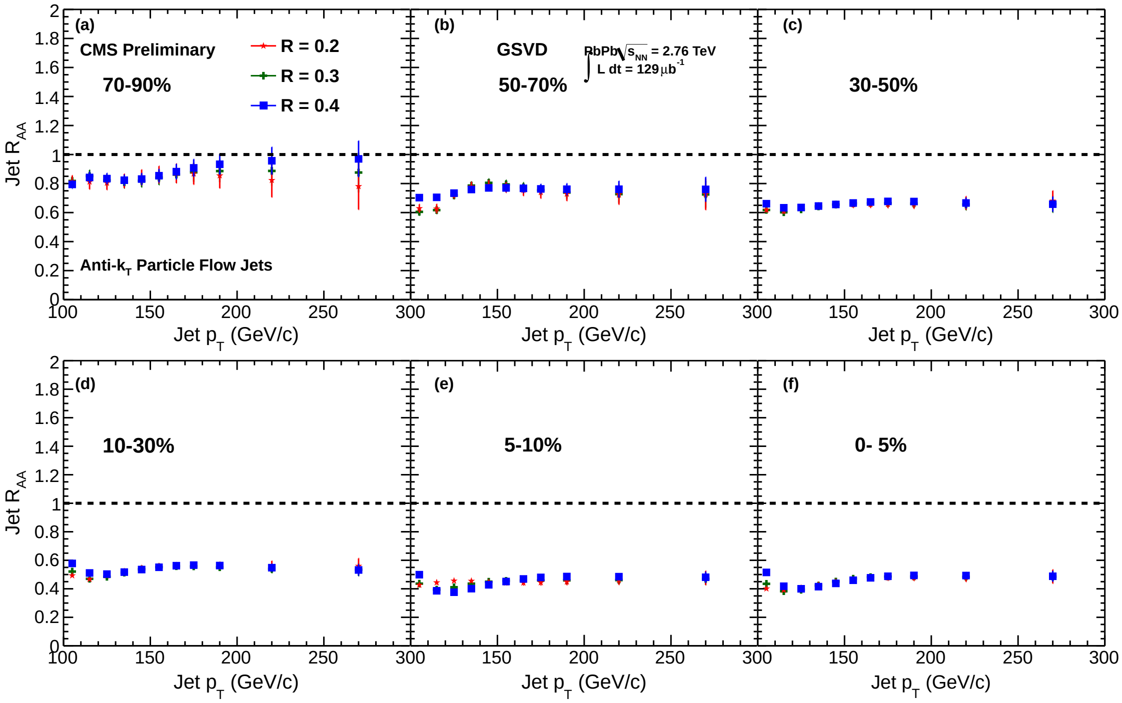

Figure 7.5: R_{AA} in different cone sizes for anti-k_{T} particle flow jets in cone size 0.3 with GSVD unfolding method.

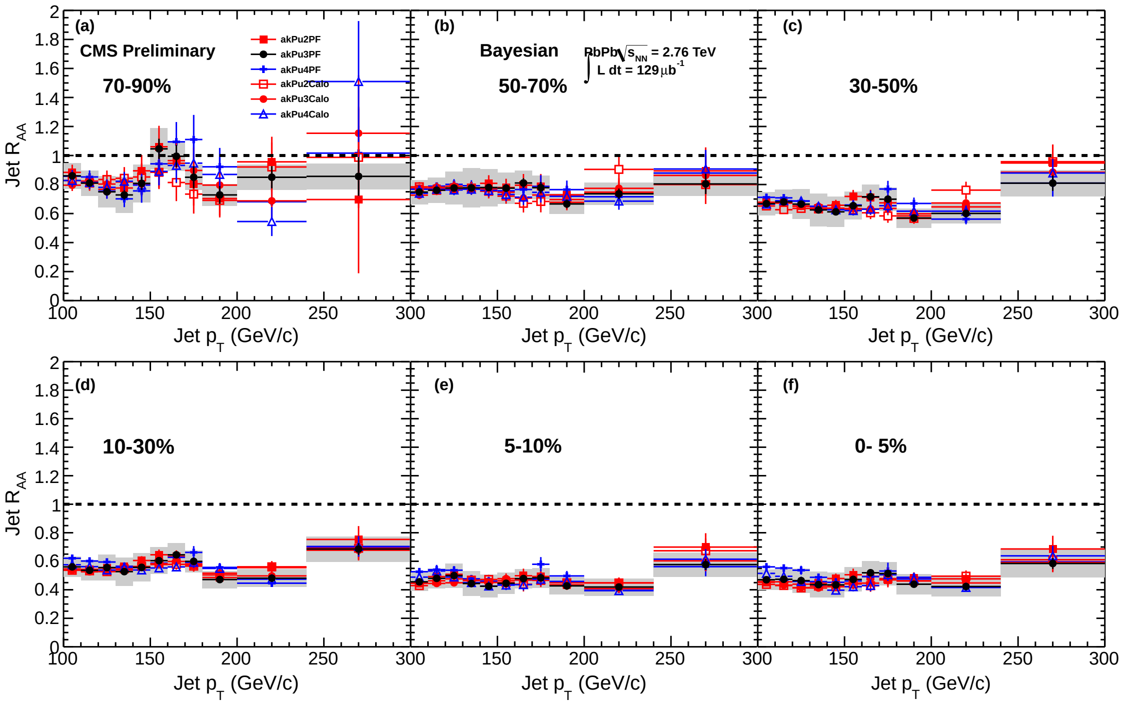

Figure 7.6: R_{AA} in different cone sizes for anti-k_{T} particle flow jets (akPuPF) and anti-k_{T} calorimeter jets (akPuCalo) with Bayesian method. The total systematics are only calculated for ak3PuPF jets. The result shows consistency between different cone size jets, as well as between particle-flow and calorimeter jets.

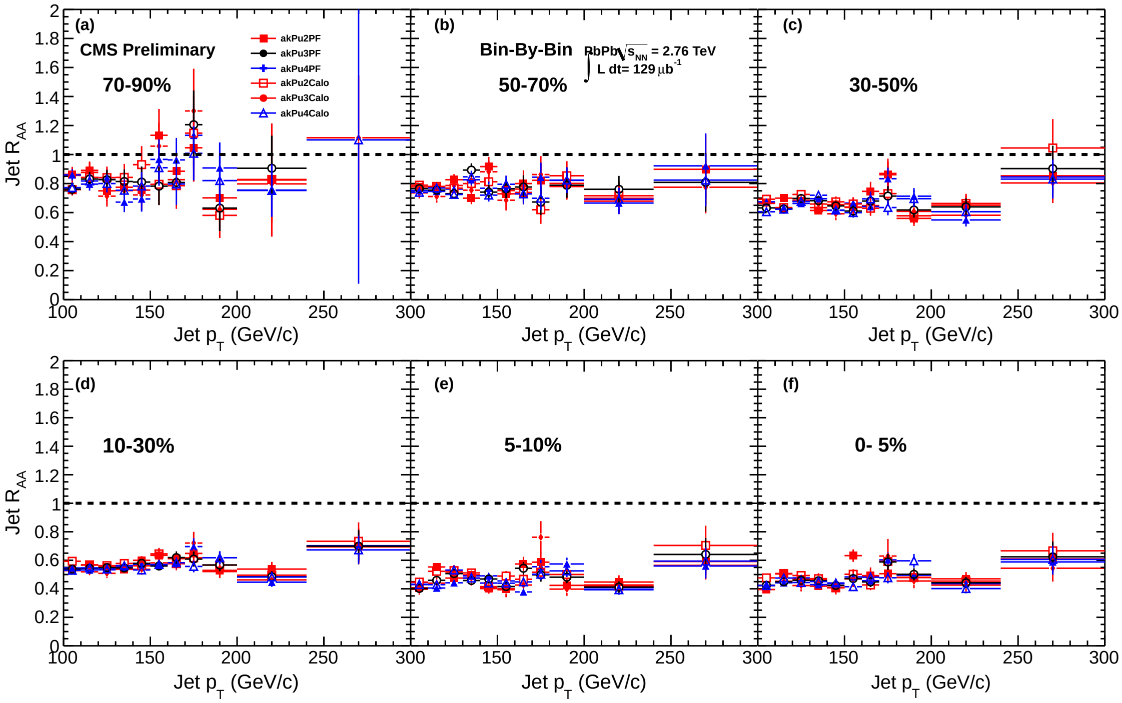

Figure 7.7: R_{AA} in different cone sizes for akPuPF jets and akPuCalo jets with Bin-by-Bin unfolding method.

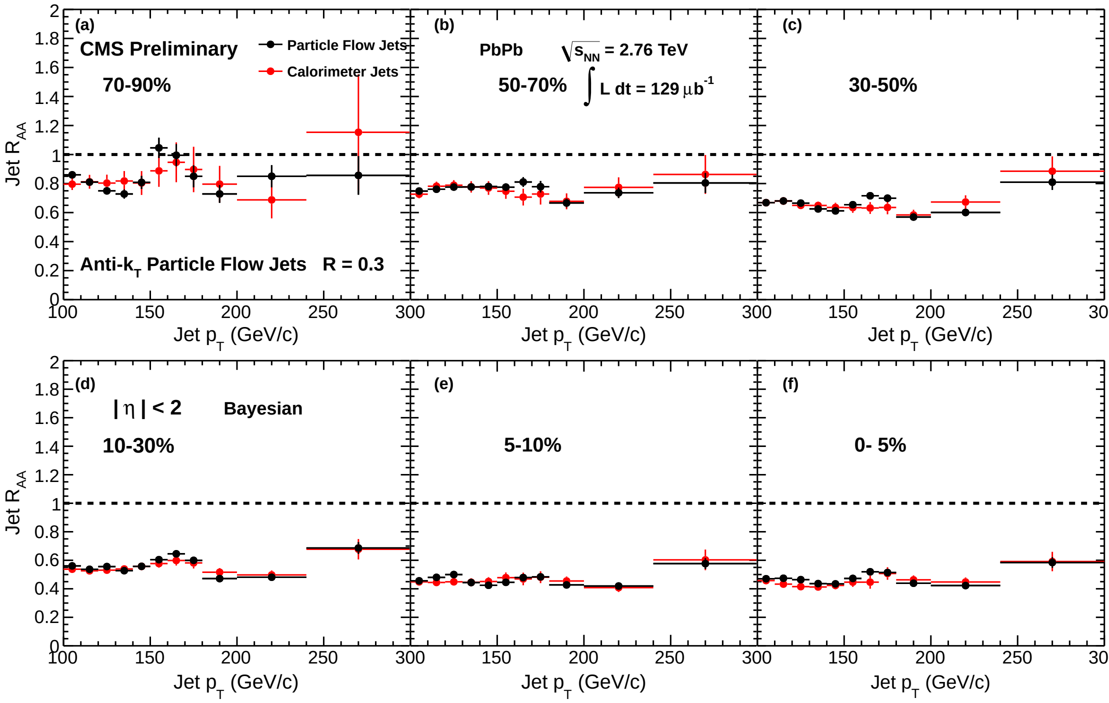

Figure 7.8: R_{AA} for calorimeter and particle flow jets in anti-k_{T} algorithm with Bayesian method in jet cone size 0.3.

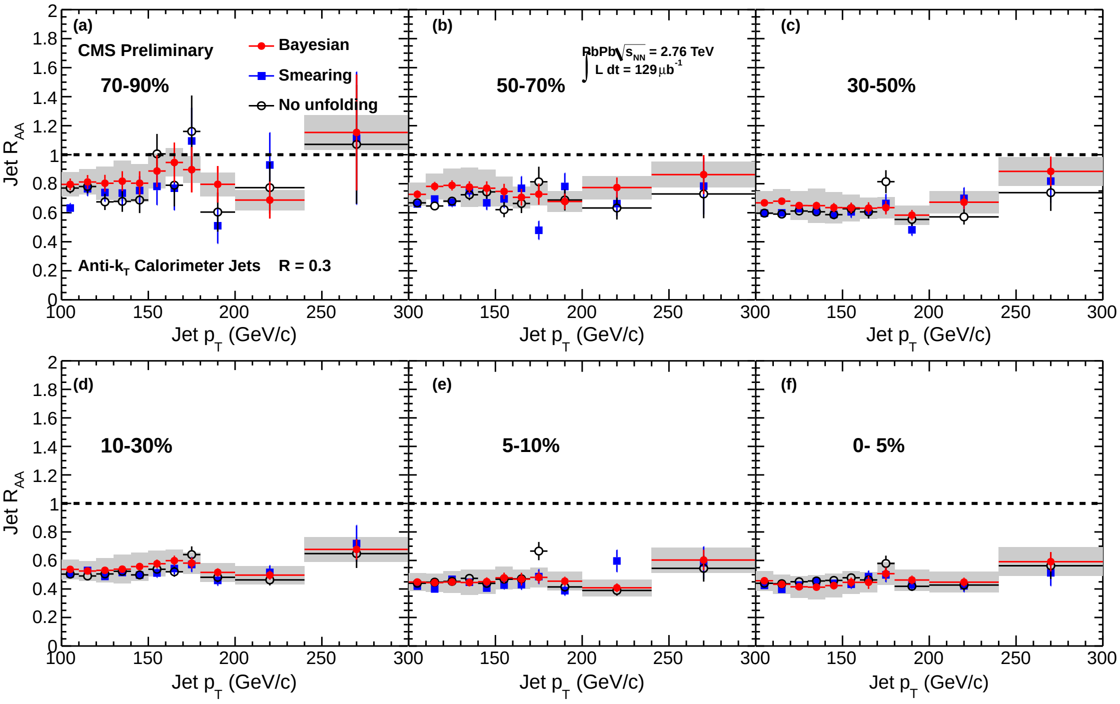

Figure 7.9: $R_{\rm AA}$ for akPu3Calo jets in comparison of Bayesian and smearing method.

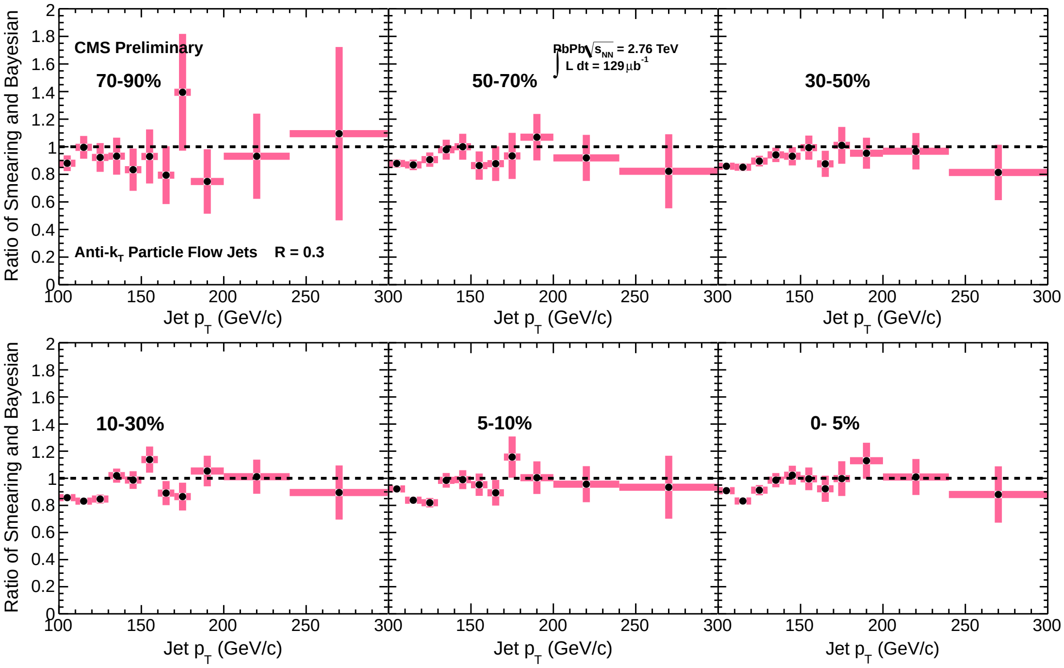

Figure 7.10: Ratio of $R_{\rm AA}$ Smearing and Bayesian methods in different centrality bins.

7.2 Jet R_{AA} vs. N_{part} Result

The behavior of the jet R_{AA} as function of centrality can be seen in Fig. 7.11. Here, the average number of participants indicates the centrality, with the higher number of participants indicating the more central collisions. The jet R_{AA} is shown for the first, high statistics bin of $100 < p_T^{\mathrm{jet}} < 110$ GeV/c with the closed circles. For the open boxes, the jet p_T spectra are averaged 100 to 300 GeV/c and the jet R_{AA} constructed. The average jet R_{AA} is consistent with that of the individual 100 to 110 GeV/c jet R_{AA} bin.

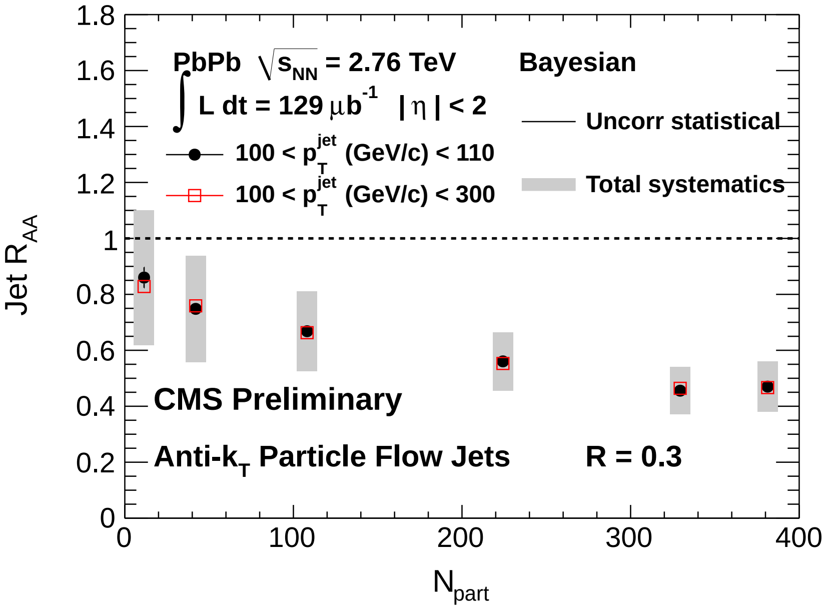

Figure 7.11: R_{AA} vs N_{part} with anti-k_{T} particle flow jets in cone size 0.3 for Bayesian unfolding method in the jet p_T bin of 100 to 110 GeV/c (dark closed circles) and the full p_T range (100 to 300 GeV/c) studied in this analysis (red open boxes) . N_{part} indicates the centrality with higher value indicating more central collisions.

Fig. 7.12 shows the consistent suppression in various techniques of jet R_{AA} as function of centrality. The systematics is only shown for Bayesian unfolding. The results from different correcting techniques are within the systematics.

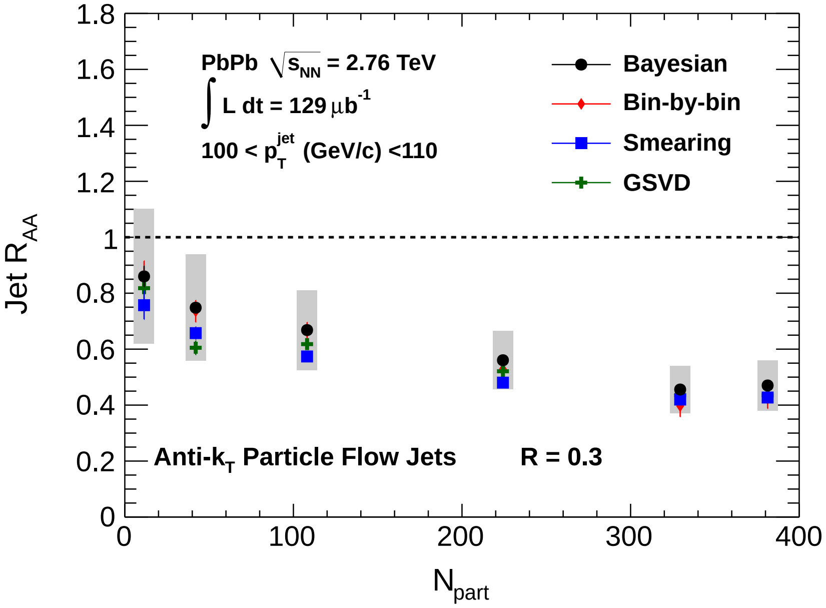

Figure 7.12: R_{AA} vs N_{part} for various techniques in Bayesian unfolding method in the jet p_T bin of 100 to 110 GeV/c .The systematics are only shown for Bayesian unfolding method.

Chapter 8

Conclusion

The CMS detector has been used to study jet production in PbPb collisions at $\sqrt{s_{NN}}$ =2.76 TeV. Utilizing high luminosity collected in 2011, this new result for jet R_{AA} provides a better view of the jet quenching phenomenon. The energy loss in the medium (the Quark Gluon Plasma) produced in heavy-ion collisions is quantified by this quenched jet R_{AA} which is evaluated around 0.5 in central collisions compared to the value of around 0.9 in peripheral collisions. A suppression of high p_T jets is confirmed in central PbPb collisions in comparison to peripheral collisions. The results demonstrate little p_T dependence with all correction methods within uncertainties in the p_T range in this study. Jet R_{AA} results are consistent within systematic and statistical uncertainty for three different unfolding methods, including Bayesian, bin-by-bin and GSVD methods, as well as corrections performed with pp data smearing. R_{AA} of jets reconstructed with various resolution parameters are also compared. Measurements of consistent jet R_{AA} within uncertainties indicate that there is no change in level of suppression due to jet cone size.

Figure 8.1 is a summary diagram of the nuclear modification study in CMS. The jet R_{AA} studied in this thesis is shown as the neon-blue band (closed circles). The other physical objects studied for R_{AA} in CMS collaboration include charged hadron particle (blue-band with open circles), b-quarks (dark orange with open square), Z boson (red band with closed square), W boson (pink band with star), isolated photon (yellow band with closed circles) and b-jets (earth band with closed square). The amount of suppression as a function of p_T is observed to be different in jet R_{AA} than the single charged hadrons. This is mainly due to the fact that jet R_{AA} combines lots of particle information as opposed to single charged hadron p_T and the p_T range specified between two studies are not overlapped, thus the results are not directly comparable. The jet R_{AA} is generally p_T independent compared with the charged hadron particle R_{AA}, which was studied at a lower p_T region. This summary plot provides us a overview of all the new results on the jet quenching phenomenon with various particles, providing further evidences of the energy loss in this dense Quark-Gluon-Plasma phase.

In terms of the future improvement for the analysis based on the jet R_{AA} studied in this thesis, the extension to a lower p_T range will be interesting in that it can be compared with the charged hadron particle R_{AA} result which is studied from 0 to 100 GeV/c. In addition, jets in cone sizes other than 0.2, 0.3 and 0.4 in the lower p_T range can be investigated, since jets with bigger cone size include more soft particles that might be recovered from the quenching effects.

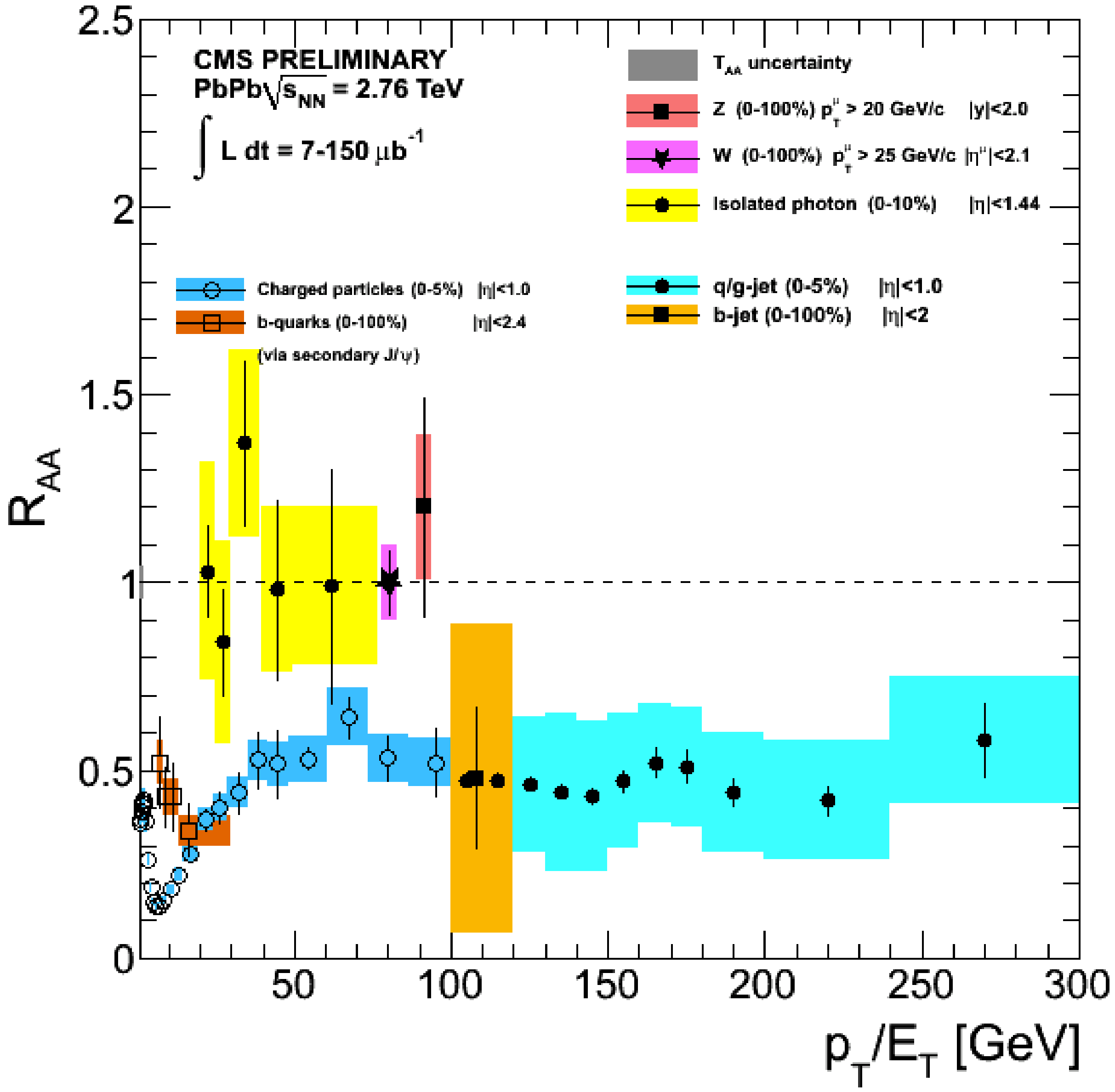

Figure 8.1: R_{AA} "zoo". It is a summary diagram of the R_{AA} study in CMS, with the neon-blue band (closed circle) representing the jet R_{AA} work in this thesis. The overall T_{AA} uncertainties are represented by the small grey band located at unity.

Appendix A

Lorentz Contraction

Einstein's special and general theories of relativity explain that our observation or measurement of things traveling at very high speeds (> 0.1c) is very much dependent on our frame of reference. For instance, at RHIC and other heavy-ion accelerators where nuclei travel at nearly the speed of light, an effect called length contraction or *Lorentz contraction* occurs to the moving nuclei's length when measured in the laboratory's reference frame. This contraction is described by the Lorentz factor $\gamma = 1/\sqrt{1-\beta^2}$, where $\beta = v/c$, velocity divided by the speed of light. The relationship between β, called the speed parameter, and γ is shown in Fig. A.1.

At RHIC, γ can be calculated for accelerated Au nuclei using $E = \gamma\langle m\rangle c^2$, where the beam energy per nucleon (E) is 100 GeV and the average nucleon mass ($\langle m\rangle$) is 0.9390 GeV/c^2. This results in $\gamma = 106.5$. For these relativistic Au nuclei, the measured length L in the laboratory's reference frame is calculated by $L = L_0/\gamma$, where L_0 is the length of the nuclei when at rest. For Au, L_0 is 14 fm, resulting in a length L at RHIC of 0.1315 fm.

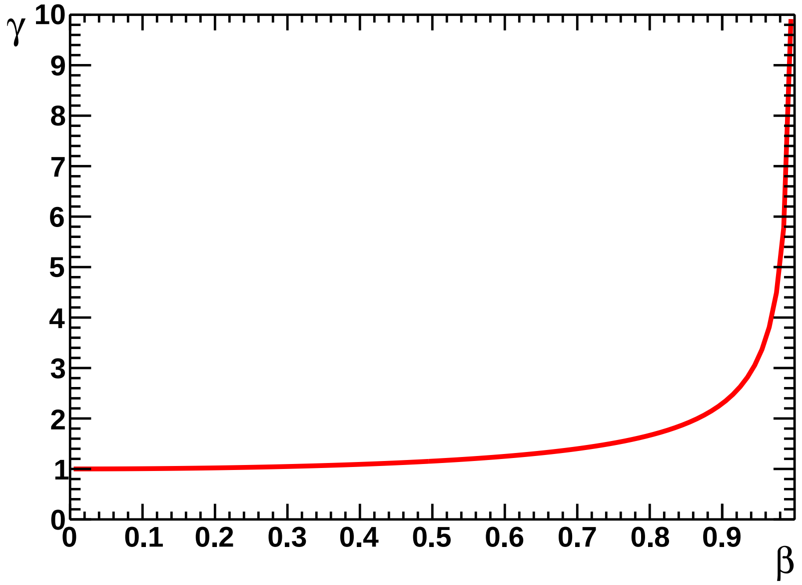

Figure A.1: Relation between Lorentz factor (γ) and the speed parameter (β).

Appendix B

Rapidity and Pseudorapidity

Rapidity (y) is a dimensionless variable that describes the rate at which a particle moves with respect to a reference point along the line of motion. For collider experiments, the chosen reference point is the nominal collision vertex and the line of motion is the direction of the z-axis. Rapidity is mathematically defined as

$$\mathrm{y} = \frac{1}{2}\ln\frac{1+\beta\cos\theta}{1-\beta\cos\theta} = \frac{1}{2}\ln\frac{1+\beta_z}{1-\beta_z}, \tag{1.3}$$

where $\beta = v/c$, velocity divided by the speed of light, and θ is the particle's polar angle with respect to the z-axis. Figure B.1 shows graphically how rapidity is related to β. Note that a particle can have a positive or negative rapidity depending on its direction in velocity compared to the reference point. Although a particle's potential rapidity range is unlimited, in practice its logarithmic dependence leads to small numeric values. For instance, the rapidity of RHIC's 100 GeV Au ion beam is only 5.36 despite traveling at 99.996% the speed of light.

The advantage of using rapidity to describe a particle's rate of motion is that, unlike velocity, rapidity is additive even for velocities approaching the speed of light. In other words

$$\mathrm{y} = \mathrm{y}' + \mathrm{y}_0, \tag{B.1}$$

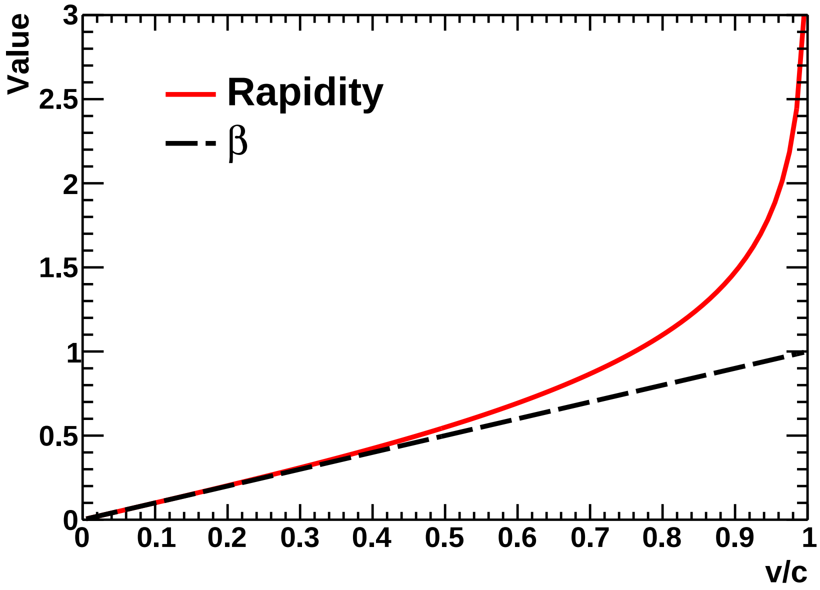

Figure B.1: Relation between rapidity (solid) and β (dashed) as a function of v/c.

where y_0 is the nominal vertex's rapidity, y' the rapidity of the traversing particle, and y their sum. This leads to the consequence that differences in rapidity are invariant. That is to say, the difference in the rapidities of two particles in one frame of reference is the same in all other frames of reference. For instance, using Eq. B.1, the rapidities of two particles A and B are

$$\mathrm{y}_A = \mathrm{y}'_A + \mathrm{y}_0 \tag{B.2a}$$

$$\mathrm{y}_B = \mathrm{y}'_B + \mathrm{y}_0 \tag{B.2b}$$

Subtracting B.2b from B.2a yields

$$\mathrm{y}_A - \mathrm{y}_B = \mathrm{y}'_A - \mathrm{y}'_B \tag{B.3}$$

demonstrating the invariant property of rapidity by the cancelation of y_0, the rapidity of the "observation" reference frame. Hence rapidity differences are invariant.

Despite its usefulness, rapidity has the disadvantage of being difficult to measure experimentally due to the need for particle identification to determine its mass. This is overcome for ultrarelativistic particles ($\beta \approx 1$), making a particle's rapidity only dependent on θ (see middle term of Eq. 1.3). This allows for the introduction of a substitute variable for rapidity called pseudorapidity (η), which is similarly defined as

$$\eta = \frac{1}{2} \ln \frac{1 + \cos\theta}{1 - \cos\theta} \tag{1.4}$$

and is only dependent on the θ angle of the emitted particle. For ultrarelativistic particles, rapidity and η are nearly indistinguishable quantities except at angles near 0° and 180°. For slower particles, differences emerge between the two variables. Figure B.2 compares rapidity and η as a function of θ with various β values used in calculating the rapidity functions.

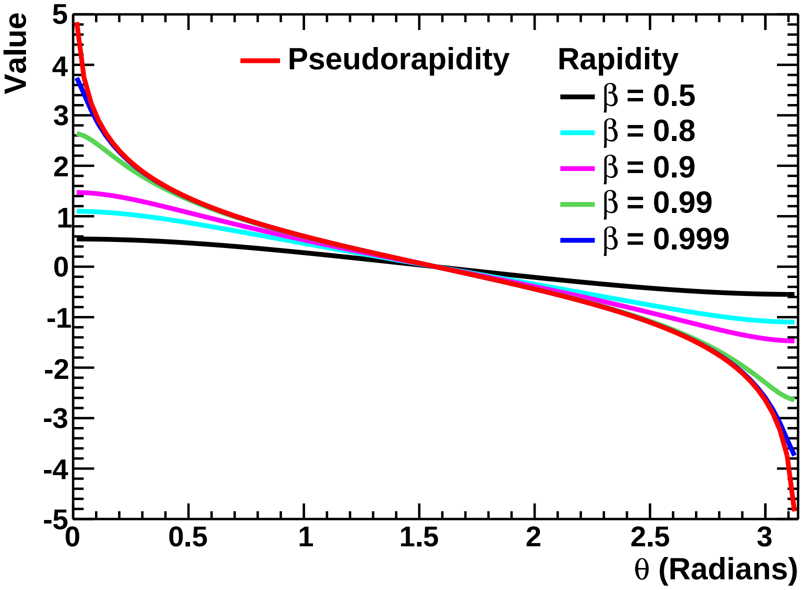

Figure B.2: Relation between rapidity and pseudorapidity as a function of θ. For rapidity, different values of β are used. See legend for details.

Appendix C

Luminosity

Beam luminosity or *instantaneous luminosity* ($\mathscr{L}$) is a parameter used to characterize the effectiveness of colliding beams. Mathematically it is defined as [3]

$$\mathscr{L} = fn\frac{N_1 N_2}{4\pi\sigma_x\sigma_y} = f'\frac{N_1 N_2}{4\pi\sigma_x\sigma_y}, \tag{C.1}$$

where N_1 and N_2 are the number of particles in each beam bunch, σ_x and σ_y are the x and y transverse bunch profiles, respectively, n is the number of bunches in either beam, and f is the beam's revolution frequency. The product of f and n can be combined into f', *i.e.* $f' = fn$, which is simply the bunch crossing frequency. This luminosity definition assumes each beam has the same number of bunches, those bunches have the same transverse profile, the profiles are independent of position along the bunch, and the particle distributions are not altered durring bunch crossings. Luminosity is generally expressed in units of cm^{-2} s^{-1} or b^{-1} s^{-1}, where a barn (b) $= 10^{-24}$ cm^2. After an accelerator's buckets are fully populated with bunches, the luminosity can still be increased by either increasing the number of particles in each bunch or decreasing the bunch's transverse profile.

Of particular importance to a collider Run is the *integrated luminosity* ($\mathscr{L}_i$) or *delivered luminosity* defined as the integral of the instantaneous luminosity over time, *i.e.* $\mathscr{L}_i = \int \mathscr{L}\ dt$. It is generally expressed in units of cm^{-2} or b^{-1}. In addition to the previously mentioned beam improvements, the integrated luminosity can be improved by increasing the beam's lifetime via decreasing beam loss or beam degradation, as well as decreasing the turn around time between stores.

In practice, it is impossible for an experiment to archive to disk all of the delivered luminosity. The amount that is archived is called the *collected* or *recorded luminosity* ($\mathscr{L}_r$), and is defined for min-bias collisions as

$$\mathscr{L}_r = \frac{N_{MB}}{\sigma_{NN}}, \tag{C.2}$$

where N_{MB} is the number of min-bias events recorded and σ_{NN} is the inelastic nucleon-nucleon cross section, which depends on colliding species and collision energy. Taking into account the min-bias trigger efficiency (ϵ_{MB}) yields

$$\mathscr{L}_r' = \frac{N_{MB}}{\epsilon_{MB}\sigma_{NN}}, \tag{C.3}$$

which can be an essential calculation for certain analyses such as those determining a particle's invariant yield. For $\sqrt{s_{NN}} = 200$ GeV Au+Au collisions $\sigma_{NN} = 6.85$ b and the PHENIX min-bias trigger efficiency is $\epsilon_{MB} \approx 93\%$. Aside from the previously mentioned improvements, increasing an experiments recorded luminosity can be done by decreasing the bunch's longitudinal profile so more collisions occur in the experiments acceptable vertex region. It can also be accomplished by improving the trigger efficiency through experimental upgrades, or decreasing DAQ dead time, *i.e.* the time the DAQ isn't recording events because of a bottleneck in the system.

Another luminosity term called *sampled luminosity* is used when the trigger rate is larger than the DAQ's maximum recording rate. In these instances the DAQ triggers are pre-scaled to only record a subset or sample of the events that pass the trigger requirements.

Appendix D

Unfolding Techniques

The linear least square (LLS) with Phillips–Tikhonov regularization or "SVD" unfolding, and the Richardson–Lucy or "Bayesian" unfolding are used to determine the true jet energy spectrum with full covariance matrices, which is generally described as an inverse or ill-posed problem. For jet spectra, the folding process is the Fredholm equation

$$\frac{dN}{dp_T^{\mathrm{rec}}} = \int dp_T \, P(p_T^{\mathrm{rec}}|p_T) \frac{dN}{dp_T}, \tag{D.1}$$

where $p_T \equiv p_T^{\mathrm{gen}}$ is understood as the true or perfect detector (hadronized) jet energy. With finite histogram binning, this can be understood as the matrix inversion to solve

$$\mathbf{A}\mathbf{x} = \mathbf{b}, \tag{D.2}$$

with the correspondence

$$\begin{aligned} \frac{dN}{dp_T^{\mathrm{rec}}} &\leftrightarrow \mathbf{b} \\ P(p_T^{\mathrm{rec}}|p_T) &\leftrightarrow \mathbf{A} \\ \frac{dN}{dp_T} &\leftrightarrow \mathbf{x}. \end{aligned} \tag{D.3}$$

For the (additive) LLS method, an "initial guess" x_{ini} is used to scale the problem such that the unfolding does not have to exhaust its total degrees of freedom (DOF) to purely reproduce the steeply falling spectrum shape. The scaled form of (D.2) is

$$\hat{\mathbf{A}}\hat{\mathbf{x}} = \mathbf{b}, \tag{D.4}$$

where the multiplicative scaling is shifted from $\hat{\mathbf{x}}$ towards $\hat{\mathbf{A}}$ and

$$\begin{aligned} \hat{x}_i &= x_i / x_{\mathrm{ini},i} \\ \hat{a}_{ij} &= a_{ij} x_{\mathrm{ini},i} \end{aligned} \tag{D.5}$$

with the intent of having $\hat{x}_i \approx 1$ (at least within one or two orders of magnitude).

Both methods are regularized in the sense that structures in the jet spectrum unmeasurable due to finite detector resolution are removed by constraints imposed either by iterative reblurring, or applying a continuity constraint.

Apart from the implementation found ROOUNFOLD, the standard Richardson-Lucy method was implemented for this thesis. No extra reblurring is applied, as this is unphysical and usually indicates resolution mismatch between Monte Carlo detector description and the measurement (that should not be masked via unfolding regularization).

The standard method to perform Phillips–Tikhonov regularization (without resorting to approximative tricks to invert the otherwise singular regularization matrix, such as with GURU and ROOUNFOLD) is the generalized singular value decomposition (GSVD). This was implemented using the standard linear algebra subprogram libraries BLAS and LAPACK. Due to the scarcity of notes within the HEP, a brief summary as follows.

The (real valued) GSVD of a matrix pair GSVD($\hat{\mathbf{A}}, \mathbf{L}$), with $\hat{\mathbf{A}} \in \mathbb{R}^{m \times n}$, $\mathbf{L} \in \mathbb{R}^{p \times n}$, and $p \leq n \leq m$, simultaneously decomposes both matrices (using the LAPACK convention) into

$$\begin{aligned} \hat{\mathbf{A}} &= \mathbf{U}\mathbf{\Sigma}_1 \begin{pmatrix} 0 & \mathbf{R} \end{pmatrix} \mathbf{Q}^T \\ \mathbf{L} &= \mathbf{V}\mathbf{\Sigma}_2 \begin{pmatrix} 0 & \mathbf{R} \end{pmatrix} \mathbf{Q}^T, \end{aligned} \tag{D.6}$$

with $\mathbf{U} \in \mathbb{R}^{m \times m}$, $\mathbf{V} \in \mathbb{R}^{p \times p}$, $\mathbf{Q} \in \mathbb{R}^{n \times n}$ all being orthogonal matrices, and $\mathbf{R}$ an upper triangular matrix. The "diagonal-plus-zero-padding" matrices $\mathbf{\Sigma}_1$, $\mathbf{\Sigma}_2$ contain a pair of singular values (α_i), (β_i), and because of the correspondence to SVD($\hat{\mathbf{A}}\mathbf{L}^{-1}$), the singular values of $\hat{\mathbf{A}}\mathbf{L}^{-1}$ are $\gamma_i = \alpha_i/\beta_i$. The singular values for the solution with respect to $\hat{\mathbf{x}}$ (as opposed to $\mathbf{L}\hat{\mathbf{x}}$ with GURU) scale with the function

$$f_i(\tau) = \frac{\gamma_i^2}{\gamma_i^2 + \tau} \tag{D.7}$$

with f also called the Tikhonov filter. And as a shorthand, the following are defined:

$$\begin{aligned} \mathbf{F} &= \operatorname{diag}(f_i(\tau)) \\ \mathbf{\Sigma}'^{-1} &= \mathbf{F}{\mathbf{\Sigma}_1}^{-1}. \end{aligned} \tag{D.8}$$

A comparison with the SVD solution (for invertible regularization matrix) gives as solutions to the unfolding

$$\begin{aligned}\hat{\mathbf{x}} &= \mathbf{X}\boldsymbol{\Sigma}'^{-1}\mathbf{U}^T\mathbf{b} \\ \operatorname{Cov}\hat{\mathbf{x}} &= \mathbf{X}\boldsymbol{\Sigma}'^{-1}(\boldsymbol{\Sigma}'^{-1})^T\mathbf{X}^T,\end{aligned} \tag{D.9}$$

where $\hat{\mathbf{x}}$ is understood as the unfolded mean and $\operatorname{Cov}\hat{\mathbf{x}}$ denotes its covariance matrix. Here, $\mathbf{X}$ is a combined scaling–rotation matrix (and with proper book keeping for the rank deficient cases)

$$\mathbf{X} = \mathbf{Q}\begin{pmatrix}\mathbf{I} & 0 \\ 0 & \mathbf{R}^{-1}\end{pmatrix}, \tag{D.10}$$

The quality of the unfolding is characterized by

$$\begin{aligned}\mathrm{DOF} &= m - (n-p) - \operatorname{tr}\mathbf{F} \\ \|\mathbf{A}\hat{\mathbf{x}} - \mathbf{b}\| &= (\mathbf{I} - \mathbf{F})\mathbf{U}^T\mathbf{b} \\ \|\mathbf{L}\hat{\mathbf{x}}\| &= \boldsymbol{\Sigma}'^{-1}\mathbf{U}^T\mathbf{b},\end{aligned} \tag{D.11}$$

where DOF is the effective degrees of freedom. Two model-independent estimations of the optimum τ are readily available from GSVD. The optimum τ given by the L-curve criterion locates the "kink" of the curve $(\log\|\mathbf{A}\hat{\mathbf{x}} - \mathbf{b}\|, \log\|\mathbf{L}\hat{\mathbf{x}}\|)$, or rigorously defined as the locally maximum (convex) curvature. The entire curve, however, can have multiple such maxima. Since the first concave turn indicates accelerated divergence, the "kink" that is useful is usually the largest in term of RSS. For the optimum τ in term of the generalized cross validation (GCV) or leave-one-out cross-validation (LOOCV) can be shown to minimize $\|\mathbf{A}\hat{\mathbf{x}} - \mathbf{b}\|^2/\mathrm{DOF}^2$.

The error propagated R_{AA}, which is the ratio of two random variates with known mean and covariance matrix can be derived by Taylor expansion of statistical moments

$$\begin{aligned} \mathrm{E}\left(\frac{X_i}{Y_i}\right) &= \frac{\mathrm{E}(X_i)}{\mathrm{E}(Y_i)} + \frac{\mathrm{E}(X_i)\mathrm{Var}(Y_i)}{\mathrm{E}^3(Y_i)} \\ \mathrm{Cov}\left(\frac{X_i}{Y_i}, \frac{X_j}{Y_j}\right) &= \frac{\mathrm{Cov}(X_i, X_j)}{\mathrm{E}(Y_i)\mathrm{E}(Y_j)} + \frac{\mathrm{E}(X_i)\mathrm{E}(X_j)\mathrm{Cov}(Y_i, Y_j)}{[\mathrm{E}(Y_i)\mathrm{E}(Y_j)]^2}, \end{aligned} \tag{D.12}$$

where E and Cov are the mean and covariance of the random variates, and $\mathrm{Var}(X_i) \equiv \mathrm{Cov}(X_i, X_i)$. X_i and Y_i are bin entries of the uncorrelated cross section bins in the numerator and denominator, respectively.

One particular problem with plotting fully propagated covariance is the presentation of the size of the correlated uncertainty. The approach found to reproduce realistic error sizes when comparing unfolding results with full covariance propagation and "diagonal" approaches (such as raw spectra ratio, "bin-by-bin" methods), is to show as the total (correlated + uncorrelated) error

$$\sigma_{\mathrm{tot}} = \left[\mathrm{Var}(X_i) \sum_j \rho_{ij}^2\right]^{1/2}, \tag{D.13}$$

with $\rho_{ij} = \mathrm{Cov}(X_i, X_j)/\sqrt{\mathrm{Var}(X_i)\mathrm{Var}(X_j)}$ being the correlation coefficients. However, it should be cautioned that while this form of visualization can at least give the visual impression of "correlatedness", the reduction of a full covariance matrix to a "diagonal" representation cannot be done without loss of information and should never be interpreted e.g. by simple combinations with other errors.

Appendix E

Jet Quality Check

Basic jet kinematics were checked in MC and data and the ratio between them has been calculated to make a comparison for anti-k_{T} particle flow jets with pile-up subtraction (abbreviated as ak3PuPF jets). MC samples were combined from PYTHIA+HYDJET (version 1.8) Drum with $\hat{p}_{\mathrm{T}} > 50$, 80, 120, 170 , 200, 250 GeV/c. The combined sample is re-weighted by centrality, primary vertex and cross section. The luminosity of each MC sample varies according to the number of generated events. In order to gain a proper jet distribution from different $\hat{p}_{\mathrm{T}}$ samples, each $\hat{p}_{\mathrm{T}}$ sample is normalized by its luminosity ($N_{\mathrm{events}}/\sigma$), where σ is the cross section. With this re-weighting of cross section, different $\hat{p}_{\mathrm{T}}$ samples that produce overlapping jets are not double counted. The offline selection for both MC and data is to require reconstructed jets with $|\eta| < 2$, $p_T > 100$ GeV/c, the primary vertex cut of 15 cm and the maximum track p_T / jet $p_T > 0.01$. Figures E.1 to E.3 are the jet η, p_T, ϕ distributions, with data represented by the closed points, and MC by the striped distribution. The distributions plot the frequency of jets observed in each of the variables. From these plots, no outstanding outlier events were observed. More jet quality checks are shown from Fig. E.4 to E.14.

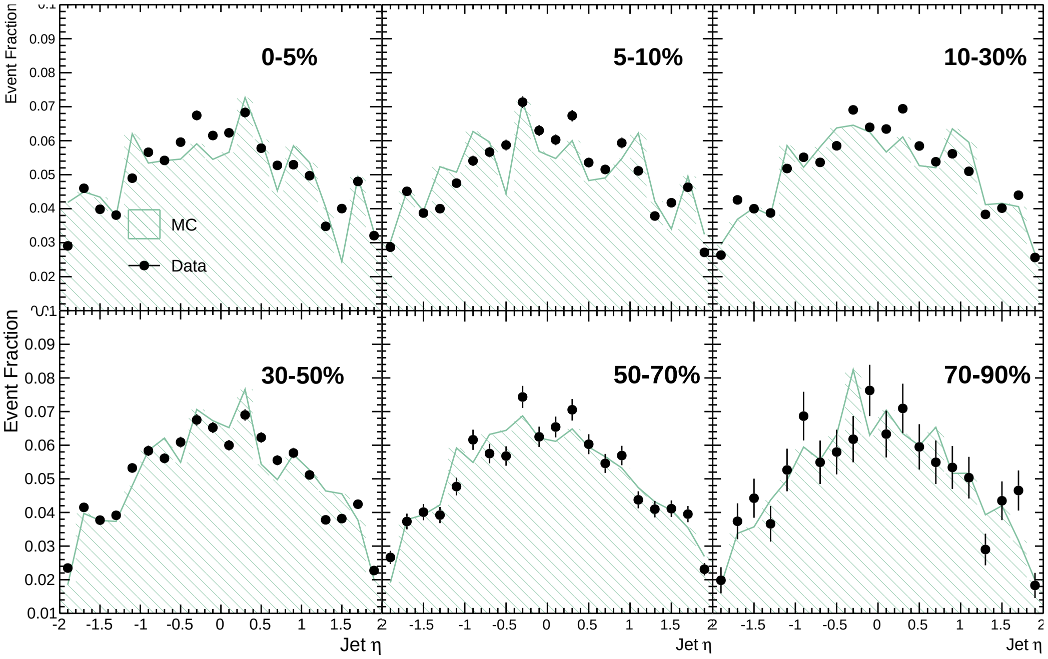

Figure E.1: Jet η distribution comparison of data and MC sample.

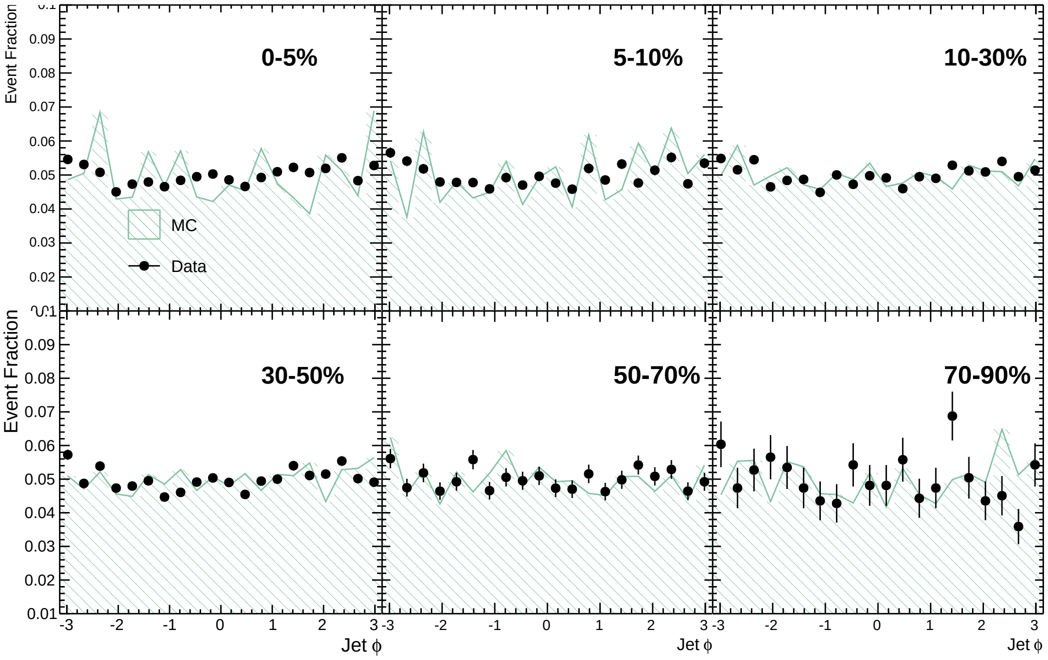

Figure E.2: Jet ϕ distribution comparison of data and MC sample.

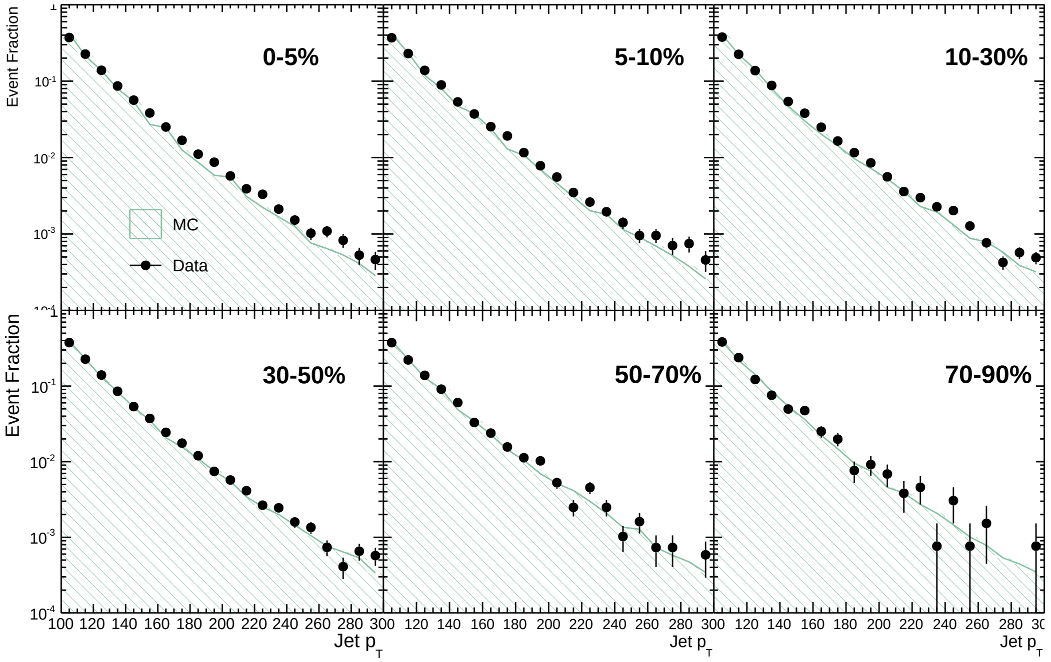

Figure E.3: Jet p_T distribution comparison of data and MC sample.

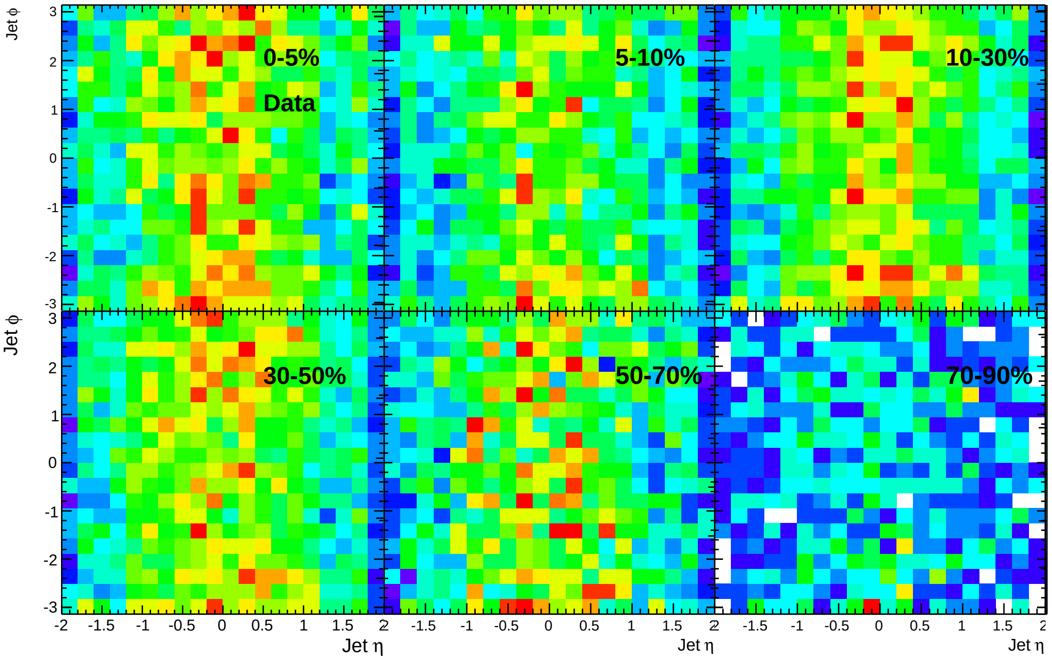

Figure E.4: Jet η-ϕ distribution of data sample.

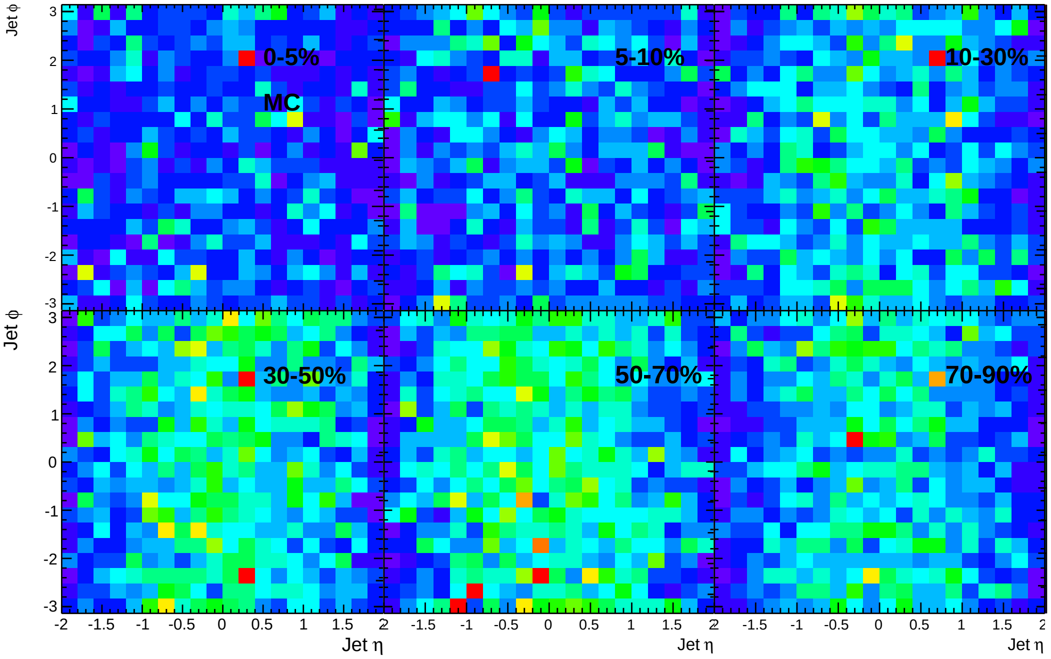

Figure E.5: Jet η-ϕ distribution of MC sample.

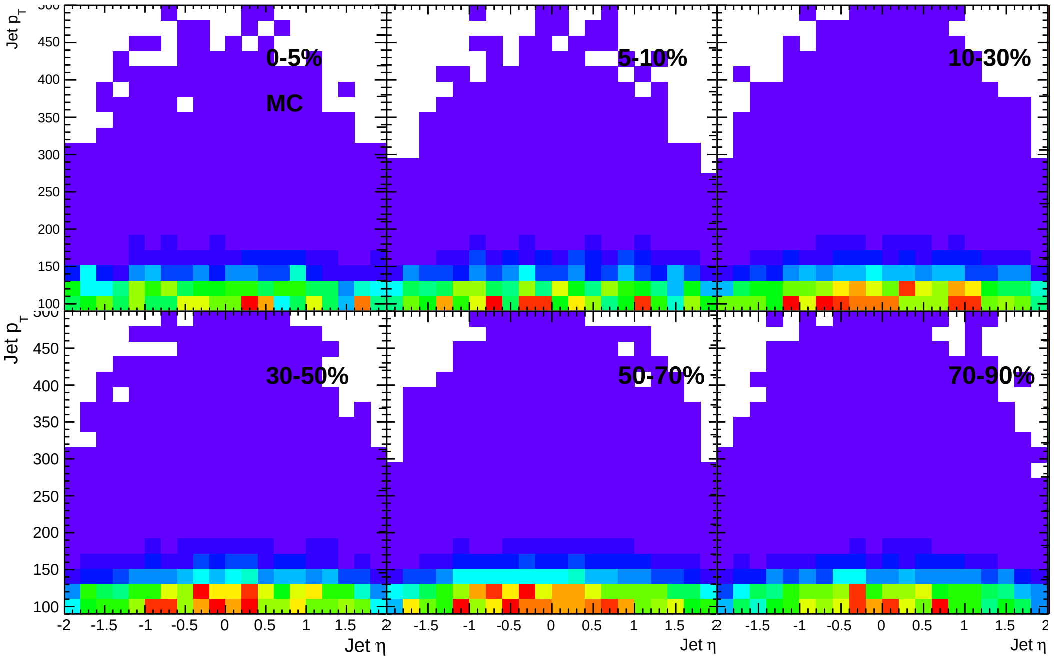

Figure E.6: Jet η-p_T distribution of data sample.

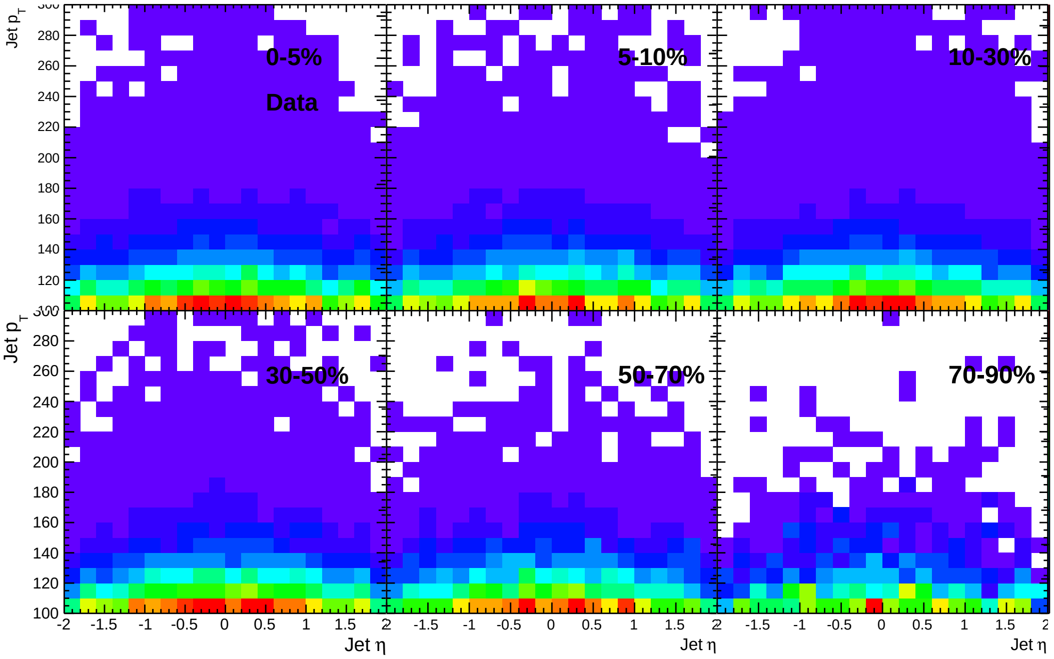

Figure E.7: Jet η-p_T distribution of MC sample.

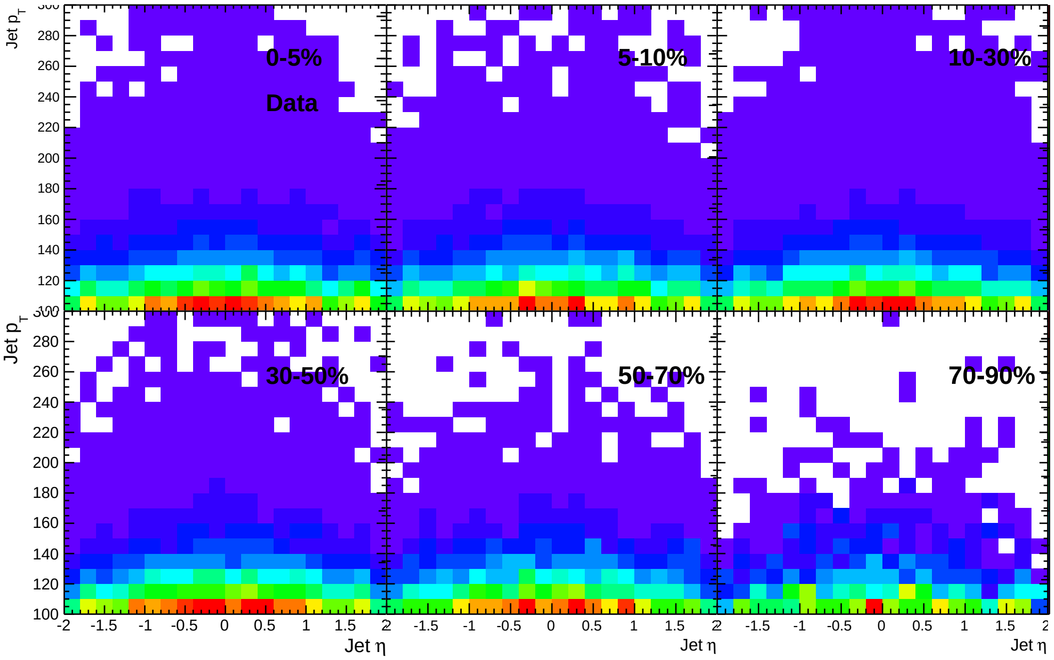

Figure E.8: Jet η-p_T distribution of MC sample.

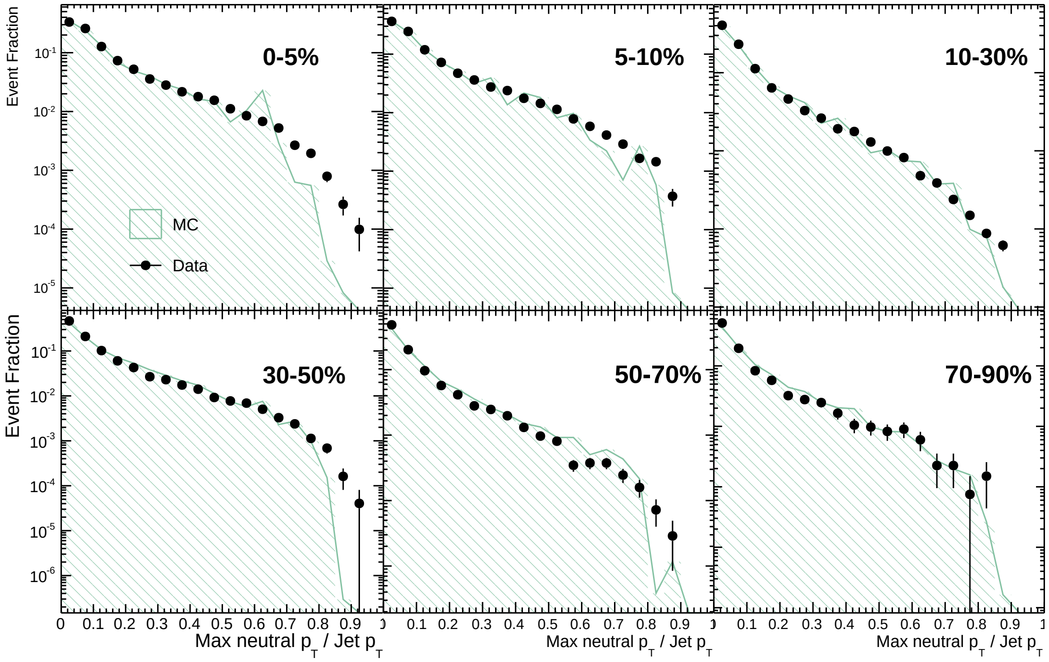

Figure E.9: JetID neutralMax with ak3PuPF jets.

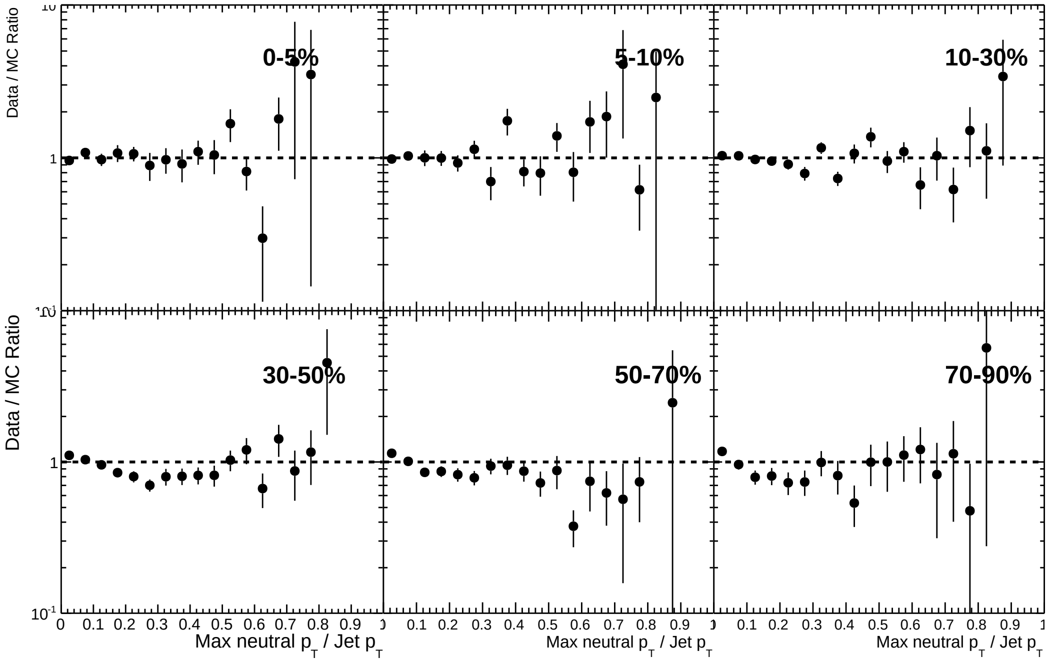

Figure E.10: JetID neutralMax data / MC ratio with ak3PuPF jets.

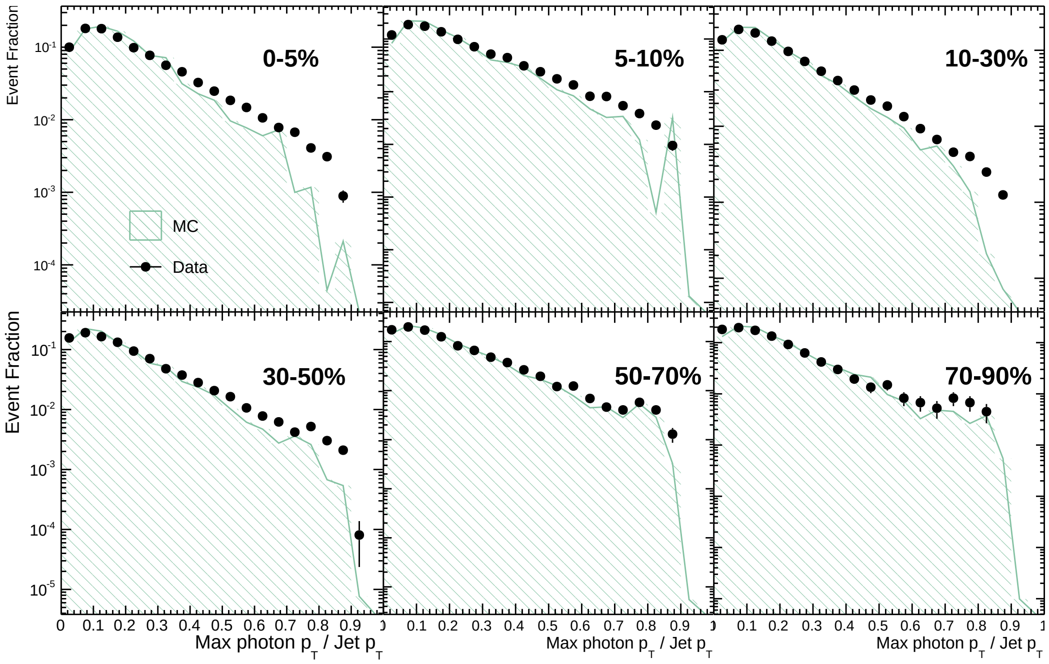

Figure E.11: JetID photonMax ak3PuPF

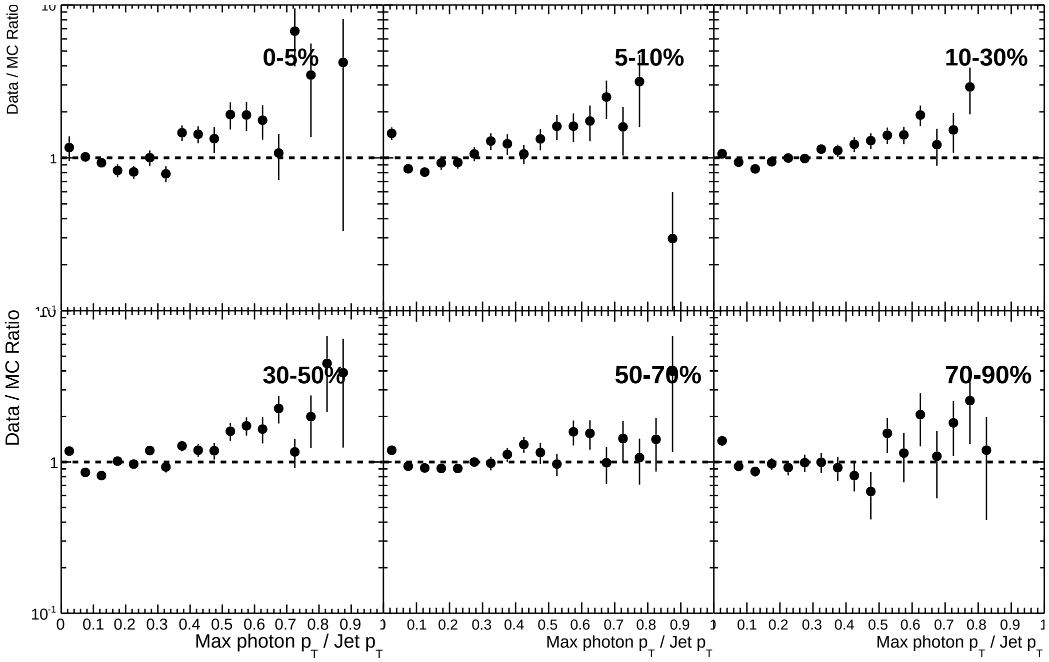

Figure E.12: JetID photonMax data / MC ratio with ak3PuPF jets.

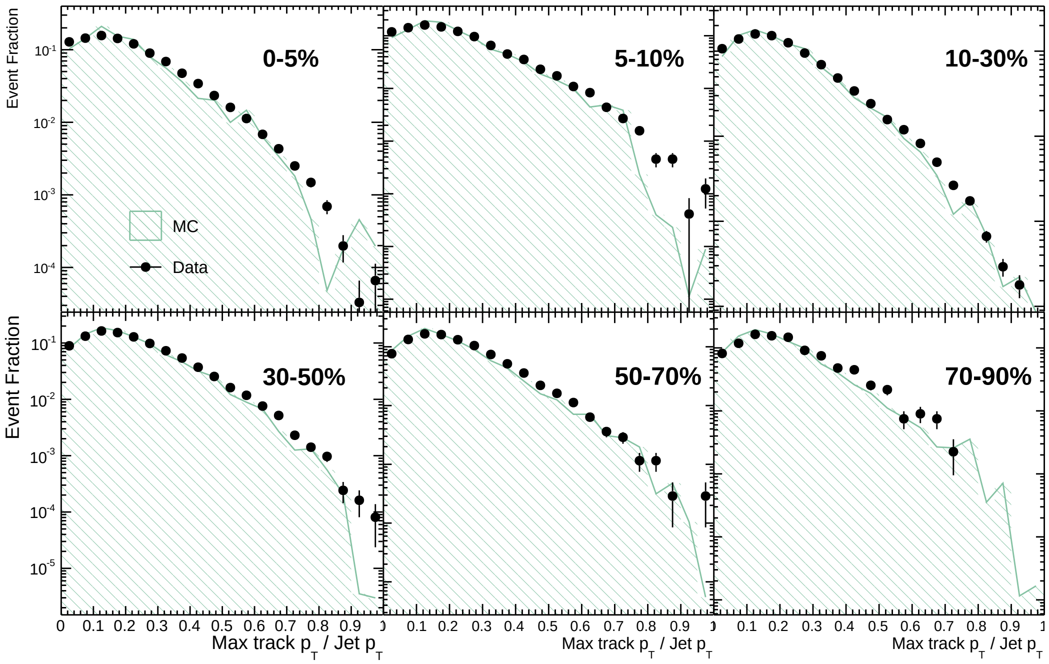

Figure E.13: JetID trackMax data / MC ratio with ak3PuPF jets.

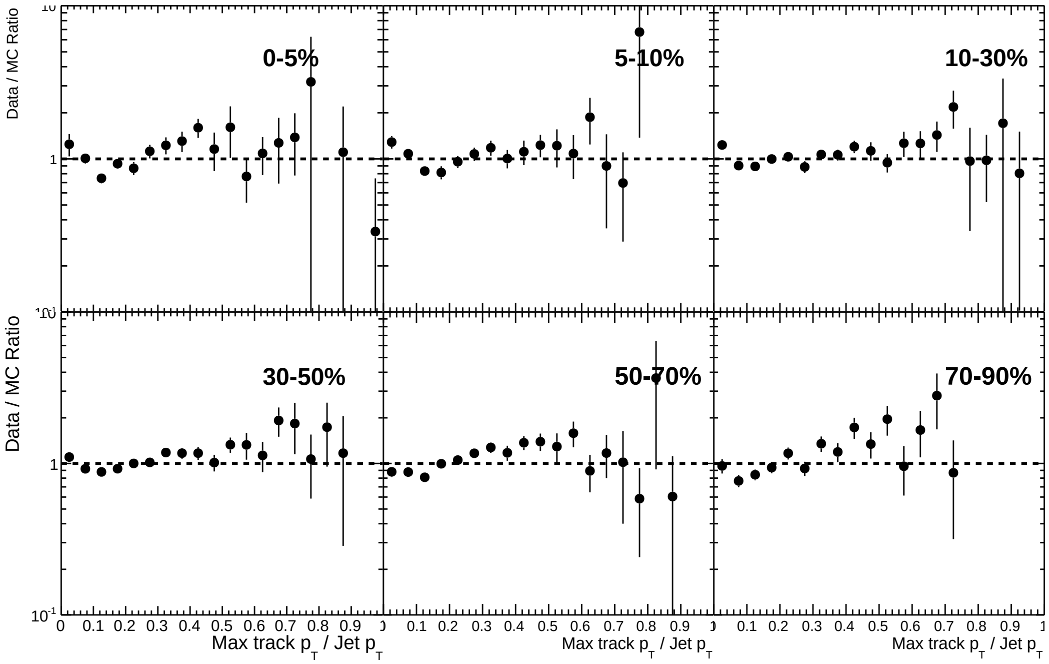

Figure E.14: JetID trackMax data / MC ratio with ak3PuPF jets.

Bibliography

[1] STAR Collaboration. Evidence from d+au measurements for final-state suppression of high p_t hadrons in au+au collisions at rhic. *Phys.Rev.Lett.*, 91(072304), 2003.

[2] R.A. Dunlap. *An introduction to the physics of nuclei and particles*. Brooks/Cole – Thomson Learning Inc., 2003.

[3] K. Nakamura and Particle Data Group. Review of particle physics. *J. Phys. G*, 37:075021, 2010.

[4] The Particle Adventure: The Fundamentals of Matter and Force, `http://www.particleadventure.org`.

[5] R.P. Feynman. Very high-energy collisions of hadrons. *Phys. Rev. Lett.*, 23:1415, 1969.

[6] R.P. Feynman. Structure of the proton. *Science*, 183:601, 1974.

[7] R.G. Roberts. *The structure of the proton*. Cambridge University Press, 1990.

[8] R. Kikuchi et al. Production of neutral pions from electron-proton collisions. *Il Nuovo Cimento*, 4:1178, 1966.

[9] R. Bindel. *Elliptic flow measured with the PHOBOS spectrometer at RHIC*. PhD thesis, University of Maryland, College Park, MD, 2008.

[10] B. Jacak. The future of quark matter at RHIC. Quark Matter 2006, Shanghai, China, 2006, `http://www.sinap.ac.cn/qm2006/`.

[11] R. Bindel. Fluid-like properties of hot and dense nuclear matter. Analytical, Nuclear and Environmental Chemistry PhD Exit Seminar, University of Maryland, College Park, MD, 2007.

[12] A. Bickley. Quarkonium production in PHENIX. Hard Probes 2006, Pacific Grove, CA, 2006, `http://hp2006.lbl.gov/`.

[13] M. Harrison, T. Ludlam, and S. Ozaki. RHIC project overview. *Nucl. Inst. and Meth. A*, 499:235, 2003.

[14] H. Hahn et al. The RHIC design overview. *Nucl. Inst. and Meth. A*, 499:245, 2003.

[15] L. Evans and P. Bryant. LHC machine. *J. Inst.*, 3:S08001, 2008.

[16] F. Karsch. Lattice QCD at high temperature and density. *Lect. Notes Phys.*, 583:209, 2002.

[17] K. Adcox et al. Formation of dense partonic matter in relativistic nucleus-nucleus collisions at RHIC: Experimental evaluation by the PHENIX collaboration. *Nucl. Phys. A*, 757:184, 2005.

[18] D.R. Williams. Sun fact sheet (NASA). 2004, `http://nssdc.gsfc.nasa.gov/planetary/factsheet/sunfact.html`.

[19] A. Bickley. *Charged antiparticle to particle ratios near midrapidity in d+Au and p+p collisions at* $\sqrt{s_{NN}} = 200$ *GeV*. PhD thesis, University of Maryland, College Park, MD, 2004.

[20] J. D. Bjorken. Energy loss of energetic partons in qgp:possible extinction of high p_t jets in hadron-hadron collisions. 1982. FERMILAB-PUB-82-059-THY.

[21] Jorge Casalderrey-Solana and Carlos A. Salgado. Introductory lectures on jet quenching in heavy ion collisions. *Acta Phys. Polon.*, B38:3731–3794, 2007.

[22] Jorge Casalderrey-Solana, J Guilherme Milhano, and Paloma Quiroga-Arias. Out of medium fragmentation from long-lived jet showers. *Physics Letters B*, 710(1):175–181, 2012.

[23] Steffen A. Bass, Charles Gale, Abhijit Majumder, Chiho Nonaka, Guang-You Qin, et al. Systematic Comparison of Jet Energy-Loss Schemes in a realistic hydrodynamic medium. *Phys.Rev.*, C79:024901, 2009. 15 pages, 12 figures, revtex.

[24] Serguei Chatrchyan et al. Observation and studies of jet quenching in PbPb collisions at nucleon-nucleon center-of-mass energy = 2.76 TeV. *Phys. Rev. C*, 84:024906, 2011.

[25] Serguei Chatrchyan et al. Jet momentum dependence of jet quenching in PbPb collisions at sqrt(sNN)=2.76 TeV. *Phys.Lett.*, B712:176–197, 2012.

[26] Michael L. Miller, Klaus Reygers, Stephen J. Sanders, and Peter Steinberg. Glauber modeling in high energy nuclear collisions. *Ann. Rev. Nucl. Part. Sci.*, 57:205–243, 2007.

[27] A. Majumder. A Comparative study of Jet-quenching Schemes. *J.Phys.G*, G34:S377–388, 2007.

[28] Oliver Sim Brüning, Paul Collier, P Lebrun, Stephen Myers, Ranko Ostojic, John Poole, and Paul Proudlock. *LHC Design Report*. LHC Design Report, Geneva, 2004.

[29] Serguei Chatrchyan et al. Studies of jet quenching using isolated-photon+jet correlations in PbPb and pp collisions at sqrt(s[NN]) = 2.76 TeV. 2012.

[30] CMS Collaboration. Dijet energy balance studies in pbpb collisions at 2.76 tev. *Phys. Lett. B*, 712:176–197, 2012.

[31] CMS Heavy Ion. Energy loss in high transverse momentum dijets in pbpb collisions at nucleon-nucleon center-of-mass energy = 2.76 tev. CMS Analysis Note AN-11-478, CMS, 2012.

[32] M.L. Miller, K. Reygers, S.J. Sanders, and P. Steinberg. Glauber modeling in high energy nuclear collisions. *Ann. Rev. Nucl. Part. Sci.*, 57:205, 2007.

[33] Raimond Snellings. Elliptic flow: a brief review. *New Journal of Physics*, 13(5):055008, 2011.

[34] Ivan Amos Cali, Yongsun Kim, Pelin Kurt, Yue Shi Lai, Yen-Jie Lee, Ying Lu, Frank Ma, Pawan Kumar Netrakanti, Matthew Nguyen, Jorge Robles, Dragos Velicanu, Yetkin Yilmaz, Andre Yoon, Dipanwita Dutta, Christof Roland, Gunther Roland, Sevil Salur, George Stephans, and Marguerite Tonjes. Gamma-jet correlation studies in pbpb collisions. CMS Analysis Note AN-11-435, CMS, 2012.

[35] Christof Roland, Frank Ma, Andre Yoon, Matthew Nguyen, Yetkin Yilmaz, Edward Wenger, Gunther Roland, Marguerite Belt Tonjes, Yen-Jie Lee, Sevil Salur, Yongsun Kim. Measurement of jet fragmentation functions in central pbpb collisions at 2.76 tev. CMS Analysis Note AN-11-121, CMS, 2012.

[36] Torbjorn Sjöstrand, Stephen Mrenna, and Peter Skands. PYTHIA 6.4 Physics and Manual. *JHEP*, 05:026, 2006.

[37] I. P. Lokhtin and A. M. Snigirev. A model of jet quenching in ultrarelativistic heavy ion collisions and high-p_T hadron spectra at RHIC. *Eur. Phys. J.*, C45:211, 2006.

[38] S. Agostinelli et al. GEANT4: A Simulation toolkit. *Nucl. Instrum. Meth.*, A506:250–303, 2003.

[39] Urs Achim Wiedemann. Jet quenching in heavy ion collisions. *arXiv:0908.2306*, 2009.

[40] Matteo Cacciari, Gavin P. Salam, and Gregory Soyez. FastJet user manual. 2011. * Temporary entry *.

[41] Matteo Cacciari, Gavin P. Salam, and Gregory Soyez. The Catchment Area of Jets. *JHEP*, 0804:005, 2008.

[42] Olga Kodolova, I. Vardanian, A. Nikitenko, and A. Oulianov. The performance of the jet identification and reconstruction in heavy ions collisions with CMS detector. *Eur. Phys. J.*, C50:117, 2007.

[43] Measurement of the relative jet energy scale in cms with pp collisions at sqrt(s) = 7 tev. CMS Analysis Note PAS PFT-10-002, CMS, 2010.

[44] Commissioning of the particle-flow reconstruction in minimum-bias and jet events from pp collisions at 7 tev. *CMS-PAS-PFT-10-002*, 2010.

[45] CMS Collaboration. Measurement of the relative jet energy scale in cms with pp collisions at sqrt(s) = 7 tev. CMS Analysis Note AN-10-139, CMS, 2010.

[46] Determination of the jet energy scale in cms with pp collisions at $\sqrt{s} = 7$ tev. *CMS-PAS-JME-10-010*, 2010.

[47] Andrey Nikolayevich Tychonoff. On the stability of inverse problems. *Dokl. Akad. Nauk SSSR*, 39:195–198, 1943.

[48] David L. Phillips. A technique for the numerical solution of certain integral equations of the first kind. *J. Assoc. Comput. Mach.*, 9(1):84–97, January 1962.

[49] Martin Hanke and Per Christian Hansen. Regularization methods for large-scale problems. *Surv. Math. Ind.*, 3(4):253–315, 1993.

[50] Per Christian Hansen. *Rank-Deficient and Discrete Ill-Posed Problems: Numerical Aspects of Linear Inversion*. SIAM, Philadelphia, PA, 1998.

[51] Andreas Höcker and Vakhtang Kartvelishvili. Svd approach to data unfolding. *Nucl. Instrum. Methods A*, 372(3):469–481, April 1996.

[52] William Hadley Richardson. Bayesian-based iterative method of image restoration. *J. Opt. Soc. Am.*, 62(1):55–59, January 1972.

[53] Leon Brian Lucy. An iterative technique for the rectification of observed distributions. *Astron. J.*, 79:745–754, June 1974.

[54] Larry A. Shepp and Yehuda Vardi. Maximum likelihood reconstruction for emission tomography. *IEEE Trans. Med. Imaging*, 1(2):113–122, October 1982.

[55] Tim Adye. Unfolding algorithms and tests using RooUnfold. 2011.

[56] CMS Collaboration. Study of high-pt charged particle suppression in pbpb compared to pp collisions at 2.76 tev. CMS Analysis Note CMS-AN-11-101, CMS, 2011.

[57] Serguei Chatrchyan et al. Measurement of jet fragmentation into charged particles in pp and PbPb collisions at sqrt(s[NN])= 2.76 TeV. 2012.